The Rational Synthesis and Catalytic Testing of Heterogeneous Multimetallic Nanoparticles for the Hydrogenation of CO_2

James Warwick Max Crawley

Cardiff Catalysis Institute,

University of Cardiff

Degree: Master of Philosophy (MPhil)

Supervisor: Professor Graham Hutchings

2019 – 2023

Table of Contents

Abstract

It has been documented for over a century that metal surfaces can act as catalysts for many different reactions, such as the Fe-based catalyst used in the Haber-Bosch ammonia synthesis. For many decades, metal nanoparticles, defined as particles less than 100 nm in diameter, have become widely used as catalysts for many industrially important reactions, including hydrogenations, dehydrogenations, oxidations, reductions, and more. The nanoscopic size of a metallic nanoparticle results in extremely high surface area to volume ratios, which in turn results in a large number of catalytic sites per quantity of material used. Since catalyst design focuses on the highest activity and selectivity towards the desired product using the least material possible, metal nanoparticles have become an attractive choice.

Multimetallic nanoparticles, which include more than one metal, have become increasingly popular over the past two decades. Synergistic effects between metals have been reported by many research teams. A wide array of publications have indicated a superior catalytic activity and selectivity towards the desired product when adding a second, or even a third metal, to a nanoparticle catalyst, when compared to monometallic catalysts. When designing a multimetallic nanoparticle catalyst for application in an industrial reaction, there are many factors to consider. Particle size, shape, morphology, structure, and molar ratio between metals are all highly important. Small alterations to even one of these factors can have a dramatic impact on catalytic performance. Many traditional synthesis methods still commonly used today, such as wet and incipient wetness impregnation, are crude processes that afford poor control over these factors. This is especially an issue in the design of multimetallic nanoparticles, which are more complex than monometallic nanoparticles.

A highly rational synthetic procedure known as Strong Electrostatic Adsorption (SEA), developed by John Regalbuto, has been investigated in the synthesis of supported multimetallic Pd-containing nanoparticles as catalysts for the hydrogenation of CO_2 to methanol. Methanol is a highly important industrial chemical – 53 million tonnes were consumed in 2011 alone – and this process is important for CO_2 capture. The SEA method involves altering the pH of the solution to induce a charge on the supporting material, maximising electrostatic interaction between the supporting material and the metal precursors to yield small nanoparticles around 1 nm in diameter.

Units and Abbreviations

- % = Percent
- µm = Micrometres (10^{-6} Metres)
- µmol = Micromoles (10^{-6} Moles)
- Å = Ångströms (10^{-10} Metres)
- AB = Ammonia Borane
- AC = Activated Carbon
- AU = Arbitrary Units
- acac = Acetylacetonate
- aq = Aqueous
- ATR = Attenuated Total Reflectance
- BE = Binding Energy
- BET = Brunauer-Emmett-Teller
- BMNP = Bimetallic Nanoparticle
- °C = Degrees Celsius
- cat = Catalyst
- CCI = Cardiff Catalysis Institute
- Co-SEA = Simultaneous Strong Electrostatic Adsorption
- cm = Centimetre (10^{-2} Metres)
- CPA = Chloroplatinic Acid
- CPS = Counts Per Second
- CTAB = Cetyltrimethyl ammonium bromide
- CTAC = Cetyltrimethyl ammonium chloride
- CVI = Chemical Vapour Impregnation
- CZA = Copper Zinc Alumina
- DME = Dimethyl Ether
- DMF = Dimethylformamide
- DRIFTS = Diffuse Reflectance Infrared Fourier Transform Spectroscopy
- EDX = Energy Dispersive X-ray
- en = Ethylenediamine
- eV = Electron Volts
- FCC = Face Centred Cubic
- FT-IR = Fourier-Transform Infrared
- FTS = Fischer-Tropsch Synthesis
- g = Grams

- GHSV = Gas Hourly Space Velocity
- GR(R) = Galvanic Replacement (Reaction)
- h = Hours
- HAADF-STEM = High Angle Annular Dark Field Scanning Transmission Electron Microscopy
- HCP = Hexagonal Close Packed
- HSA = High Surface Area
- HTR = High Throughput Reactor
- IR = Infrared
- IWI/DI = Incipient Wetness Impregnation/Dry Impregnation
- k = Rate Constant
- k_{ads} = Rate Constant of Adsorption
- K = Kelvin
- kg = Kilograms (10^3 Grams)
- kJ = Kilojoules (10^3 Joules)
- k_{obs} = Observed Rate Constant
- kV = Kilovolts (10^3 Volts)
- L = Litres
- m = Metres
- M = Molar
- $_M$ = Metal
- M# = Metal (number)
- mg = Milligrams (10^{-3} Grams)
- min = Minutes
- mL = Millilitres (10^{-3} Litres)
- mm = Millimetres (10^{-3} Metres)
- mM = Millimolar (10^{-3} Molar)
- MMNP = Monometallic Nanoparticle
- mmol = Millimoles (10^{-3} Moles)
- MNP = Metallic Nanoparticle
- mol = Moles
- MPa = Megapascals (10^6 Pascals)
- MP-AES = Microwave Plasma Atomic Emission Spectroscopy
- nm = Nanometres (10^{-9} Metres)
- NP = Nanoparticle

- OR(R) = Oxygen Reduction (Reaction)
- oxC = Oxidised Carbon
- P25 = TiO_2 with average particle size 25 nanometres.
- pH = Potential of Hydrogen, negative base 10 logarithm of protons in solution
- pK_b = Negative base 10 logarithm of base dissociation constant
- ppm = Parts Per Million
- PVP = Polyvinylpyrrolidone
- PZC = Point of Zero Charge
- RDS = Rate Determining Step
- RWGSR = Reverse Water Gas Shift Reaction
- s = Seconds
- SEA = Strong Electrostatic Adsorption
- SEM = Scanning Electron Microscopy
- Seq-SEA = Sequential Strong Electrostatic Adsorption
- SI = Sol-immobilisation
- (S)SA = (Specific) Surface Area
- STEM = Scanning Transmission Electron Microscopy
- T/Temp = Temperature
- TA = Tetraammine
- TEM = Transmission Electron Microscopy
- TMNP = Trimetallic Nanoparticle
- TOF = Turnover Frequency
- TPR = Temperature Programmed Reduction
- TtMNP = Tetrametallic Nanoparticle
- UV(-vis) = Ultraviolet(-visible)
- VOC = Volatile Organic Compound
- v/v% = Volume By Volume Percent
- WGSR = Water Gas Shift Reaction
- wt.% = Weight Percent
- XANES = X-ray Absorption Near Edge Structure
- XPS = X-ray Photoelectron Spectroscopy
- XRD = X-ray Diffraction

Chemical element symbols have been used throughout.

Acknowledgements

I would like to give all my thanks to the people who supported me during my time working on this project. However, I would like to give particular thanks to Graham Hutchings and Nick Dummer for their time and the guidance they offered me throughout my project.

I would like to thank Graham Hutchings and Nick Dummer for his help, support and guidance in helping me gain independence as a chemist. I would like to thank them for sitting with me and offering direction throughout the project.

I would like to thank the post-doctoral team for guiding me and encouraging me to read further into the literature, and for supporting me during the practical and written aspects of the project. I would like to thank them for patiently answering my questions.

I would also like to thank the PhD and Post-Doc students at the Cardiff Catalysis Institute who provided very useful information and took time out of their busy schedules to show me how to use industrial-grade equipment (MP-AES, SEM, TEM, EDX, TPR, and many more).

I would like to thank PhD student Isla Gow for her development of the modified Farag method which was used in this project to synthesise high-surface area ZnO. I would like to thank PhD student Naomi Lawes for the experimental details and demonstrations on pelleting and metal ratios to use in CVI, as developed by her own experiments. I would like to thank post-doc student Dr. Louise Smith for providing information and operating the high throughput reactor, which was used to obtain the catalytic data.

I would like to give my thanks to Dr. Andy Logsdail and his team of PhD students for providing theoretical insight to this project, in particular to the computational aspect of this research, and allowing me to see this for myself by granting me the use of the Hawk supercomputing facility.

Finally, I would like to thank both the Cardiff Catalysis Institute and the University of Cardiff chemistry department for this incredible opportunity.

1 Introduction

In the chemical industry, catalysis underpins the majority of key processes. Many chemical industries such as food production, plastics, pharmaceuticals, and commodity chemicals rely on catalysis to meet societal demands. In order to achieve sufficient turnovers, a catalyst must be engineered to afford a high activity while simultaneously having high selectivity towards the product. A good catalyst suppresses competing reactions or side reactions, which results in high yield of product in less time and can be reused in multiple cycles of the reaction. The field of catalysis strives to use as little material as possible to increase the sustainability of the use of the catalyst.[1]

1.1 Fundamentals of Catalysis

1.1.1 Mode of Action

In any chemical reaction, bonds between atoms within molecules are broken. The atoms rearrange themselves and new bonds are formed to yield new molecules. Each of these processes require energy. Each bond between atoms has an associated bond energy, which must be overcome to break the bond. This means chemical reactions require energy to occur. This minimum energy input is known as the *activation energy* (E_a), acting as a barrier to be surmounted before the reaction can occur.

Catalysts serve to lower this activation energy barrier of a chemical reaction. They achieve this by providing an alternate reaction route or mechanism which is of lower activation energy than the reaction of the molecules with no catalyst. Fig. 1.1 demonstrates the comparison between the progression of the catalysed reaction (red) and the uncatalyzed reaction (turquoise) with regards to potential energy of the reaction. The effect of this is an increase in the rate of a chemical reaction, and milder conditions required to initiate the reaction. For example, a chemical reaction where a temperature of 400 K would be required to overcome the activation energy barrier may occur at a temperature of 300 K in the presence of a catalyst.

The addition of a catalyst lowers the activation barrier for a chemical reaction, however, the enthalpy change (ΔH) is conserved.[2]

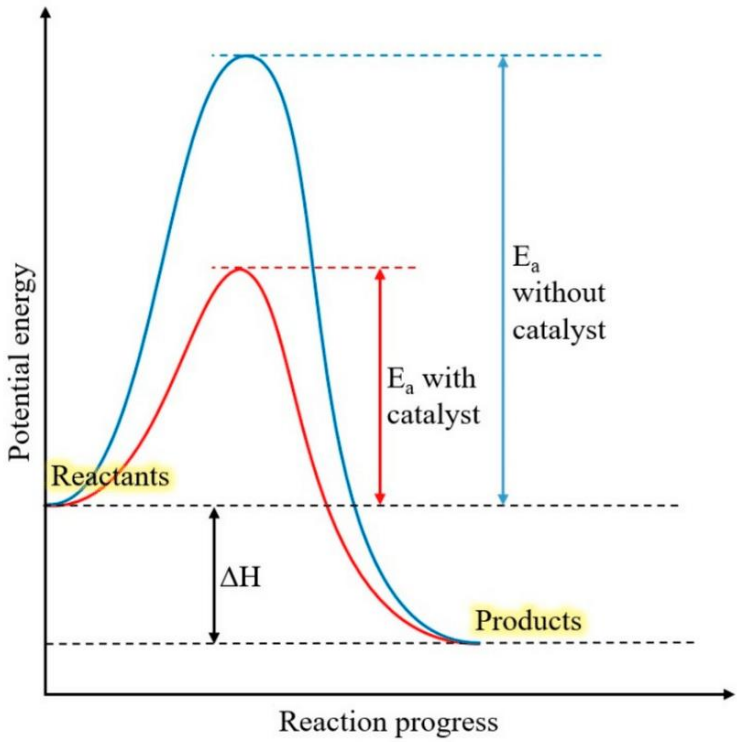

Fig. 1.1 – A graph illustrating the effect of a catalyst on the activation energy (E_a) of a chemical reaction. Reproduced from [2].

1.1.2 Designing a Suitable Catalyst

In designing a suitable catalyst for a reaction, there are several factors to consider, other than the catalytic activity (the increase in the rate of the chemical reaction per quantity of catalyst). The catalyst must not facilitate or favour any competing reactions or side reactions that may lead to unwanted byproducts which would lower the atom economy of the process and thus increase the environmental impact.[3]

Many industrial chemical reactions are also reversible, with the forwards “desirable” reaction path (reactants – products) in dynamic equilibrium with the competing reverse path (products – reactants). A suitable catalyst should lower the activation barrier of the forward reaction, thus increasing the rate of formation of the products. The catalyst should also ideally work to inhibit side reactions or over-reactions. The suppression of competing reactions, and the favouring of the formation of desired products, is known as *selectivity*, and is measured as the ratio of desired products to undesired products.

Another factor to consider in catalyst design is the *reusability*. In theory, the catalyst itself is not consumed or altered. Any changes to the catalyst during a reaction cycle

must be transient, being restored to its original form at the end of the reaction. This means catalysts should be re-usable. In reality, catalysts do not last forever. This may be due to physical deformation of the catalyst in the conditions of the reaction. Catalytic "poisoning" may also occur, which is when the catalyst is inhibited by certain byproducts or intermediates during the reaction. Unwanted byproducts or reactants may also react with the catalyst and alter it in such a way it can no longer be used. As such, the reusability of the catalyst is also to be assessed.[4]

Another factor to consider is the type of catalyst. Catalysts can be homogeneous or heterogeneous. Homogeneous catalysts are catalysts that exist in the same phase as the reactants. For example, solvated acid or base catalysts in a solution-phase reaction. Heterogeneous catalysts exist in a different phase to the reactants. For example, a solid-phase catalyst in a solution or gas-phase reaction.

The aim in catalyst design is to devise a catalyst that exhibits high activity, high selectivity, high reusability, and a suitable type for the reaction.

1.1.3 Heterogeneous Catalysts

For the scope of this project, heterogeneous catalysts have been studied. Specifically, solid-phase catalysts for gas-phase reactions. Solid-phase heterogeneous catalysts work through adsorption of the reactants onto the catalyst surface and orienting the reactants in such a way to promote their reaction. Finally, the product desorbs from the catalyst. An example of such a reaction is the hydrogenation of ethylene to ethane in the presence of a nickel catalyst, as displayed in Fig. 1.2.[5] First, H_2 adsorbs onto the Ni surface, breaking the H-H bond. Ethylene can then react with an adsorbed hydrogen atom to form an intermediate in which the C=C bond breaks and chemisorbs to the nickel surface (dissociation). There, the intermediate and an adsorbed H atom are oriented in such a way that ethane can form (coupling), desorbing the newly formed ethane molecule (desorption).

The adsorption of the reactants to the metal surface and providing the correct orientation to facilitate the reaction provides an alternate reaction mechanism that is lower in energy than the uncatalysed reaction, thus increasing the rate of the reaction. For heterogeneous reactions similar to this example, the atoms at the surface of the metal function as the catalytic sites.

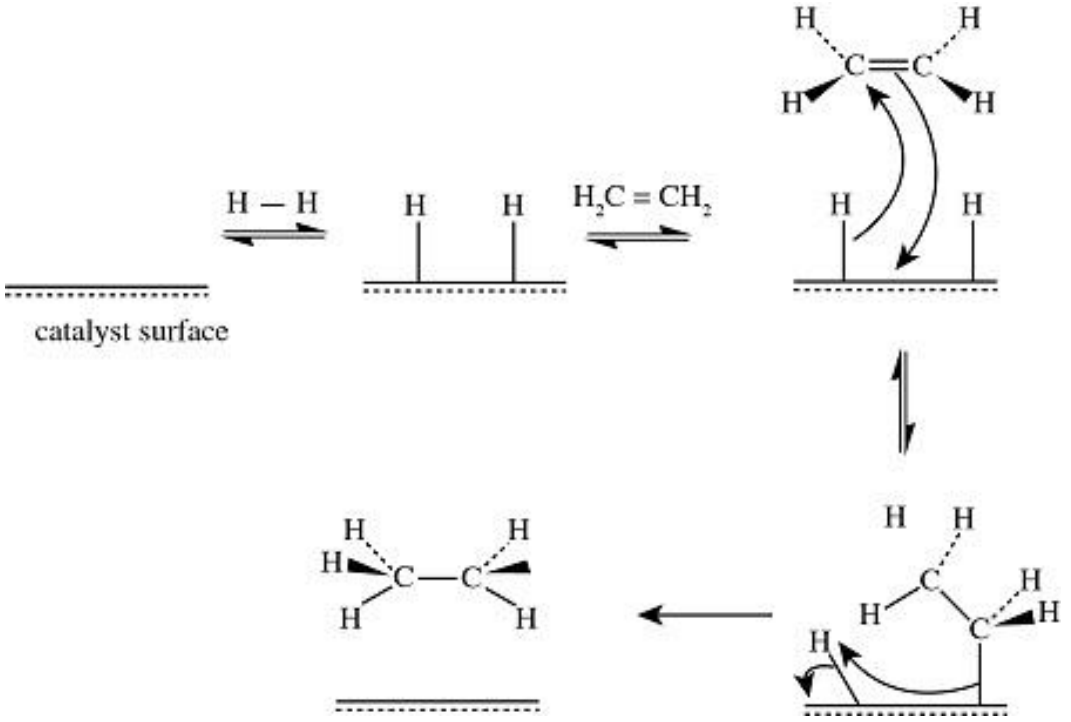

Fig. 1.2 – The reaction mechanism of the hydrogenation of ethylene to ethane on the surface of a nickel catalyst. This is a typical example of a heterogeneous catalyst in action. Reproduced from [5].

Since the catalytically-active atoms are only on the surface and not in the bulk of the metal, there is much material within the catalyst that is going unused, thus the quantity of material is not minimised. In order to meet the demand of using as little material as possible for the greatest catalytic activity, this project aims to investigate metallic *nanoparticles* as catalysts.

1.1.4 Measuring Catalytic Performance

The only way to measure the performance of a catalyst is to evaluate its activity in the reaction the catalyst was designed for. There are several ways to enumerate the performance of a heterogeneous catalyst.

Measurements of reactants consumed do not take into account selectivity towards products. As such, these tend not to be used. One of the most commonly reported measures is the turnover number (TON). This is defined as the number of chemical conversions of reactants per quantity of catalyst. This is typically reported as *turnover frequency (TOF)*, which is TON per a unit of time. In a metal-based catalyst, this can be calculated by examining the moles of product formed in a specific amount of time, per mole of catalytic active site. However, the quantity of catalyst can also be

measured in moles of metal, or mass of catalyst. The units of TOF are typically (unit time)$^{-1}$. *Mass activity* measures the moles of product formed per unit mass (typically kg) of catalyst, per unit of time, and typically have units of ($mol_{product}$ unit $mass_{cat}^{-1}$ unit $time^{-1}$), or ($mol_{product}$ $mol_{metal,M}^{-1}$ unit $time^{-1}$).[6]

Ideally, measures such as TOF and activity should be useful to form easy comparisons of catalytic performances across research centres. However, in literature, catalytic activity comparison between studies often presents a challenge. In addition to terms such as TOF, activity, and productivity often being used interchangeably, challenges arise due to the frequent lack of specific activity data given, and differing units. Some reports use kg of catalyst as unit, whereas others use moles of active site, or even reaction rate constants. When trying to draw direct comparisons between papers, this can lead to non-trivial unit conversions which are often made more difficult, if not impossible, by insufficient information in the articles. Differing test conditions between papers can further compound the difficulty of these comparisons.[7]

1.2 Introduction to Nanoparticles as Catalysts

Nanoparticle materials have unknowingly been used since antiquity. Roman glass workers in the fourth century A.D. utilised colloidal gold nanoparticles to produce glasses that changed colour depending on the location of the light source, as exampled by the famous Lycurgus cup. It would, however, be another fifteen centuries before scientific interest in colloidal gold would become apparent, when Michael Faraday investigated the interactions of light with colloidal nanomaterials in the 1850s.[8] It would take another 130 years for a new use of nanomaterials to flourish – their applications as catalysts within the commercial chemical industry.[7,9]

1.2.1 Nanoparticles as Catalytic Sites

In order to achieve sufficient efficiency, yield and product purity in industrial processes to meet growing demands, the main objective in catalysis is to maximise catalytic performance by developing catalysts with a high number of active sites per unit mass.[10]

A nanoparticle is defined as any ultrafine particle where its dimensions measure below 100 nm. Due to the fact volume is proportional to $(length)^3$, and surface area is proportional to $(length)^2$, as the volume of any object decreases, the surface area-to-volume ratio increases. Considering a large ingot of copper, the percentage of copper

atoms within the ingot to those that are on the surface would be extremely low. However, with nanoparticles, as their dimensions are on the nanometre scale, nanoparticles possess extreme surface area-to-volume ratios.[10] Fig. 1.3 illustrates how the diameter of spherical and tetrahedral copper nanoparticles correlates to the percentage of atoms that are “surface atoms”.

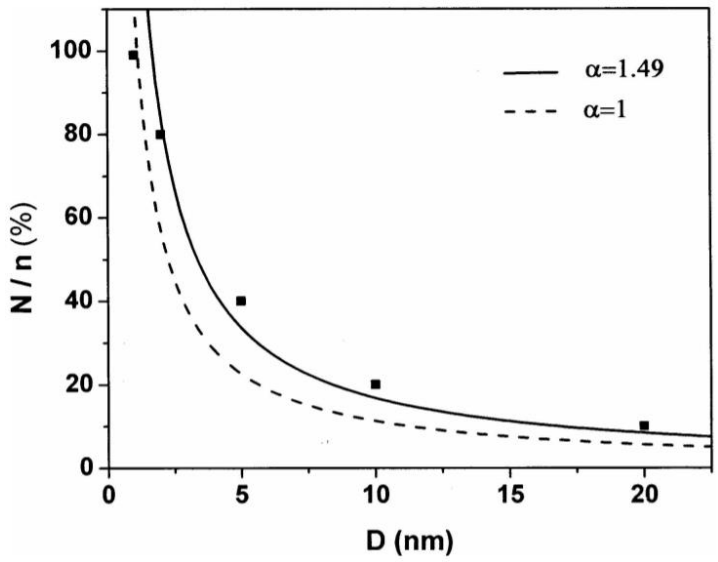

Fig. 1.3 – A graph illustrating the percentage of surface atoms of Cu nanoparticles as a function of nanoparticle size. α=1 corresponds to a spherical particle and α=1.49 a tetrahedral particle. Reproduced from [11].

This graph shows a copper nanoparticle 20 nm in diameter has approximately 10% of its atoms on its surface. As the size of the nanoparticle decreases, the proportion of surface atoms increases two-fold with each halving of diameter. At a diameter of 10 nm, 20% of the atoms are surface atoms. At a diameter of 5 nm, 40% of the atoms are surface atoms.

For decades, metal surfaces have been used to catalyse chemical reactions. A notable example of this is the Haber-Bosch synthesis of ammonia from H_2 and N_2. First industrialised in 1913 and still used to produce ammonia commercially to this day, this revolutionary synthetic process involves the use of an iron catalyst.[12] The mode of action of metallic surfaces involves adsorption and desorption of the reactants, or substrates, on the coordinatively-unsaturated atoms on the surface of the metal.[13] As such, the property of very high surface atom to atom ratio seen in metal nanoparticles satisfies the need for a high number of active sites per mass of material, thus reducing the overall quantity of material required, in the field of catalysis.

Metal nanoparticles have found catalytic applications in many different types of industrial reactions. These include hydrogenation reactions,[14–29] dehydrogenation reactions,[30–46] redox reactions,[47–56] and even electrochemical reactions.[57–67]

Since the mode of action of nanoparticles depends on chemical and physical interactions between the reagents and the nanoparticle, different metal species of nanoparticle exhibit catalytic activity towards different reactions. For example, palladium nanoparticles are known for their high affinity for hydrides, readily adsorbing H_2 onto the surface and splitting the H-H bond. Thus, palladium nanoparticles are often used to catalyse hydrogenation reactions.[68]

When using metal nanoparticles as catalysts, there are numerous factors to consider, other than the metal species. As previously discussed, the size of the nanoparticle is an important factor to consider as the size of the particle can impact the number of surface atoms, and thus the number and density of active sites.[69]

An example of the impact the size can have on catalytic activity has been demonstrated by Isaifan *et al*. with their use of Pt nanoparticles supported on carbon black for the complete oxidation of ethylene.[70] Pt loadings were 0.4±0.04 wt.% for all catalysts tested. The team reported that the smaller the diameter of their nanoparticles, the lower the temperature of the complete oxidation of ethylene occurred. Fig. 1.4 displays this trend:

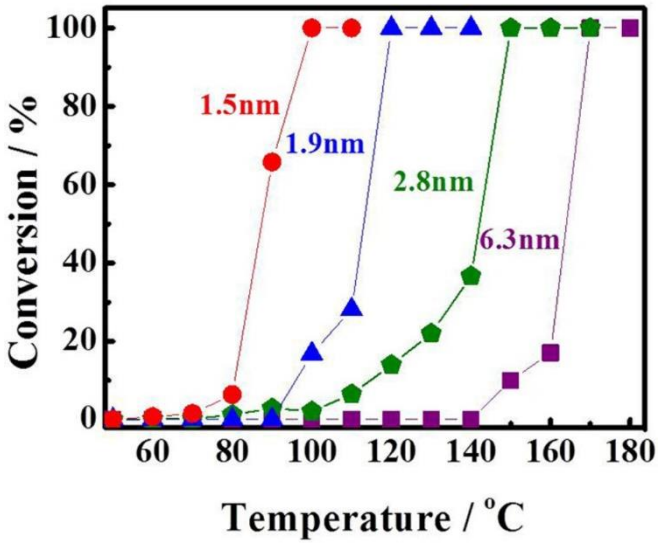

Fig. 1.4 – The % conversion of ethylene vs. temperature plot for Pt/C nanoparticles of four different diameters. Reproduced from [70].

As shown by this dataset (Fig. 1.4), the temperature of complete oxidation is more than 70 °C lower with the catalyst of particle size 1.5 nm than the catalyst of particle size 6.3 nm with the same Pt loading. The increase in number of surface atoms with the 1.5 nm catalyst plays a large part in this difference. However, the catalytic activity of the 1.5 nm catalyst is further increased by the higher proportion of very low-coordinated metal atoms, such as “corner sites”, which increase in atomic proportion as the size of the particle decreases.

Size alone can have a significant impact on catalytic activity. However, another crucial aspect to consider is the shape.[71] Fig. 1.5 shows some examples of different metal nanoparticle shapes.[72]

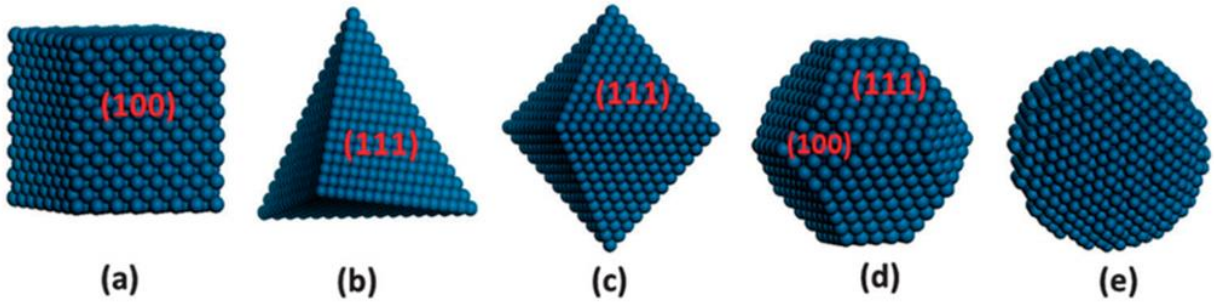

Fig. 1.5 – Examples of different shapes of metal nanoparticle. (a) cubic; (b) tetrahedral; (c) octahedral; (d) cuboctahedral; (e) spherical. The Miller indices *(hkl)* of the exposed planes have been marked on each face in red. Reproduced from [72].

In each of these different nanoparticle shapes, the Miller Indices *(hkl)* are used to categorise the exposed surface plane. These indices represent parallel equidistant planes of atoms within a unit cell, one of which passes through one of the vertices defined as the origin. Subsequent planes pass through intercepts a/h, b/k, c/l, where a, b, and c are the lengths of the unit cell, and h, k, and l are integers denoting the number of these intercepts within the unit cell. In the cubic metal nanoparticle case (Fig. 1.5a), the (100) surface planes are exposed on all facets. In the tetrahedral and octahedral cases (Fig. 1.5b and 1.5c), (111) surface planes are present on all faces. The cuboctahedral case (Fig. 1.5d) exhibits both (100) and (111) facets.

Each of these different surface planes exposed by these different shapes feature different coordination numbers of the surface atoms. This has an impact on the interaction with the adsorbing reactants, and will influence the adsorption, dissociation, coupling, and desorption stages of the reaction. This is due to the differing intrinsic binding energies of each of these surface atoms with differing coordination numbers

to the reactants and products. Thus, many reactions are selective to specific surface planes, and by extension, certain shapes. For example, the hydrogenation of benzene yields cyclohexane on cubic Pt(100) nanoparticle surfaces, and a mixture of cyclohexane and cyclohexene on cuboctahedral Pt(111) surfaces.[73] Fig. 1.6 demonstrates these Pt nanoparticle shapes, cubic and cuboctahedral, exposing the Pt(100) and Pt(111) faces respectively.

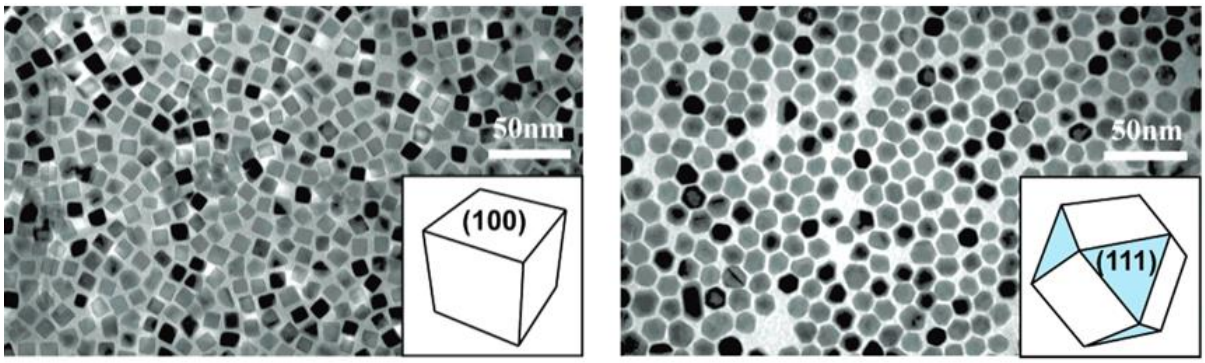

Fig. 1.6 – TEM images and diagrams of cubic Pt nanoparticles (left) and cuboctahedral Pt nanoparticles (right). Average particle sizes are 12.3 ± 1.4 and 13.5 ± 1.5 nm respectively. The cubic particles exhibit (100) surfaces, and the cuboctahedral particles exhibit (111) surfaces. Reproduced from [73].

This highlights that nanoparticles tailored towards specific reactions must be synthesised to aim for a highly controlled morphology (overall shape) and exposed surface plane in order to achieve high selectivity towards desired products and against unwanted byproducts.

1.2.2 Supported Nanoparticle Systems

Along with the size, morphology, and surface specificity of nanoparticle systems as catalysts, one of the most important factors to consider is their stability. In the field of metal nanoparticle catalysis, the presence of a supporting material is almost ubiquitous. Due to their thermodynamic instability, as previously discussed, during a catalytic process, unsupported (colloidal) metal nanoparticles are known to sinter under many reaction conditions. This results in a loss in metal surface area as the nanoparticles become larger in size. This results in losses not only in catalytic activity, but also selectivity.[74] The supporting material effectively anchors the nanoparticles in place, greatly reducing the magnitude of sintering in the reaction conditions for which the catalyst is applied.[75]

Not only does a supporting material provide stability, it also provides a surface for increased dispersion of the nanoparticles and a more even distribution, as well as controlling the shape and size of the nanoparticles.[75]

A supporting material typically consists of larger particles of a metal oxide or activated carbon. The metal nanoparticles are anchored to the surface of the supporting material. An example of this is gold nanoparticles anchored to alumina (written as Au/Al_2O_3) or titania (Au/TiO_2). TEM images of these materials are shown in Fig. 1.7.[76]

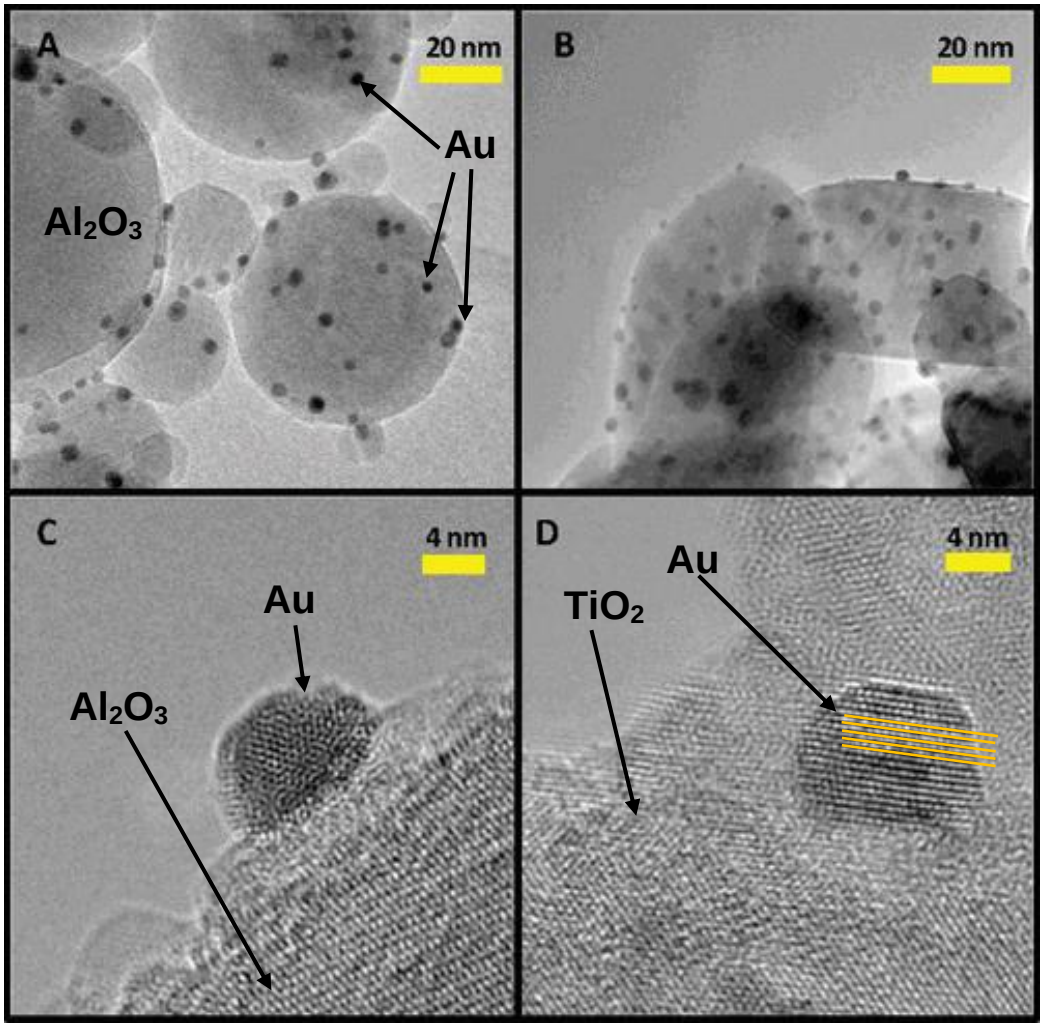

Fig. 1.7 – (a) and (b): TEM images of Au/Al_2O_3 and Au/TiO_2 catalysts respectively. (c) and (d) HR-TEM images of Au/Al_2O_3 and Au/TiO_2 catalysts respectively. The orange lines shown in (d) highlight lattice planes. The distance between these planes can be used to determine particle shape and exposed surface plane. Modified from [76].

The TEM images show the Au nanoparticles are immobilised on the larger metal oxide particles. Using images such as this, nanoparticle size distribution can be estimated.

Moreover, analysis of the atomic spacing and lattice pattern of the HR-TEM images can be used to determine the particle shape and exposed surface plane.

Importantly, the supporting material is not merely an inert surface to anchor the nanoparticles. The supporting material itself can have synergistic effects with the metal nanoparticle.[77] Moreover, the supporting material may provide additional active sites to facilitate catalytic activity, essentially acting as a promoter for the catalyst.[78] Because of this, supported nanoparticles are often referred to as a "supported nanoparticle *system*".

As expected, due to the interactions and interplay between the supporting material and the metal nanoparticle, the choice of support can play an important role in catalytic activity. For example, when Cuenya *et al*. applied supported Pt nanoparticles to a methanol decomposition reaction, the choice of supporting material for the Pt nanoparticles showed a large impact on the relationship between the % conversion of methanol and temperature (refer to Fig. 1.8). This was evident even when the size, shape, morphology, and loading of the Pt nanoparticles were all kept constant.[79]

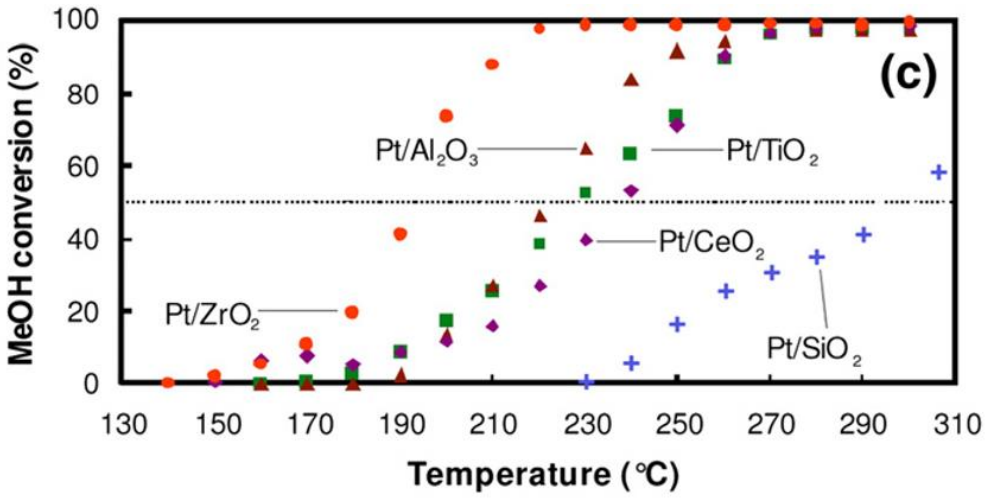

Fig. 1.8 – A graph reported by Cuenya showing the activity in % conversion of methanol over a Pt nanoparticle where 2 wt.% Pt loading was deposited to five different oxide supporting materials. Reproduced from [79].

For this example, it is clear the zirconia (ZrO_2) support promoted the decomposition reaction to occur at a far lower temperature than other supporting materials, such as alumina (Al_2O_3), ceria (CeO_2), titania (TiO_2), and silica (SiO_2). When ZrO_2 is used as the supporting material, the reaction reaches completion at a temperature of 220 °C. When silica is used however, the reaction is at just 60% completion at 310 °C with no reaction at all occurring below 230 °C. This example illustrates the extent of the

interaction between the metal nanoparticles and the supporting material used in the reaction. This demonstrates that in designing a nanoparticle catalyst, choice of supporting material can be an extremely important factor.

1.2.3 Multimetallic Nanoparticle Systems

So far, the effect of nanoparticle size, shape, surface plane, and supporting material has been discussed with regards to metal nanoparticles composed of a single metal, such as Pd or Pt. However, metal nanoparticles need not be confined to a single metal. Metal nanoparticles may contain two or more metals. This introduces new degrees of freedom, and thus new factors to consider in addition to the previously-discussed considerations with single-metal nanoparticles. It is worth noting that any metals present in the supporting material, such as Al or Ti, are not counted since they generally are not within the nanoparticle itself.

There are huge advantages of adding additional metals when designing catalysts for industrial reactions. Multiple metals in a multimetallic particle system often exhibit synergistic effects with each other, as will be discussed extensively in later chapters, which can greatly improve catalytic performance. There are several ways this can occur: (i) a second metal may facilitate a rate-limiting step in a reaction that the first metal alone could not. (ii) electrical interactions between the two metals due to differing redox properties can also have promotional effects, (iii) the second metal suppresses a side reaction or the formation of a byproduct, thus increasing selectivity towards the desired product and the yield, (iv) shifting the equilibrium away from a competing reverse reaction and towards the product. In addition, multiple metals enables far greater flexibility in fine-tuning properties to greatly improve catalytic performance over monometallic counterparts.[80–100]

The addition of a second metal greatly increases the complexity of the investigations into these nanoparticles. As later sections will discuss, the presence of multiple metals poses synthetic fine-tuning challenges due to the wide array of additional parameters that must be controlled when compared to monometallic nanoparticles (MMNPs).

One of the new factors to consider when expanding to multimetallic nanoparticles is the *structure*. This is defined as the arrangement of the different metals within the nanoparticle. Even within the simplest multimetallic nanoparticle, the bimetallic

nanoparticle (BMNP), there are countless possible structures. Fig. 1.9 shows some of the more commonly reported structures.[101]

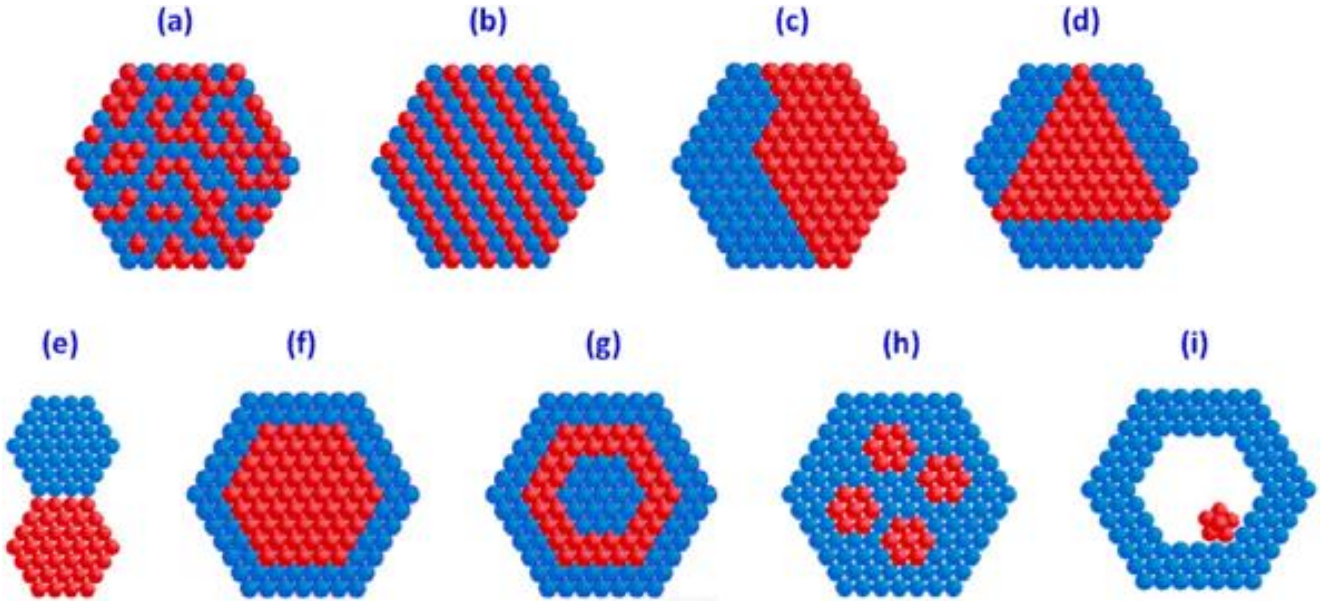

Fig. 1.9 – Some possible structures of bimetallic nanoparticles. Atoms of the two different metals are represented with blue and red discs. (a) random alloy; (b) alloy; (c) two-interfaced sub-cluster; (d) three-interfaced sub-cluster; (e) segregated nanoparticles; (f) core@shell; (g) multilayer core@shell; (h) small clusters of one metal within a single shell of the other metal; (i) movable core within hollow shell. Reproduced from [101].

The structure of the nanoparticle can have a dramatic impact on catalytic performance, including both activity and selectivity. As such, it is imperative that the structure of the nanoparticle is controlled during synthesis and remains unchanged under operando conditions.

Another important factor is the ratio between the metals, also known as the *composition*. This is also known as the metallic stoichiometry. In a bimetallic system, this would be written in the form A_xB_y, where A and B are metals, and *x* and *y* are the molar ratios of the metal. Alternatively, this can be written in the form A_xB_{100-x}, giving molar percentages of each metal within the nanoparticle. As will be discussed in later chapters, the composition of the nanoparticle can have drastic impacts on the catalytic performance.[102]

A further expansion of the multimetallic nanoparticle is the trimetallic nanoparticle (TMNP), which includes three metals. The same principles apply to BMNPs, however, as expected, a third metal further increases the complexity due to the addition of even more degrees of freedom. An even greater array of structures are now possible, a selection of which are shown in Fig. 1.10.

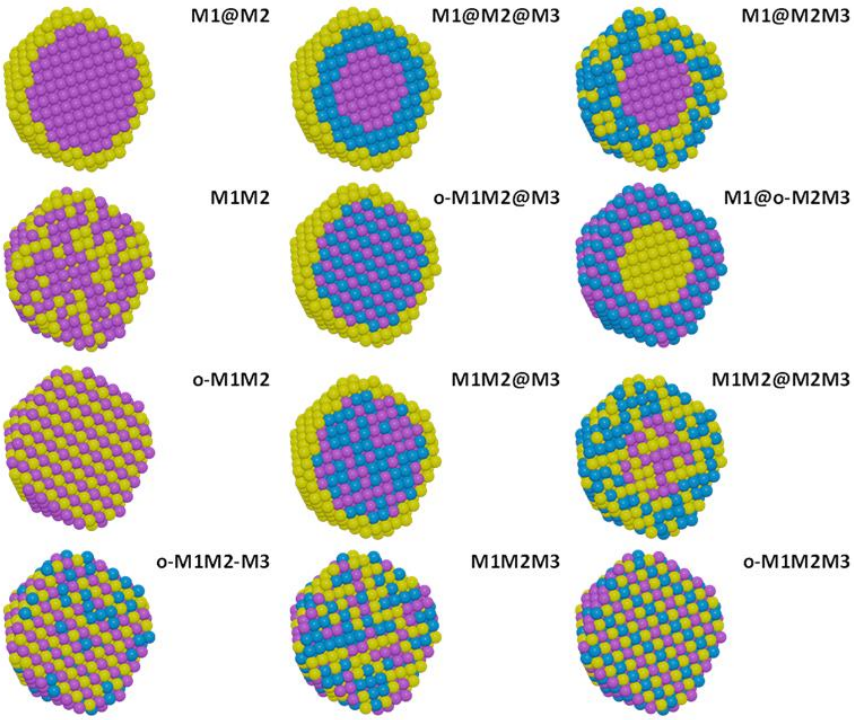

Fig. 1.10 – Possible structures of spherical bimetallic and trimetallic multimetallic nanoparticles, in particular, TMNPs. "o-" denotes an ordered structure. Reproduced from [7].

What Fig. 1.10 displays are just a few basic structures possible, and huge variations can occur even within the same basic structure, as shown with the bimetallic example (Fig. 1.9).

As with structural considerations, compositional consideration also becomes far more complex when expanding to TMNPs. This complexity is demonstrated by Fig. 1.11. In this example, supported trimetallic AuPdPt/CeO_2 catalysts have been used in the synthesis of H_2O_2 from H_2 and O_2.[103] The total metal loading has been fixed at 5wt.%. This contour plot illustrates how certain ratios of the same three metals exhibit almost no catalytic activity, whereas other ratios exhibit high catalytic activity. The plot further illustrates how islands of high activity can be within very small regions. In this study, the most active composition was found to be $Au_{2.4}Pd_{2.4}Pt_{0.2}$. Even slight deviations from this island resulted in a dramatic loss of activity. This highlights the importance of high control over composition when designing and challenges of synthesising a multimetallic nanoparticle as a catalyst.

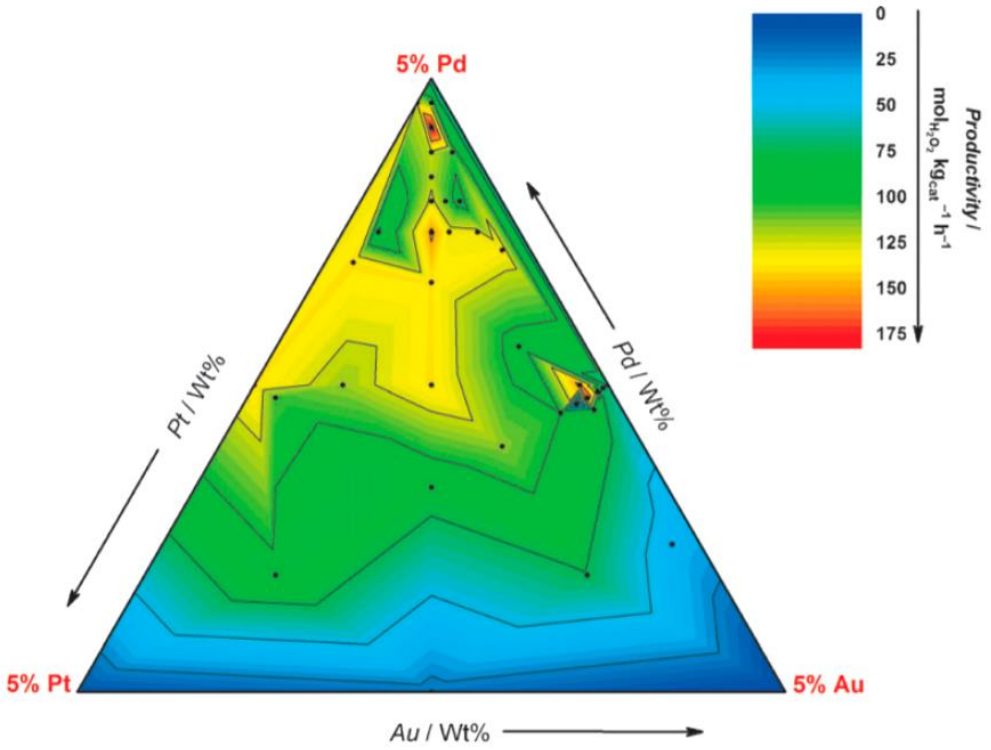

Fig. 1.11 – Contour diagram of catalytic activity of timetallic AuPdPt/CeO_2 catalysts for the reaction of H_2 and O_2 to form H_2O_2. This shows how widely catalytic performance (measured in terms of H_2O_2 productivity) depends on the ratio of the three metals. Reproduced from [103].

Research into systems as complex as TMNPs has become increasingly pertinent over the past decade. Over 130 papers relating to TMNPs were published in 2020 alone, with an upward trend of publications over the decade leading up to 2020. Fig. 1.12 shows the increase in publications relating to TMNPs between 1990 and 2020.[7]

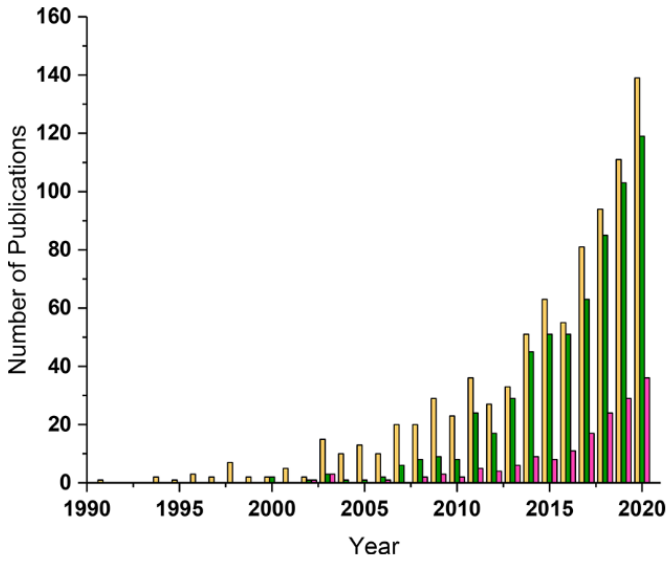

Fig. 1.12 – Number of publications relating to TMNPs based on Web of Science searches for “trimetallic catalyst” (tan); “trimetallic nanoparticles” (green); “trimetallic nanoparticles” with “applications” (pink), between 1990 and 2020. Reproduced from [7].

1.3 Synthesis of Metal Nanoparticle Systems

Whilst their extreme surface-area-to-volume ratio proves beneficial in catalysis, this property also provides challenges in their synthesis. One of the main challenges is the thermodynamic instability introduced by the large quantity of surface atoms compared to volume. Surface atoms are coordinatively unsaturated. In order to reduce the number of surface atoms and adopt a more stable bulk lattice-like configuration, nanoparticles are known to agglomerate into larger particles (sintering).[104] Larger particles have a lower surface area-to-volume ratio thus are less desirable for their applications in catalysis. Sintering can also result in less control towards other factors, such as the shape and morphology of the nanoparticle.[105]

The complexity of synthesis in metal nanoparticles is further increased when multimetallic systems are considered, due to the additional considerations of structure, composition, and segregation of the metals. This section will discuss several synthetic methods and detail additional challenges faced when applying the method to multimetallic systems.

1.3.1 Traditional Industrial Synthesis Methods

The two main industrial methods include impregnation and co-precipitation (CP).[106–113]

Wet impregnation involves an excess of solution containing dissolved metal precursor salts and a supporting material in suspension. The metal precursor is reduced, depositing the metal on the supporting material surface. This is followed by activation through calcination or reduction at high temperature, and finally a drying step. A modification of this method is incipient wetness impregnation (IWI). This involves addition of the solution of metal precursor to the supporting material of known surface area and pore volume, such that the solution fills 90-95% of the pore volume of the supporting material. The pores of the supporting material draw in the metal solution through capillary action. Following filtering and drying the slurry, the recovered catalyst is then ground and calcined to remove residual volatile compounds within the system. This method results in metal nanoparticles on the surface of the supporting material.[114,115] Fig. 1.13 represents schematics of these two types of impregnation.

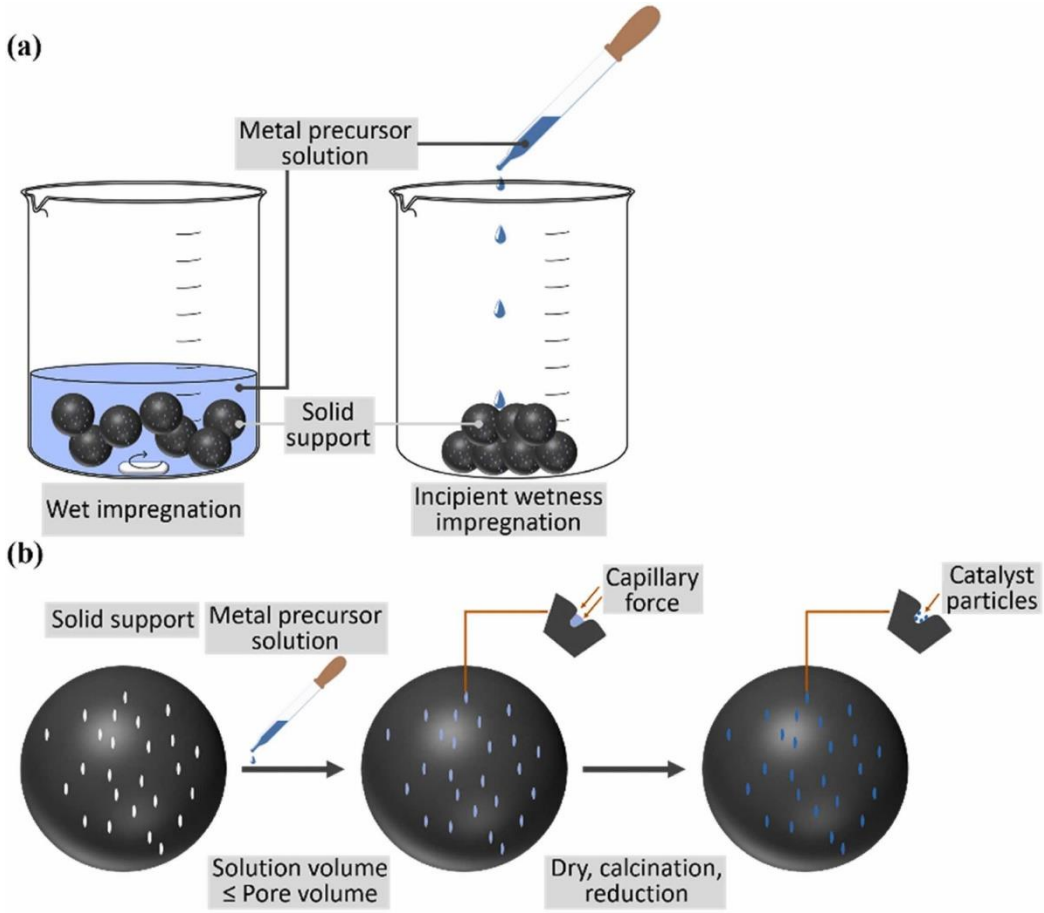

Fig. 1.13 – Schematics of (a, left) wet impregnation; (a, right) incipient wetness impregnation (IWI); and (b) detailed IWI schematic of formation of catalytic metal nanoparticles through capillary action. Reproduced from [116].

Co-precipitation involves the simultaneous formation of the nanoparticles and the supporting material. Typically, a solution of both the metal nanoparticle precursor and the metal oxide supporting material precursor is treated with a strong base, inducing precipitation of both precursors. The suspension is aged at elevated temperature overnight and then dried at high temperature (over 523 K). Finally, the sample is calcined at high (773 K) temperature.[117]

Different shapes and sizes are obtained depending on the method used: impregnation methods yield nanoparticles anywhere between 1 and 100 nm in diameter depending on conditions, as well as atoms and small clusters. Co-precipitation yields nanoparticles between 1 and 10 nm in diameter with atoms and clusters.[118]

Although impregnation and co-precipitation methods are conventional and the most widely used industrially, they are not without issues. As previously stated, there is a wide range of shapes and sizes that can be obtained using these methods. For

example, since IWI involves the drawing of metal into pores, variation in pore sizes and shapes can result in large differences in shape and size of the nanoparticle formed.[118] In addition, metal complexes that remain in solution and do not deposit on the surface of the supporting material can migrate during drying.[119] These methods afford less control over the formation of the nanoparticle. As discussed previously, particle size, shape, morphology, and surface plane can all have dramatic impacts on the catalytic activity of the system.

Despite issues with control of several parameters, and the further increase in complexity when additional metals are added, multimetallic nanoparticle systems prepared via traditional methods have been reported in literature. For example, simple wet impregnation has been used to synthesise several trimetallic nanoparticle (TMNP) systems. Examples include Mendoza-Nieto *et al.*'s synthesis of NiMoW nanoparticles supported on SBA-15,[120] and the trimetallic PdNiAg/C system reported by Yurderi *et al*.[121]

IWI has been reportedly used to synthesise an array of TMNP systems, too. Nakaya *et al*. successfully prepared $Pt_3(Fe_{0.75}M_{0.25})/SiO_2$, where M = Co, Ni, Cu, Zn, Ga, In, Sn, and Sb for use in alkene dehydrogenation.[122] AuPdPt alloys have also been prepared by He *et al* for use in solvent-free oxidation of benzyl alcohol in order to suppress the formation of the byproduct toluene, although these reportedly exhibited a far lower activity than AuPdPt prepared via alternate methods. This was due to the large particle sizes obtained in comparison to those obtained with non-traditional methods.[123] Size and composition distribution studies conducted by Lopez-Sanchez[124] and Bahruji[125] further highlight wide ranges of size distribution, and larger overall size of particle produced by impregnation methods than non-traditional methods.

Similar to monometallic nanoparticle synthesis using impregnation methods, the main issue arising with traditional impregnation is the lack of control over size, shape, and morphology. However, this is especially true when synthesising multimetallic nanoparticles due to the greater complexity and number of variables present in the system, which could potentially have dramatic impacts on catalytic performance. As such, in order to optimise catalytic activity for a range of commercial reactions using multimetallic nanoparticle systems, there exists a strong drive for novel synthesis methods that afford greater control over these additional parameters.[7]

1.3.2 Colloidal Methods

Colloidal synthesis of metal nanoparticles (MNPs) involves synthesising nanoparticles in the presence of a solvent, such as an aqueous environment. Upon formation, MNPs form a suspension in their solvent.[126] An advantage of these procedures is they eliminate the larger (>8 nm) particle sizes observed with many impregnation procedures.

One such colloidal method is sol-immobilisation (SI). This method overcomes the stability challenges and the potential loss of morphological control through the use of a capping or stabilising agent. These provide kinetic stabilisation in the form of electrostatic forces or steric factors. Electrostatic stabilisation may be achieved through an ionic surfactant, or counter ion. Steric stabilisation may be achieved through the use of a large polymer molecule. These are illustrated by Fig. 1.14.[127]

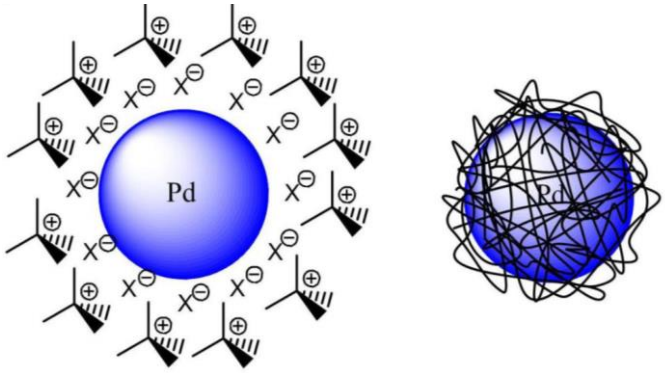

Fig. 1.14 – Left: Pd nanoparticle electrostatically stabilised by a double-layer surfactant. Right: Pd nanoparticle sterically stabilised by large polymer molecules wrapping around the nanoparticle by chemisorption. Reproduced from [127].

These stabilising agents, also known as capping agents, may also function to control the size and shape of the nanoparticles to tailor them to specific catalytic properties.[128]

The standard SI synthetic procedure involves a solution of a metal precursor, typically a soluble salt of the metal cation. A solution of the stabilising agent may then be added. The metal then may be isolated from solution and reduced under flowing reducing gas such as H_2,[129] or be chemically reduced in solution with a reducing agent such as sodium borohydride.[130] The reducing agent reduces the metal ions to their elemental form, initiating nucleation and crystal growth. The stabilising agent inhibits crystal growth, resulting in a cluster of atoms a few nanometres in diameter.[126]

The formation of palladium nanoparticles via ligand-mediated nucleation and coalescence mechanism described above is illustrated by Fig. 1.15.[131]

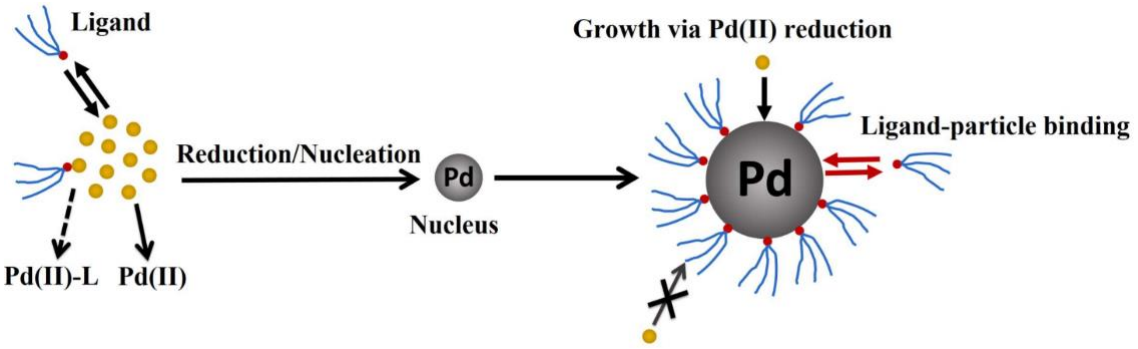

Fig. 1.15 – The generic procedure of the formation of metal nanoparticles in colloidal suspension through ligand-mediated nucleation and coalescence. Ligands prevent further growth and agglomeration. This capping effect could also be achieved with double layer surfactants. Reproduced from [131].

Many variations of this general procedure exist in order to control the shape, size, and morphology of the nanoparticles.[7] Colloidal methods can be extended to the production of multimetallic nanoparticles. Multimetallic nanoparticles, specifically TMNPs, have been successfully prepared and applied to several industrially important reactions. These include glycerol oxidation,[132] methanol oxidation,[133] and dehydrogenation of ammonia borane.[134]

Typically, using colloidal methods such as SI, multimetallic nanoalloys are prepared much in the same way as monometallic nanoparticles (MMNPs). Both or all the metal precursors can be added and reduced at once, in a method known as co-reduction SI. However, this can result in segregation of metals and large fluctuations of composition between different nanoparticles, a problem of which further investigation is required to solve.[123]

Another major issue that may arise with multimetallic nanoparticles, especially TMNPs, is the huge complexity of different outcomes that can arise when dealing with three metals, all with different reduction potentials. This makes growth and structural control more complex, and increases the difficulty of morphological control.

Kang *et al.* studied the ternary AuPdPt system, with the metals fixed in a 1:1:1 ratio.[135] Their method involved hydrazine and ascorbic acid as reducing agents, and CTAC as the capping agent. This resulted in an octahedral Au core with a dendritic shell of alloyed PdPt, a type of core@shell structure. In order to study the mechanism, bimetallic nanoparticles (BMNPs) involving Au and Pd were synthesised in the presence of CTAC. Core@shell Au@Pd octahedral (111)-faceted nanoparticles formed with average edge length 61 nm. Repeating this procedure with Pt yielded

Au@PdPt nanoparticles with average edge length 43 nm and a wider distribution of sizes. Repeating this experiment without ascorbic acid yielded Au MMNPs in a variety of shapes, with no Pd or Pt detected. When hydrazine was not used, bimetallic PdPt dendritic particles formed, highlighting the need for both reducing agents to gain control over particle formation. UV-Vis data also supported the importance of using CTAC, as without the capping agent, or using a different surfactant, the octahedral shape of the Au core was lost.

Although these methods work well for the AuPdPt system, they do not apply to other systems.[135] This is because other metals have their own electronic properties, reduction potentials, sizes, and preferred shapes of formation.

Other reported trimetallic systems synthesised through one-pot SI-type colloidal syntheses include CuAuPt,[136,137] PtAuRu,[138] Ag@PdAu,[139] and PdCo@Pt.[140] All of these examples, like Kang's study previously detailed, appear to have been prepared via a significant amount of trial and error to identify optimal conditions for specific shapes and compositions. It appears there is no "universal" one-pot colloidal method that can apply to a range of systems.[7]

However, methods involving polyols such as ethylene glycol have been reported to improve control via increasing the viscosity of the solution, which in turn limits uncontrolled growth of the nanoparticle. Polyols can also act as the solvent and the capping agent, resulting in greater control over size and morphology.[140,141,142] Future studies into the use of polyols in colloidal synthesis of multimetallic nanoparticles is thought to yield promising results.[7]

1.3.3 Chemical Vapour Impregnation

Another method of synthesising a supported nanoparticle, eliminating the need for a solvent, is chemical vapour impregnation (CVI). This method involves a modified chemical vapour deposition (CVD) set-up, in which volatile metal precursors, typically organometallic in nature, are heated under near-vacuum. This results in the sublimation of these precursors, but the temperatures are not high enough to decompose the organic component. Under these conditions, the gas-phase metal precursors are adsorbed onto the supporting material, resulting in a small, isolated metal nucleus (the nucleation step of crystal growth).[143] This method is useful in enabling the fine-tuning of composition and morphology of supported MNPs.[144] In this

method, the supporting material and metal precursor are physically mixed within the same vessel. As such, the sublimation and deposition steps occur within the same location. Studies utilising this method to synthesise MMNPs such as Pd and Pt deposited on TiO_2 have proven narrow particle size distributions of 1.5 – 2.8 nm.[144,145]

This method can be extended to multimetallic systems. This has been proven in the study by Bahruji *et al*.[143] This study produced high-metal-loading catalysts, 5wt.% Pd and 5wt.% Zn, on ZnO, TiO_2, or Al_2O_3 supports. For this study, the precursors $Pd(acac)_2$ and $Zn(acac)_2$ were used. Molar ratios of Pd:Zn varied from 1:1 and 1:10. The solid-state mixture of the acac salts and the supporting material were sealed in Schlenk apparatus and evacuated to a pressure of 10^{-3} bar. The mixture was heated to 418 K for 1 hour. Samples were calcined in air at 773 K for 16 hours to decompose the acac precursors. Fig. 1.16 shows TEM images of the BMNPs obtained through this method, showcasing size distribution.

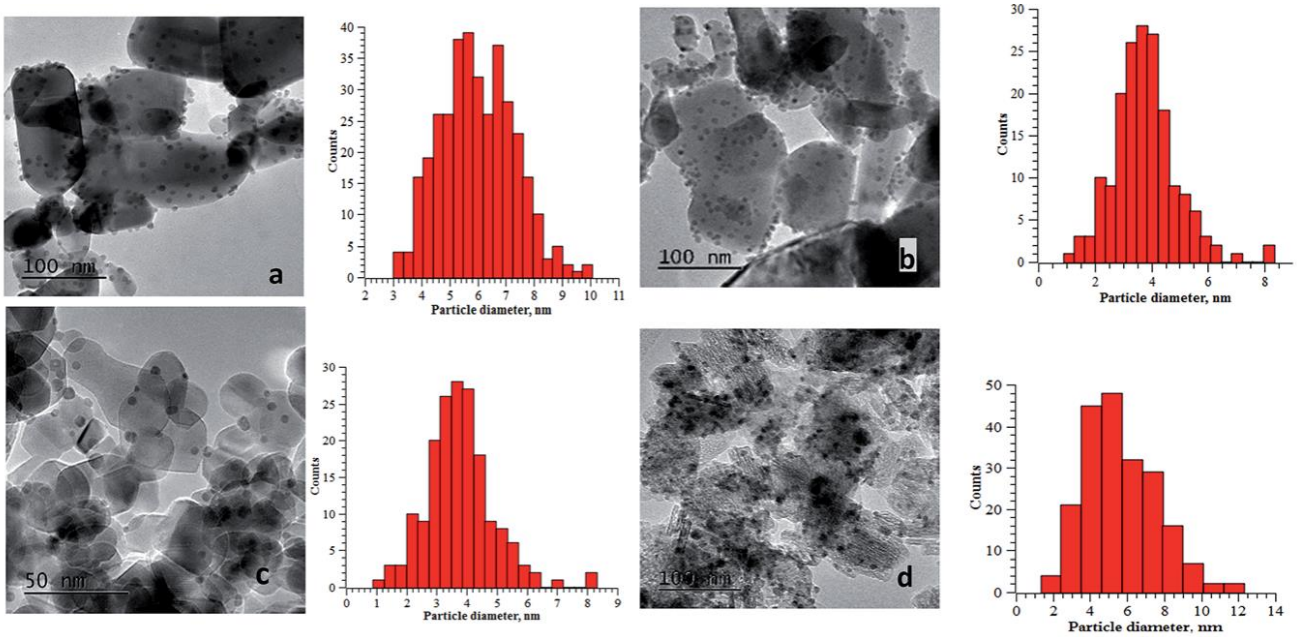

Fig. 1.16 – TEM images obtained of (a) 5% Pd/ZnO reduced without calcining; (b) 5% Pd/ZnO following calcination and reduction; (c) 5% PdZn(1:10)/TiO_2 following calcination and reduction; (d) 5% PdZn(1:10)/Al_2O_3 following calcination and reduction. Reproduced from [143].

The data shown in Fig. 1.16 was used to calculate a mean BMNP particle size of 3.9 nm on TiO_2. The PdZn nanoparticles were highly dispersed owing to the steric bulkiness of the acac precursor. XRD confirmed the presence of both metals, and reflection identification therein showed that the two metals were alloyed. Alloying likely occurred due to the physical proximity of the metals during the preparation. These catalysts were tested for activity for hydrogenation of CO_2 to methanol, wherein the activity of the BMNP formulation was much greater than supported MMNPs.

As previously mentioned, the deposition of the precursor onto the surface of the supporting material serves as the nucleation stage. From there, several possible modes of crystal growth are possible, resulting in different final morphologies of the system. The three basic modes of growth in any CVD process are Frank van der Merwe growth (layer-by-layer), Stranski-Krastanov (layer-plus-island), and Wolmer-Weber (island). These are displayed schematically, at varying coverages, through Fig. 1.17.[146]

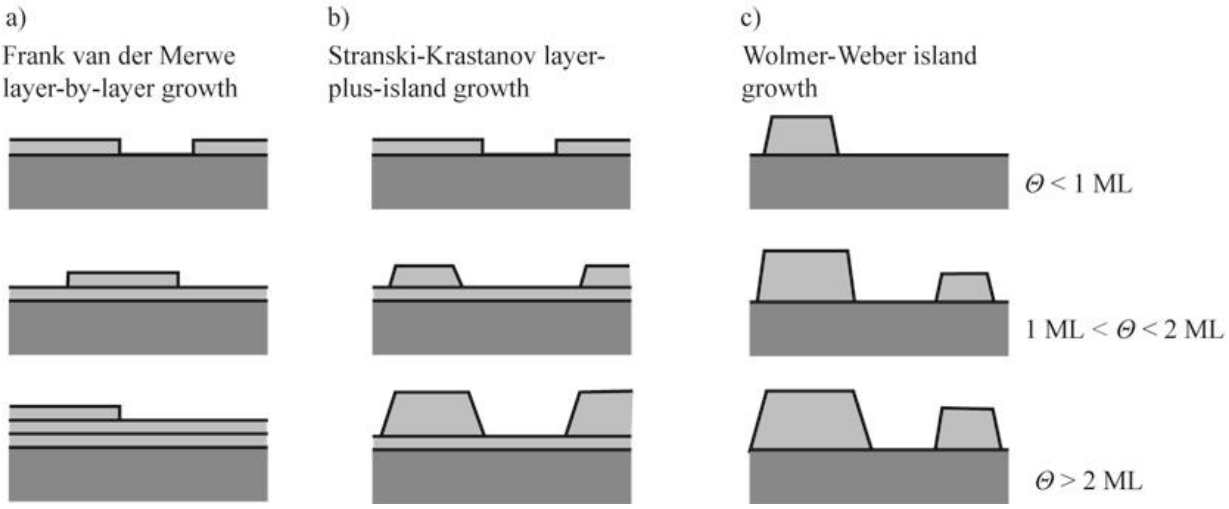

Fig. 1.17 – Schematic diagram of the three main modes of thin film growth on a surface with increasing coverage. (a) Frank van der Merwe layer-by-layer growth; (b) Stranski-Krastanov layer-plus-island growth; (c) Wolber-Weber island growth. ML = monolayer. Reproduced from [146].

When synthesising a nanoparticle system, the nucleation stage typically leads to Wolmer-Weber island growth. This is, of course, dependant on the interaction between the deposited metal precursor and the supporting material, which in turn will depend on the species of metal and supporting material used. However, at high enough loadings, there is sufficient deposited material to coat the surface of the supporting material entirely, forming a monolayer (ML). Since island growth dominates growth at low coverages, exceedingly high metal loadings such as 15 wt.% will likely result in a changeover to Stranski-Krastanov layer-plus-island growth.[147–149]

1.3.4 Other Reported Synthesis Methods

Several other, more niche, methods of multimetallic nanoparticle synthesis have been reported by other research teams. All of these methods seek to gain utmost control over the morphology, shape, size, structure, and composition of the nanoparticle in order to optimise its catalytic performance for its specific application.

1.3.4.1 Galvanic Replacement

A method of forming multimetallic nanoparticles that has gained recent attention is galvanic replacement reactions (GRR).[7] This method has gained traction for use in synthesising catalysts for several industrially important reactions.[150–157] This method involves the use of surface displacement reactions to add an additional metal to a system. For instance, adding a third metal to a bimetallic system. This generally results in a core@shell (M1@M2M3 or M1M2@M3) or pseudo-core@shell (M1M2@M1M3) structure, although metal diffusion resulting in alloying is also possible.[154]

The GRR displacement occurs between zero-valent surface metal atoms of a nanoparticle and ionic metal precursors in solution. Equation 1 summarises the reaction that occurs:

$$\mathrm{nM2} + \mathrm{mM3}^{n+} \rightarrow \mathrm{nM2}^{m+} + \mathrm{mM3} \qquad \textbf{Equation 1}$$

The driving force of this reaction is the differing reduction potentials between the surface metal and the metal cations in solution. The surface metal atom is oxidised and the metal cation in solution is reduced to its metallic state. As such, this process is surface sensitive.[155] The third metal is added only to the surface, and never enters the interior of the nanoparticle.[150] Since the process occurs gradually over time, the stoichiometry of the third metal can also be controlled.[158]

Advantages of this method include a flexible design which can be fine-tuned to provide control over morphology and elemental composition. However, if a method with poor size control, such as impregnation methods, were used to synthesise the MNP that is to be modified, the wide range of sizes will remain following GRR. Several studies have taken advantage of the control this procedure affords over the stoichiometry and structure.

Miyazaki *et al*. reported the use of GRR to add a third metal, M, to PdZn/SiO_2, controlling the stoichiometry such that Pd:Zn:M = 1:1:0.25.[150] PdZn/SiO_2 was synthesised using co-IWI, obtaining a 3% metal loading of PdZn. HR-TEM images indicated the particles were between 2 and 6 nm in diameter, with a mean of 3 nm. d-spacing analysis showed the exposed surface plane to be PdZn(010). Following addition of Pb via GRR, the mean nanoparticle size increased to 3.3 nm, and the morphology of the nanoparticle did not change. EDX mapping of the nanoparticle confirmed a pseudo-core@shell structure. Pd was dispersed throughout, Zn was

exclusively in the core, and Pb was exclusively in the shell. In this particular reaction, Pb replaced Zn and not Pd. This is due to the lower oxidation potential of Zn compared to Pd, thus Zn is able to reduce Pb^{2+} to Pb^{0}.

The $PdZn@PdPb_{0.25}/SiO_2$ catalyst was compared to the Lindlar catalyst ($PdPb/CaCO_3$) in the hydrogenation of phenylacetylene to styrene. The catalyst exhibited high activity, but importantly, superior selectivity towards styrene over the unwanted over-hydrogenation product ethylbenzene to the Lindlar catalyst.

GRR has reportedly also been used to synthesise tetra-metallic nanoparticles (TtMNPs).[159] AgAuPtPd TtMNP nanotubes were prepared via stepwise GRR procedures starting with Ag nanowires. Au, Pd, and Pt were added in that order via GRR, using CTAB as a surfactant to control growth. HAADF-STEM characterisation revealed the metals were well-mixed and catalytic testing showed this catalyst was effective in reduction of 4-nitrophenol with $NaBH_4$.

1.3.4.2 Specialised Structures

Chemical etching is a common synthesis method to obtain multimetallic nanoparticles of non-standard shape. For instance, trimetallic PtRuCu nanoframes were synthesised by Yin *et al*.[160] First, PtRuCu TMNPs were synthesised via a colloidal synthesis method, Pt, Cu, and Ru chlorides, and oleic acid and oleylamine capping agents. The mixture was heated to 473 K in a Teflon-lined stainless-steel autoclave, to form PtRuCu TMNPs with a rhombic dodecahedral shape. The PtRuCu TMNPs were dispersed in a 1:1 mixture of DMF and cyclohexane, and the etching agent, BF_4NO, was added. The mixture was centrifuged and washed with excess DMF, then activated with carbon black in DMF/acetone by sonication and dispersion in a nitrogen-saturated aqueous $HClO_4$ solution. Fig. 1.18 summarises this synthesis procedure. This resulted in hollow nanoframes preserved the shape of the original TMNPs.

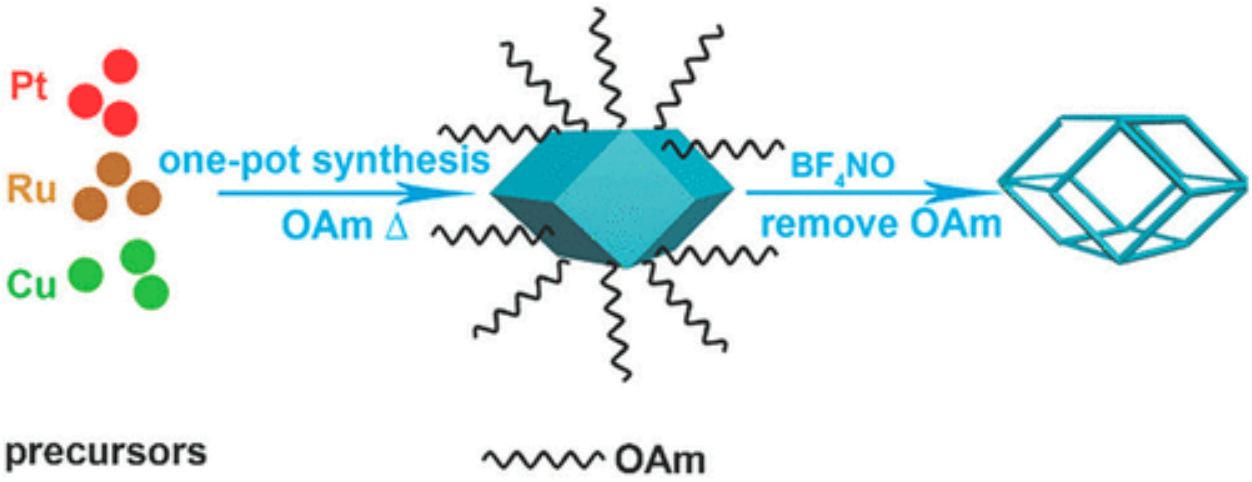

Fig. 1.18 – The synthesis scheme of a production of a trimetallic PtRuCu nanoframe in two steps. The first step is a colloidal one-pot synthesis, and the second step is an etching stage and removal of the capping agent to form a hollow trimetallic nanoframe. Reproduced from [160].

The three metals within the frame were evenly distributed. However, the Ru content was far lower than expected: the Pt:Ru:Cu ratio was 40.7:0.3:59. This was due to the mismatch in Ru lattice structure compared to Pt and Cu. Pt and Cu both adopt FCC structures, whereas Ru adopts the HCP structure.[161]

Another specialised structure, a 1-dimensional nanowire, was reported by Zhu *et al*.[162] The trimetallic nanowire (TMNW) was synthesised using a tellurium nanowire sacrificial template. An aqueous suspension of Te nanowires was charged with Pd, Pt, and Au chloride acid precursors in varying ratios. The TMNWs formed essentially by a GRR-type process. EDX mapping showed the nanowires to contain evenly-distributed metals with no measurable tellurium remaining. The TMNWs were tested for the electrooxidation of ethanol in comparison to the commercial E-TEK Pd/C catalyst. The $Au_{17}Pt_{24}Pd_{59}$ TMNWs exhibited superior activity to the commercial catalyst.

These examples are just a few of many more niche synthetic methods that have been utilised to synthesise multimetallic nanoparticles. New methods are constantly being developed all over the world in an attempt to synthesise multimetallic nanoparticles in ways that afford control over size, shape, structure, metal stoichiometry, and metal distribution in a way that traditional methods cannot.[86,163–167] In the future, many more different and niche synthetic methods will be reported.

1.4 The CO_2 Hydrogenation Reaction to Methanol

One highly important commercial industrial reaction nanoparticles have found use in is the hydrogenation of carbon dioxide to methanol.[125] The scope of this project involves the investigation of a supported multimetallic nanoparticle system for this reaction.

1.4.1 The Industrial Rationale

Due to their role in global warming, the reduction of greenhouse gases in the atmosphere is one of humanity's pressing issues.[168] Greenhouse gas reduction, particularly CO_2, has been recognised at the highest levels by leading international incorporations such as the United Nations (IPCC 2018). The need for reduction of CO_2 emissions and elimination of fossil fuels has led to an increased push to convert CO_2 to liquid fuels, including formic acid, dimethyl ether, and most notably, methanol.[169]

Methanol is one of the most important chemicals both in industry and as a commodity. In 2011, the annual global consumption of methanol was approximately 53 million tonnes.[125] Currently, the most common industrial method is to react a mixture of CO, CO_2 and H_2 (commonly known as synthesis gas or "syngas") at 50 bar pressure and 523 K over a $Cu/ZnO/Al_2O_3$ (copper-zinc-alumina, CZA) catalyst (60-120 nm).[170]

The use of CO_2 for methanol synthesis has positive implications in the sustainability of the process as a form of carbon capture. However, there is still the push for a catalyst that can work under milder conditions, such as at lower temperatures, lower pressures, and the use of less catalytic material. Chemically, the use of CZA comes with issues other than the high reaction pressure requirement. The suppression of the Reverse Water Gas Shift Reaction (RWGSR) over CZA has room for improvement. This is especially true since the formation of water as a product of the RWGSR promotes sintering of Cu, thus reducing both the long-term stability of the catalyst and the yield of methanol.[7]

The direct hydrogenation of CO_2 to methanol over metal nanoparticle catalysts has become an attractive potential alternative and improvement over the current synthesis using CZA.[125]

1.4.2 The Chemistry of the CO_2 Hydrogenation Reaction

The chemical equation for the CO_2 hydrogenation reaction is shown below (Equation 2):

$$CO_{2(g)} + 3H_{2(g)} \rightleftharpoons CH_3OH_{(g)} + H_2O_{(g)} \quad \textbf{Equation 2}$$

This reaction is in direct competition with another reaction, the RWGSR (Equation 3):

$$CO_{2(g)} + H_{2(g)} \rightleftharpoons CO_{(g)} + H_2O_{(g)} \quad \textbf{Equation 3}$$

This provides a challenge in developing a catalyst that selectively facilitates the CO_2 hydrogenation to methanol reaction while suppressing the RWGSR. In addition to the desire for milder conditions, new nanoparticle catalysts should exhibit high selectivity towards methanol and suppress the RWGSR. The selectivity towards methanol can be determined by measuring the ratio of methanol to CO produced.

The reaction of carbon dioxide and hydrogen gas over Cu/ZnO proceeds via an eight-step mechanism known as the “formate pathway”, which involves the adsorption of hydrogen and CO_2 onto the metal surface and the formation of formic acid and formate intermediates. This mechanism of the CO_2 hydrogenation reaction to methanol and the RWGSR are detailed in Fig. 1.19.[171]

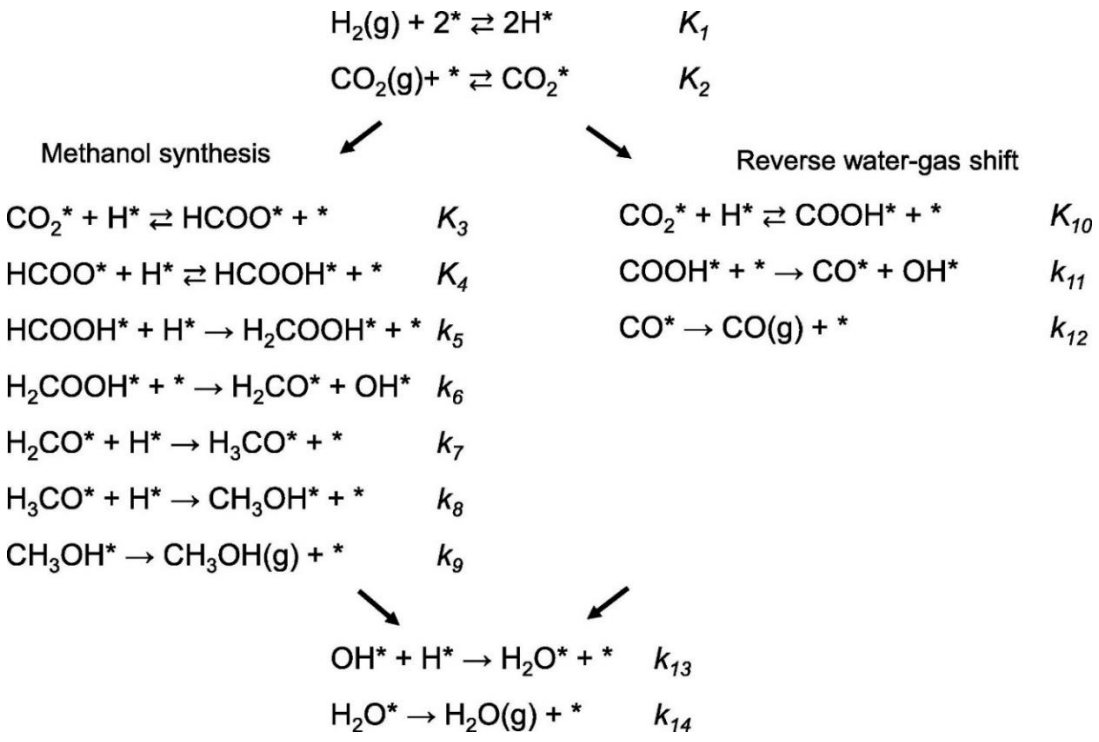

Fig. 1.19 – The reaction mechanism of the CO_2 hydrogenation to methanol via the formate pathway and the competing RWGSR. This mechanism shows each of the steps and intermediates of the reaction. Reproduced from [171].

Via the formate pathway, the rate-determining step (RDS) is known to be the hydrogenation of formic acid (k_5 in the scheme shown in Fig. 1.19). This is because formic acid does not readily accept protons (formic acid pK_b = 10.25), thus has the highest energy barrier to overcome of all the steps. For the RWGSR, the RDS is the dissociation of the carboxyl radical to CO* and OH* (k_{11}).[171]

The industrial catalyst, CZA, is a multimetallic system. It consists of Cu/ZnO (c. 60wt.% Cu) with a minor alumina component acting as a stabiliser. Specifically, Cu-Cu and Cu-Zn sites are involved in catalysing each step of the reaction. The majority of the steps are catalysed by the metallic Cu surface, as proven by previous studies on single crystal Cu(100), Cu(110), and Cu(111) surfaces, with Zn acting as a promoter.[171] However, the RDS appears to be facilitated by the stepped Cu-Zn interface, directed by synergistic electronic effects between Cu and Zn.

Reportedly, over a range of Cu particle sizes between 8.5 and 37.3 nm, selectivity towards methanol decreased at lower particle sizes, and rates of reactant conversion did not change.[172]

1.4.3 The Use of Multimetallic Nanoparticles for the CO_2 Hydrogenation Reaction

Multimetallic nanoparticles, including bimetallic nanoparticles (BMNP) and trimetallic nanoparticles (TMNP) have been investigated for their use in the CO_2 hydrogenation reaction to form methanol. These studies aim to fulfil the rationale previously mentioned, utilising milder reaction conditions than 50 bar, and using less material, while preserving or increasing catalytic performance and selectivity towards methanol. This section will detail and summarise the efforts of other research teams to investigate multimetallic nanoparticle catalysts for this reaction.

Table 1 summarises studies into several multimetallic nanoparticle catalyst systems that have been investigated. More detailed descriptions of each of these studies have been detailed below.

Table 1 – Summary of several studies into multimetallic nanoparticle systems investigated in recent years for the hydrogenation of CO_2 to methanol.

Catalyst	Catalyst Type	Reaction Conditions	TOF[a]/Activity[b]	MeOH selectivity	Ref.
$Cu/ZnO/Al_2O_3$ (CZA)	Commercial	513 K; 20-50 bar; $H_2:CO_2 = 3$; GHSV = 6,000 h^{-1}	Activity = 3.17	35%	173
CuZn/SiC	BMNP	523 K; 1 bar; $H_2:CO_2 = 9$	Activity = 0.03	5%	174
PdZn/SiC			Activity = 0.23	21%	
PdCu/SiC			Activity = 0	0%	
PdCuZn/SiC, 12.5% Pd	TMNP		Activity = 0.07	23%	
PdCuZn/SiC, 25% Pd			Activity = 0.14	40%	
PdCuZn/SiC, 37.5% Pd			Activity = 0.30	50%	
$NiGa/SiO_2$	BMNP	533 K; 10 bar; $H_2:CO_2 = 3$	TOF = 2880 Activity = 1.2	43%	175
$AuNiGa/SiO_2$	TMNP		TOF = 11160 Activity = 1.1	51%	
$CuNiGa/SiO_2$			TOF = 5040 Activity = 1.8	56%	
$CoNiGa/SiO_2$			TOF = 1800 Activity = 1.3	55%	

[a]TOF / h^{-1}; [b]Activity towards methanol formation / $mol_{MeOH}\ kg_{cat}^{-1}\ h^{-1}$.

Ramirez *et al*. investigated the use of a TMNP catalyst for CO_2 hydrogenation at atmospheric pressure. The system studied was PdCuZn/SiC with varying Pd loadings.[174] BMNP catalysts PdCu/SiC, PdZn/SiC, and CuZn/SiC were tested for comparison. These catalysts were prepared via a modified IWI method. The SiC support was macro- and mesoporous. In the case of CuZn/SiC, the pores were blocked due to the large CuZn particle size. Pd-containing BMNP and TMNPs were smaller in size, with size decreasing within increasing Pd loadings. The smallest particle size was observed with the trimetallic catalyst containing 37.5 mol.% Pd. TPR profiling of this catalyst showed Pd-Zn alloy formation at around 673 K.

In catalytic testing of each catalyst, as the reaction temperature increased, CO formation increased, indicative of a favouring of the RWGSR at higher temperatures. The PdZn/SiC BMNP catalyst favoured the RWGSR the most. In general, greater Pd

content yielded greater methanol formation in the temperature range 498-548 K. Cu-containing BMNPs performed poorly, however, Cu-containing TMNPs exhibited higher activity than BMNPs without Cu. This highlights the synergistic effects of the three metals in achieving high activity and selectivity towards methanol.

The combination of Pd, Cu, and Zn is thought to yield an effective catalyst for CO_2 hydrogenation because of a formation of the PdZn alloy, which, similar to CuZn interfaces in CZA, form an active catalytic site. It is worth noting that surface Pd^0 sites also facilitate the RWGSR due to the high H affinity on Pd surfaces. However, the presence of Cu prevents the formation of metallic Pd^0, decreasing the rate of the RWGSR and therefore increasing selectivity towards methanol.

Zhao *et al.* used computational simulations to study trimetallic PdCuAu NPs using density functional theory (DFT).[176] Calculations of these TMNPs with differing Pd:Cu:Au molar ratios showed that average bond distances within seven-atom clusters decreased as Cu content increased. Hydrogen adsorption was calculated to occur most on Pd surfaces, followed by Cu, and then Au least. As such, $Pd_3Cu_2Au_2$ clusters reportedly exhibited greatest H adsorption, thus considered most suitable amongst the formulations studied. When Pt was used instead of Pd, there was a marked shift towards the RWGSR.

Duyar *et al*. studied $NiGa/SiO_2$ nanoparticles promoted with a third metal.[175] Third metals tested were Au, Cu, and Co. By comparison, the BMNP $NiGa/SiO_2$ was also tested. The catalysts were prepared via IWI. They were tested in the temperature range of 473-543 K at pressures of 10 bar, one-fifth of the pressure used with the industrial CZA catalyst. The measured TOF value for each of these catalysts in descending order was found to be AuNiGa > CuNiGa, > NiGa > CoNiGa. The TOF of $AuNiGa/SiO_2$ at 533 K was four times greater than $NiGa/SiO_2$, at >10,800 h^{-1}. However, despite the lower catalytic activity and CO_2 conversion than AuNiGa, $CuNiGa/SiO_2$ exhibited the highest selectivity towards methanol.

Within the $AuNiGa/SiO_2$ catalyst, The Au exhibited a promotional effect, weakening the interaction between the catalyst and C and O due to the differing electron densities and binding energies of the Au-containing surface compared to the bimetallic NiGa surface. For the Cu-containing system, a CuGa phase is thought to have formed, facilitating the selectivity towards methanol. However, more work is required to

understand the intrinsic activities of different phases and form a correlation with activity and selectivity towards methanol.

Smitshuysen *et al*. also investigated Ga-containing TMNP catalysts for CO_2 hydrogenation.[177] Ni_2FeGa/SiO_2 catalysts were prepared via IWI. The addition of Ga increased the selectivity towards methanol compared to the bimetallic $FeGa/SiO_2$. However, the catalyst failed to exhibit a greater activity than CZA.

Overall, multimetallic alloyed systems are a desirable way to mitigate the issues with CZA previously discussed, such as high-pressure requirements and poor suppression of the RWGSR, thereby increasing both yield and selectivity towards methanol production.

Investigations into β-PdZn alloy formation is within the scope of this project, since this alloy has the potential to facilitate high CO_2 hydrogenation activity.[178] Beyond the scope of this project, future work could investigate the addition of a third metal, such as Cu, to aid in suppressing the RWGSR to increase selectivity towards methanol.

1.5 The Synergy of Multimetallic Nanoparticle Systems

As previously discussed, the use of multimetallic supported nanoparticle systems can provide benefits in both catalytic activity and product selectivity due to synergistic effects of the two or more metals. In this section, multimetallic nanoparticles as catalysts in the wider literature, beyond CO_2 hydrogenation, will be discussed. This includes specific examples of synergistic effects of multiple metals and how various factors such as nanoparticle shape, metal species, stoichiometry, and structure impacted the catalytic performance when used in commercially important reactions such as hydrogenations, dehydrogenations, and oxidations.[7]

1.5.1 Multimetallic Nanoparticle Systems as Catalysts for Hydrogenation Reactions

Hydrogenation encompasses a wide variety of reactions that involve the addition of hydrogen to a molecule, thus reducing the molecule.[179] A catalyst is required in such reactions to negate the need for high temperatures and pressures, and to ensure selectivity towards the product. Heterogeneous catalysts used for hydrogenation reactions include ruthenium,[180,181] nickel,[182] and Pd-based Lindlar's catalyst.[183]

Recently, a number of multimetallic, including trimetallic, examples, have been reported to address issues with selectivity and harsh reaction conditions.

1.5.1.1 Hydrogenation of CO to Higher Alcohols

An example of this is the hydrogenation of CO to higher alcohols (C_2 or higher). Higher alcohols can be blended with gasoline to improve its octane number and reduce output of harmful emissions. Although higher alcohols can be obtained using syngas, feeds are often contaminated with H_2S, which serves as a potent catalyst poison. As such, the three properties required for a catalyst for this reaction are (i) high activity towards the water gas shift reaction (WGSR), (ii) resistance to sulphur poisoning, and (iii) high selectivity towards higher alcohols over methanol, CO_2, and hydrocarbons.[7]

Monometallic MoS_2 catalysts satisfy the first two properties, but exhibit low selectivity towards higher alcohols. Adding a second metal, Rh, improves the selectivity towards oxygenates and away from hydrocarbons. Adding a third metal, Co, promotes homologation from C_1 to C_2, forming ethanol as the dominant product. In 2010, Surisetty *et al*. investigated the use of supported trimetallic CoRhMo sulphide catalysts, promoted with alkali metals.[184]

The team reported that activated carbon (AC) as a support was pH, temperature, and pressure resistant, but was prone to coking due to its microporous structure, in which its pores are easily blocked. As such, multiwalled carbon nanotubes (MWCNTs) with properties similar to AC were used. MWCNTs are mesoporous, or even macroporous, negating limitations with metal dispersion and transport.

To synthesise the alkali-promoted MWCNT-supported TMNPs, the support was pretreated with HNO_3. Through a modified IWI procedure, the K promoter (9 wt.%) was added, followed by the metal precursors.

This catalyst was tested with a wide range of temperatures and pressures. Conditions for optimal CO conversion and selectivity towards higher alcohols were 593 K and 8.28 MPa. The bimetallic formulation omitting Co exhibited a lower uptake of CO to the catalyst. CO uptake increased with additional Co up to a wt.% of 4.5%. The trimetallic CoRhMoS-K/MWCNT catalyst exhibited a higher-alcohol selectivity of 31.4%. In the equivalent reaction conditions with a bimetallic catalyst without Co, the selectivity was 24.6%. Co loadings greater than 4.5 wt.% resulted in large Co_9S_8 particle formation, decreasing the surface area and active site (CoMoS) dispersion.

For instance, the selectivity with 6 wt.% Co was lower than with 4.5 wt.% due to the reduction of active sites facilitating the selective formation of higher alcohols.

Analysis of the catalyst with TPR showed that Co not only caused an increase in CO uptake and selectivity towards higher alcohols, it also facilitated a lower reduction temperature, with greater CO conversion occurring as Co loading increased. This was ascribed to an increase in active site density.

This example shows how each of the three metals in a system can play different roles in facilitating a catalytic reaction, resulting in multiple metals exhibiting synergistic effects.

1.5.1.2 Fischer-Tropsch Synthesis

Fischer-Tropsch syntheses (FTS) involve the hydrogenation of CO to hydrocarbons. This reaction is of environmental importance since waste products such as CO and H_2 could be converted into fuel without the need for petroleum. In this reaction, syngas (a mixture of CO and H_2) in the presence of a metallic catalyst can form hydrocarbons and water through the hydrogenation of CO. This process was first developed in the 1920s by Franz Fischer and Hans Tropsch. Initially, an Fe catalyst was used. However, Co-based catalysts were later found to perform superior to form mixtures of hydrocarbons and oxygenates.[185]

In the mid-1970s, Vannice studied various transition metal nanoparticles supported on alumina as catalysts for CO hydrogenation. They found Ru/Al_2O_3 exhibited the highest activity, as well as yielding the highest molecular weight products.[186]

The monometallic transition metal on alumina catalysts produced a wide range of products, forming complex mixtures. This led to a drive to synthesise a catalyst which exhibited high CO hydrogenation activity and high selectivity towards specific products or product types.

In 2020, Badoga *et al.* investigated multimetallic supported nanoparticles for FTS.[187] The team prepared an alkali-promoted $CuFe\text{-}K/Al_2O_3$ using mesoporous alumina. These catalysts were synthesised through sequential modified IWI. First, 25 wt.% Fe was added to the alumina. After drying, 0.5 wt.% Cu was added. The catalyst was dried and calcined at 673 K for 4 hours. 1 wt.% K was added and then the product was dried and calcined again. For comparison, a monometallic Fe/Al_2O_3 was synthesised.

The catalysts were tested for FTS at 523 K and 2 MPa with a space velocity of 2000 h^{-1}. The monometallic Fe/Al_2O_3 catalyst showed high CO conversion (95%), but also a high selectivity towards the undesired WGSR product CO_2 (46.9%). Of the hydrocarbon products formed, CH_4 accounted for 34.1%, C_2-C_4 products accounted for 11.1%, and the desirable C_{5+} products, 54.8%. The alkene:alkane ratio was 0.35.

Over the promoted bimetallic catalyst, CO conversion remained high, at 94%. CO_2 selectivity was slightly lower, at 44.0%. However, of the hydrocarbons formed, selectivity towards C_{5+} hydrocarbons increased significantly to 77.0%, the CH_4 selectivity decreased significantly to 12.0%, and C_2-C_4 stayed at 11.0% In addition, the alkene:alkane ratio increased to 0.71.

Four candidates for a third metal were considered: Mn, Mg, Co, and Ni. Co was found to increase CH_4 selectivity compared to the bimetallic catalyst, to 16.8%, and reduce the alkene:alkane ratio to 0.25. When Mg was used, the selectivities were similar to those of the bimetallic catalyst, albeit a lower alkene:alkane ratio of 0.60. However, in both of these cases, the CO_2 selectivity was the same. This showed that these TMNP catalysts were not effective in suppressing the WGSR.

The TMNP formulation including Ni resulted in a lower CO conversion of 77%, but also the highest CH_4 selectivity of 29.3%. However, CO_2 selectivity reduced to 40.7%, suggesting a partial suppression of the WGSR.

The Mn-containing TMNP exhibited a 95% CO conversion. Both CO_2 selectivity and CH_4 selectivity decreased compared to that over the BMNP formulation, to 39.4% and 10.0% respectively. Moreover, the selectivity towards the desired C_{5+} products increased to 81.0%. The alkene:alkane ratio was 0.85. As such, of the TMNP formulations, $MnFeCu\text{-}K/Al_2O_3$ was superior to both the bimetallic formulation and other trimetallic formulations in CO conversion, suppression of WGSR, and production of desired products.

XPS analysis of this catalyst revealed it had the highest concentration of Fe at the surface, 40% higher than the Mg-containing catalyst. TPR and XANES analysis of $MnFeCu\text{-}K/Al_2O_3$ showed the surface Fe was reduced more readily than the bimetallic and other trimetallic catalysts. The electron-donating nature of Mn led to a strong electronic synergetic interaction between Fe and Mn which facilitated the reaction superior to the other catalysts. This synergetic effect between Fe and Mn in

combination with an increase in Fe surface sites led to a catalyst which outperformed the other catalysts for the FTS of C_{5+} alkenes.

1.5.2 Multimetallic Nanoparticle Systems as Catalysts for Deydrogenation Reactions

Dehydrogenation reactions involve the removal, or liberation, of hydrogen from a molecule. These reactions are of environmental importance in finding cleaner and more sustainable energy sources. Dehydrogenation reactions have found relevance in hydrogen storage for energy,[188] the harvesting of "stored hydrogen" from simple molecules such as formic acid,[189] alkanes,[190] and boranes.[191,192] Similar to hydrogenation reactions, heterogeneous multimetallic nanoparticle catalysts are widely used to obtain high activities and selectivities under milder conditions.[7] This section details recently reported examples of the use of these catalysts for several dehydrogenation reactions.

1.5.2.1 Dehydrogenation of Formic Acid to H_2 and CO_2

Formic acid dehydrogenation to form H_2 and CO_2 has been widely studied for its use in hydrogen storage and potential energy formation.[189] These studies involve modifications of the commercially used Pd/C catalyst.

Wu *et al*. investigated this reaction for a different purpose: generating H_2 *in situ* for the hydrogenation of nitrobenzene to aniline.[193] Industrially, aniline is an important intermediate in the production of dyes, agricultural chemicals, and pharmaceuticals.[194] These catalysts were synthesised using a novel defect-dominated shape recovery method. This method allows fine-tuning of the stoichiometry of the metals within the nanoparticle. Using this method, a third metal was added to bimetallic Pt_3Ni nanoparticles. Au, Ag, Cu, and Rh were investigated as third metals, at stoichiometries of 0.5, 2, and 8.

The base bimetallic Pt_3Ni nanoparticle exhibited a TOF of 12 h^{-1}. Among the catalysts that were prepared, $Pt_3Ni@Au_{0.5}$ was reported to exhibit the highest activity and selectivity towards the production of aniline, with a yield of 97% and a TOF of 124 h^{-1}. This was a 10-fold increase over the BMNP catalyst. An increase in Au content resulted in a diminishing of catalytic activity. The $Pt_3Ni@Au_2$ catalyst exhibited a TOF of 84 h^{-1}. With the fully defect-free, perfectly octahedral catalyst, $Pt_3Ni@Au_8$, the activity diminished to just 6 h^{-1}. Similar trends of loss of activity with increasing third

metal coverage were also observed when Ag, Cu, and Rh were used as the third metal.

This supports the published[195] hypothesis that defects can exhibit catalytic properties due to high concentrations of low-coordinate atoms: increasing the stoichiometry of the third metal resulted in a loss of defect sites, and thus a loss of catalytic activity. However, this study also highlights the importance of the species of the third metal. The activities for the catalysts where Ag, Cu, and Rh were used as the third metal exhibited far lower activities than Au-containing catalysts.

Electronic properties of $Pt_3Ni@Au_x$ catalysts have been investigated. Electronic coupling within the structure of the nanoparticle indicated electron transfer from Au to Pt, thereby reducing the Pt(II) within the nanoparticle to lower and more catalytically-active oxidation states.[196]

This study highlights the importance of stoichiometry, structure, and metal species as considerations when designing a multimetallic nanoparticle catalyst, as well as highlighting the synergistic effects that occur between specific metals.

Khan[197] demonstrated the importance of order of addition of metals in the synthesis of TMNPs, and that different synthetic methods can lead to TMNPs with the same elemental composition that have vastly different morphologies and catalytic performances. Using different orders of metal introduction, Khan synthesised unsupported core@shell TMNPs consisting of Pd, Ag, and Fe in a 1:1:1 ratio. Each TMNP had a M1M2@M3 structure. These catalysts were then tested for the dehydrogenation of formic acid to H_2 and CO_2.

PdAg@Fe TMNPs were prepared using seedless ligand-capped reduction with CTAB as the capping agent and hydrazine as the reducing agent. Separately, FePd@Ag TMNPs were prepared through stepwise addition of the metals. Aqueous Fe^{2+} was reduced with hydrazine and CTAB to Fe^0 MMNPs. To the Fe MMNP suspension, Pd^{2+} and additional CTAB were added, depositing Pd onto the Fe surface via surface displacement reaction. The FePd BMNP was isolated and redispersed in deionised water, and Ag^+ was added and reduced to form FePd@Ag TMNPs. Finally, FeAg@Pd TMNPs were synthesised by reducing Pd^{2+} and Ag^+ simultaneously onto Fe MMNPs. Differing reduction potentials of each of the metal precursor salts explained how these materials formed through the galvanic replacement reaction.

The activities for each of these catalysts for the dehydrogenation of formic acid were tested. FeAg@Pd exhibited the highest activity, with k_{obs} = 0.83 h^{-1} (corresponding to a TOF of 75 mol_{H_2} mol_{cat}^{-1} h^{-1}. This corresponded to the formation of 88 mL of product (CO_2 + H_2) in 120 minutes. By comparison, over Fe and Ag MMNP catalysts, merely 3 mL of product was formed in 120 minutes. With FePd@Ag and PdAg@Fe, the k_{obs} values were calculated to be 0.54 and 0.33 h^{-1} respectively. These rates were considerably lower than those previously reported, however, these reactions were carried out at 303 K, whereas in other reported studies, reactions were carried out at temperatures of 323 K or greater.

Activation energies of the reaction over these catalysts were calculated. Over the FeAg@Pd catalyst, the activation energy was calculated as 51 kJ mol^{-1}. Over the FePd@Ag and PdAg@Fe catalysts, activation energies were calculated as 60 and 66 kJ mol^{-1} respectively. The differences in the performances of these catalysts were due to the differing structures and electronic synergies of the metals within the nanoparticle.

This report demonstrates how different preparation methods for the same TMNP formulation can have direct and stark impacts on the catalytic performance.

1.5.2.2 Dehydrogenation of Ammonia Borane

Ammonia borane (AB), H_3N-BH_3, has gained interest as a material for hydrogen storage. This is due to its high hydrogen storage capacity, air stability, safety in transportation, and low toxicity.[198,192] The reaction studied here is the dehydrogenation of AB to liberate H_2 molecules and ultimately form BN. Many multimetallic nanoparticle catalyst formulations have thus been studied for this reaction.

Fu *et al.* investigated randomly alloyed PtAuCo TMNP catalysts.[199] Several different metal stoichiometries were investigated: $Pt_{76}Au_{12}Co_{12}$, $Pt_{76}Au_{11}Co_{13}$, $Pt_{74}Au_{21}Co_5$, $Pt_{80}Au_{16}Co_4$, $Pt_{78}Au_6Co_{16}$, and $Pt_{56}Au_4Co_{40}$. For comparison, BMNP alloys $Pt_{85}Au_{15}$ and $Pt_{86}Co_{14}$ were investigated, as well a core@shell Au@Co, and MMNP Pt, Au, and Co.

Between the TMNP formulations of different stoichiometries, TOF values varied significantly. The $Pt_{76}Au_{12}Co_{12}$ composition exhibited the highest TOF of all catalysts prepared in this studied, at 27,000 h^{-1}. Fig. 1.20a and 1.20b show the catalytic data obtained for other TMNP compositions. By comparison, of the BMNP catalysts, the

highest TOF recorded was 8,220 h^{-1}, obtained with the $Pt_{85}Au_{15}$ formulation. A separate study by Cao *et al*. reported a more active BMNP catalyst, a core@shell Ru@Co catalyst with a TOF of 20,640 h^{-1},[200] however, this is still less than the TOF obtained by the Fu study's $Pt_{76}Au_{12}Co_{12}$ composition.

In comparison to the TMNP catalysts in Fu's study, the MMNP Pt, Au, and Co catalysts performed poorly: the TOFs were in the range of 120-240 h^{-1}, more than 100 times lower than the activity obtained with $Pt_{76}Au_{12}Co_{12}$.

Data from XPS, TEM, and EDX characterisations of the TMNP PtAuCo catalysts (Fig. 1.20) show that as a result of size and orbital mismatch, Co can segregate from Pt and Au at high concentrations. In the high-Co $Pt_{56}Au_4Co_{40}$ composition, there was significant segregation of the metals. This formulation exhibited a TOF of 5,640 h^{-1}, almost five times lower than the highly-alloyed $Pt_{76}Au_{12}Co_{12}$. The segregation of the metals correlated to a decrease in catalytic activity. This was further tested via a very high-Co formulation, $Pt_{14}Au_6Co_{80}$. EDX data (Fig. 1.20e,f) showed the majority of nanoparticles were monometallic Co, with some bimetallic PtAu nanoparticle islands.

However, the stability of these catalysts over several runs of the experiment must be called into question. Significant degradation of performance was observed with each reaction cycle. This was tested via two methods: (i) the addition of more AB once H_2 formation ceased, (ii) recovering and washing the catalyst, then redispersing in a fresh AB solution. With both methods, all catalysts showed significant reductions in performance after five runs. The TOF of the $Pt_{76}Au_{12}Co_{12}$ catalyst fell to 15,120 and 21,900 h^{-1} with the two methods respectively, retaining 56% and 81% performance respectively after the fifth run. The BMNP formulations saw a TOF decrease of more than 50% after the fifth run. This showed the catalyst should be reused via washing and redispersion to retain better activity. The loss in activity has been attributed to the formation of BO_2^- in solution, which increases the viscosity of the environment and thus decreases rates of diffusion, adsorption, and desorption processes.[201]

Pt is the main component of many highly active catalysts for BA dehydrogenation. XPS measurements indicated that Pt in alloyed multimetallic nanoparticles was slightly oxidised. The electronegativity of Pt, Au, and Co respectively are 2.20, 2.54, and 1.70. The presence of the more electronegative Au results in a positive binding energy (BE) shift, whereas Co results in a negative BE shift. (Pt 4f BE = 71.34 eV for $Pt_{76}Au_{12}Co_{12}$,

71.52 eV for $Pt_{85}Au_{15}$, and 71.25 eV for $Pt_{86}Co_{14}$). The data suggested that the intermediate Pt 4f BE of the $Pt_{76}Au_{12}Co_{12}$ catalyst provided an optimal energy of interaction between the catalyst surface and the reactants and intermediates of the AB dehydrogenation reaction.

This study once again highlights the importance of ratio between the three metals, as well as electrical synergistic effects between metals to provide optimal catalytic performance superior to bimetallic and monometallic nanoparticle catalysts.

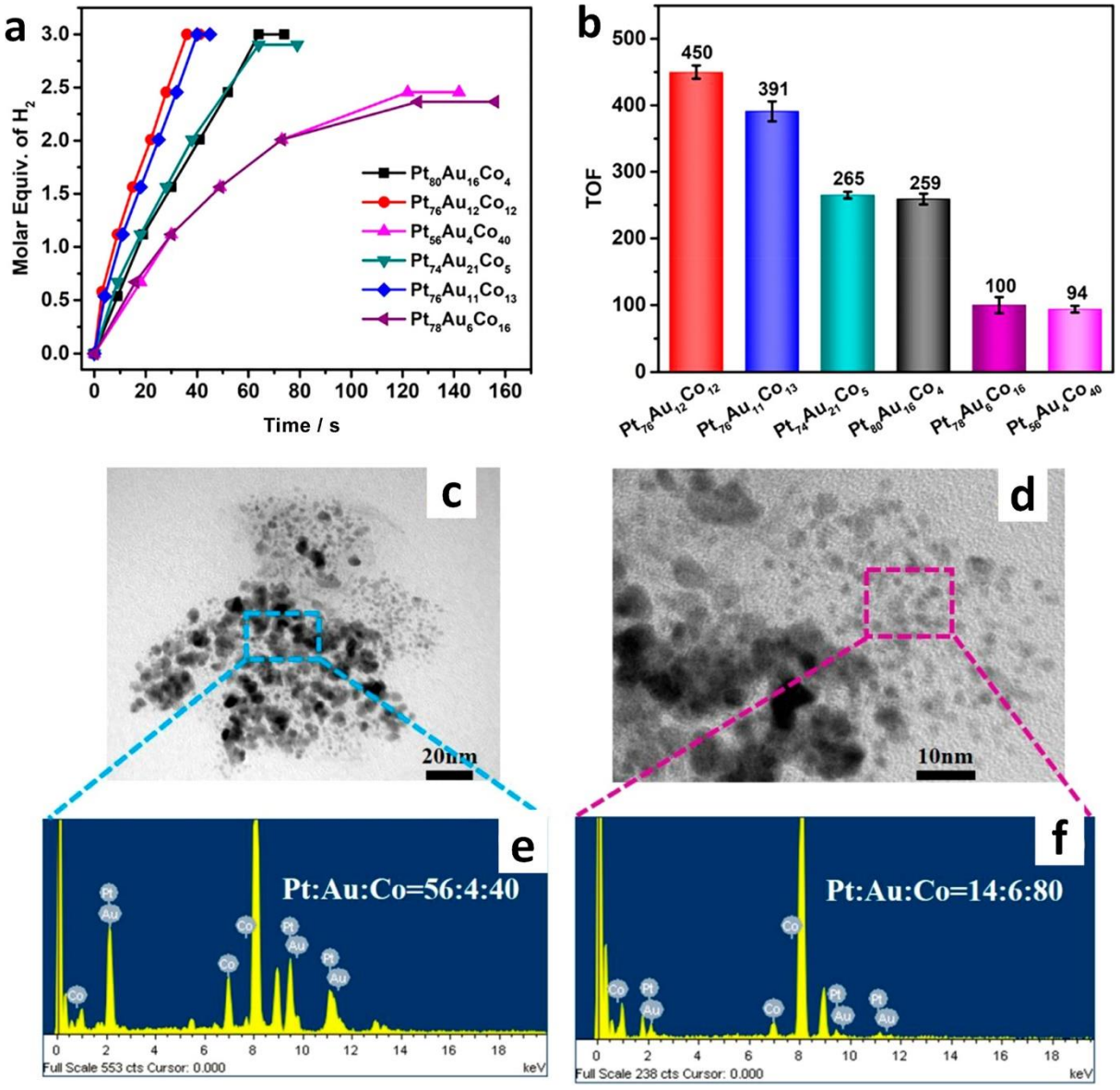

Fig. 1.20 – (a) Plots of H_2 generation with time for several PtAuCo compositions; (b) TOF values for these compositions in mol_{H_2} mol_M^{-1} min^{-1} for AB dehydrogenation reaction performed at 298 K; (c, d) TEM images of $Pt_{56}Au_4Co_{40}$ and $Pt_{14}Au_6Co_{80}$ respectively; (e, f) the corresponding EDX data highlighting the segregation of metals due to high Co concentration, and thus a reduction in catalytic activity. Reproduced from [199].

1.5.3 Multimetallic Nanoparticle Systems as Catalysts for Oxidation Reactions

Oxidation reactions are crucial in sustainable and green processes and production of key chemicals in industry. However, these reactions often exhibit low selectivity and difficulty in controlling the outcome. As such, careful catalyst design is required for such reactions.[202] Oxidation reactions of alcohols and polyols often use Au and Pd-based catalysts.[203–205]

1.5.3.1 Oxidation of Glucose and Alcohols

Oxidation of abundant molecules such as glucose can generate important intermediates used in food and pharmaceuticals. Currently, glucose oxidation is typically carried out using enzymatic catalysts.[7]

Zhang *et al*. reported that polymer-protected $Au_{70}Pt_{20}Ag_{10}$ TMNPs exhibited high catalytic activity for aerobic glucose oxidation, 20,090 $mol_{glucose}\ h^{-1}\ mol_M^{-1}$, 3.8 times higher than that of monometallic Au, with reaction conditions of 333 K and 1 bar for 2 hours.[206] This average particle diameter was 1.5 nm and was synthesised using the SI method, with PVP as the protecting agent.

It was reported that small particle size and synergy, specifically electronic charge transfer, between the elements contributed to higher activities in comparison to MMNP and BMNP formulations used for this reaction. Ag was able to donate electronic charge to Au and Pt, since the ionisation energies of Ag, Au, and Pt are 7.58, 9.22, and 9.02 eV respectively, as demonstrated in Fig. 1.21a. Compared to a bimetallic system where there was only one route for charge transfer, the trimetallic system exhibited two modes of charge transfer: (i) Ag to Au; (ii) Ag to Pt. This was supported by XPS measurements and DFT calculations, which indicated the presence of partially negatively charged Au atoms, which were thought to serve a crucial role in glucose oxidation. Zhang *et al*. also noted that the catalysts retained 70% activity after four catalytic cycles.

Data from this study, illustrated in Fig. 1.21b, also highlighted the importance of ratio between the three metals. For instance, $Au_{90}Pt_5Ag_5$ exhibited activity rates comparable to that of monometallic Au.

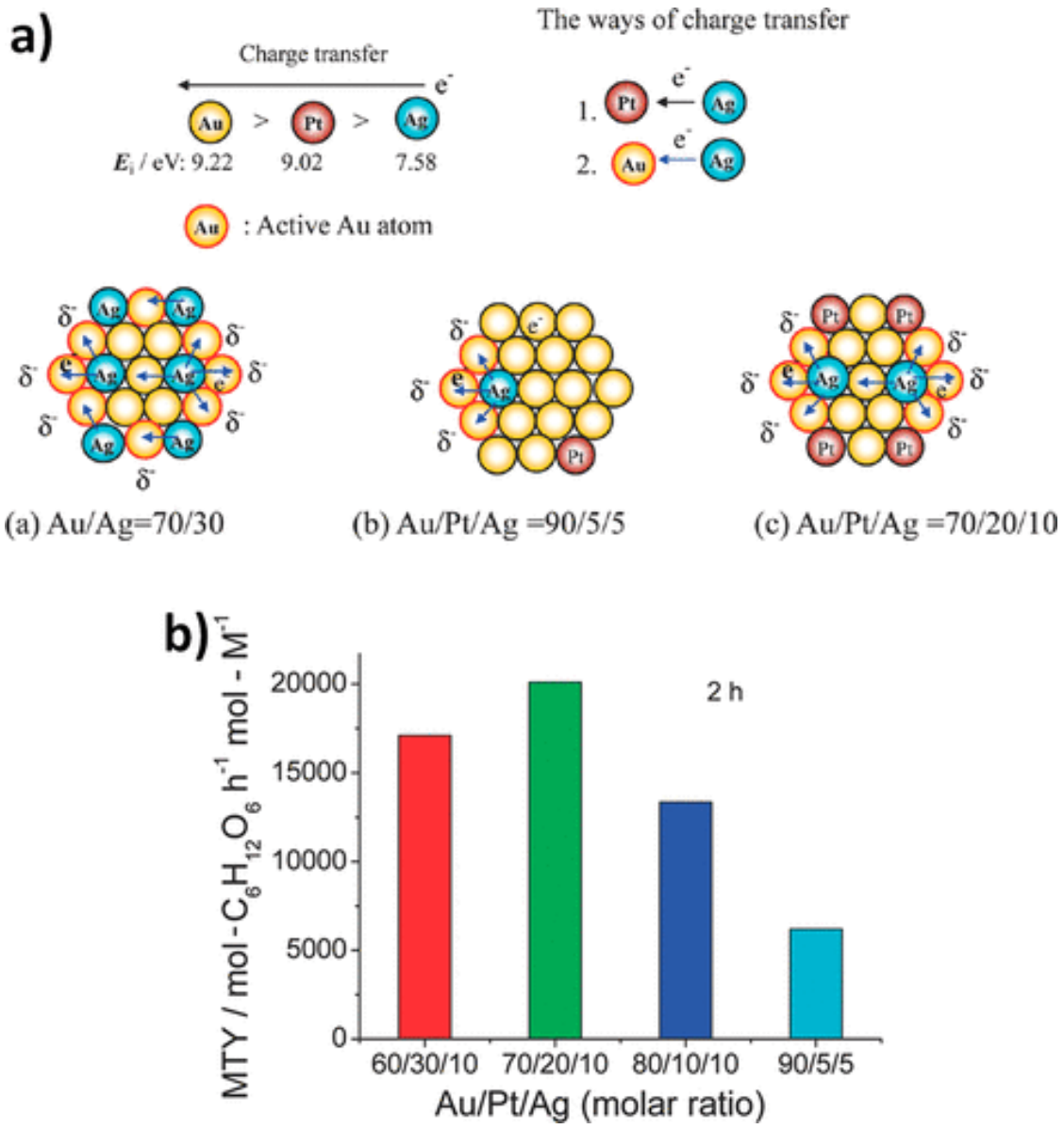

Fig. 1.21 – (a) Illustrations of electronic charge transfer modes between AuAg and AuPtAg MNPs, highlighting the partial negative charges on Pt and Au from Ag atoms; (b) Metal time yield (MTY) of four different Au:Pt:Ag ratios, highlighting the importance of tuning the ratio between the metals to optimise the synergistic effects between the metals. Reproduced from [206].

Subsequently, Zhao *et al*. probed the origins of the synergy.[207] Their study investigated AuPdPt TMNPs. In this case, the Pd provided the electron density to Pt and Au. DFT calculations on a simulated $Au_{37}Pt_{12}Pd_6$ cluster reported Mulliken charges of the elements within the nanoparticle to be -0.035 for Au, -0.024 for Pt, and +0.168 for Pd. The induced slight negative charge on Au atoms could activate O_2 molecules by donating electron charge into the antibonding orbitals for O atoms to form a superoxo

radical, a highly active oxygen species which would readily react with glucose. The reaction in turn would then be facilitated by the Pt and Pd sites.

Similar to Zhang *et al*.'s study, this study experimented with several different stoichiometries to optimise this synergistic effect. The optimal stoichiometry was reported to be $Au_{60}Pt_{10}Pd_{30}$ with a glucose oxidation rate of 26,430 $mol_{glucose}$ h^{-1} mol_M^{-1}, more than five times greater than monometallic Au and 15% greater than the most active BMNP formulation, $Au_{60}Pt_{40}$.

1.5.3.2 Oxidation of CO to CO_2

CO is a well-known highly toxic gas and environmental pollutant with well-documented environmental and health-related issues. CO oxidation is an important research area because it can be applied to methanol synthesis,[208] the WGSR,[209] and vehicle exhaust controls.[210]

Haruta *et al.* reported excellent activity when Au and Pt MMNPs supported on a metal oxide were less than 5 nm in diameter.[211] The interface between the MNP and the supporting material reportedly facilitated highly active catalytic activity. The synergy between the supporting material and the MNP has generated interest in further improving activity by adding additional metals.

Yang *et al*. synthesised PtNiCo/C TMNPs using polyol colloidal methods.[212] CO conversion rates followed the trend series PtNiCo/C > PtCo/C > PtNi/C. Pt was reportedly the main active site, but the combination of the three metals led to enhanced activity and stability in comparison to MMNP and BMNP counterparts. Ni increased the stability, whereas Co acted as a promoter, increasing the activity. The three metals were alloyed, and the intimacy of the metals provided highly active sites for oxygen activation and adsorption and activation of CO and O_2 on the surface.

Tripathi *et al*. studied a TMNP system computationally, using DFT to model a 55-atom $Pt_{31}Ni_{12}Co_{12}$ FCC catalyst.[213] The system resisted poisoning with CO, however, the oxidation activity of CO was inferior to PtNi. Occupancy of the d states and d-band centre position were used to determine the optimal metal ratio of Pt:Ni:Co. This revealed that lowering the back-donation was key to lowering the CO binding energy. This highlights the trade-off between oxidation activity and limiting CO poisoning. Further work will be necessary to determine the optimal stoichiometry.

1.5.4 Summary

The examples detailed in this section in the wider literature showcase how multimetallic nanoparticles can be used as catalysts in a wide array of different industrially important reactions. These studies have shown how the expansion from monometallic to multimetallic nanoparticles can result in drastic increases in catalytic activity and selectivity towards the desired product. These studies have all shown how multiple metals in a system can have multiple modes of synergistic effects that were introduced in previous sections which facilitate the benefits of multimetallic nanoparticles. However, these studies have also outlined challenges in synthesising, fine-tuning and optimising these catalysts that were previously discussed, and how small changes or deviations from the optimum can dramatically reduce activity owing to the loss of the optimised, synergistic interaction between the catalyst and the reactants and products that facilitated the increased activity.

In future, many more studies will be published further optimising and discovering more applications for multimetallic NPs in the chemical industry. The number of publications, following current trends, is set to increase in the coming years.[7]

1.6 Rational Synthesis of Multimetallic Systems via Strong Electrostatic Adsorption

As previously discussed, conventional methods of synthesising supported nanoparticle systems, such as IWI and co-precipitation, leave much to be desired in terms of control over morphology, shape, and size of the nanoparticle. This is especially true when synthesising multimetallic nanoparticle systems. In the widespread search for rational synthetic methods which afford greater control over the critical parameters of a supported multimetallic nanoparticle system, John Regalbuto has developed a highly rational synthetic method, known as Strong Electrostatic Adsorption (SEA).[214] His seminal research, first published in 2007, is the foundation of the experimental scope of this project.

1.6.1 Introduction to SEA

SEA is a type of impregnation procedure that typically yields small (~1 nm) nanoparticles. Ideally, the nanoparticles are well dispersed and of highly controlled size and can be applied to a wide range of metals and supporting materials.

Experimentally, this procedure revolves around adjusting the pH to optimise electrostatic interaction between charged metal complexes in solution and the supporting material. This results in adsorption of the metal complex to the supporting material, referred to as “metal uptake”. This is followed by a heat treatment under reducing conditions (typically hydrogen gas) to form the supported metal nanoparticles.

The general format of the experimental procedure is as follows:

1. Determine the Point of Zero Charge (PZC) of the supporting material’s surface via titration methods.
2. Perform a metal uptake survey using a range of different pHs and use elemental analysis to determine the uptake based on initial and final concentration of metal in solution after contact with the supporting material.
3. Determine the temperature of reduction of the adsorbed metal precursor under flowing reducing gas using temperature programmed reduction (TPR).
4. Perform the impregnation at the pH of optimal uptake, scaled up from the uptake survey, and reduce at optimal temperature determined by TPR analysis.

Metal oxide surfaces consist of terminal hydroxyl groups which, in aqueous suspension, are amphoteric in nature.[215] Whether or not the hydroxyl groups are protonated ($-OH_2^+$) or deprotonated ($-O^-$) depends on the pH of the aqueous environment. The pH at which the hydroxyl groups are neutral (-OH) is referred to as the *point of zero charge* (PZC). The PZC is a property intrinsic to each supporting material which can be determined experimentally.[216]

Below the pH of the PZC, the hydroxyl groups become protonated, and the surface becomes net positively charged. Above the PZC, the hydroxyl groups become deprotonated, and the surface becomes net negatively charged. When the surface becomes charged, electrostatic interactions between the surface and a charged metal precursor of the opposite charge can occur.

Fig. 1.22 demonstrates an example of the surface-metal interaction when adsorbing charged platinum complexes onto an oxide surface.

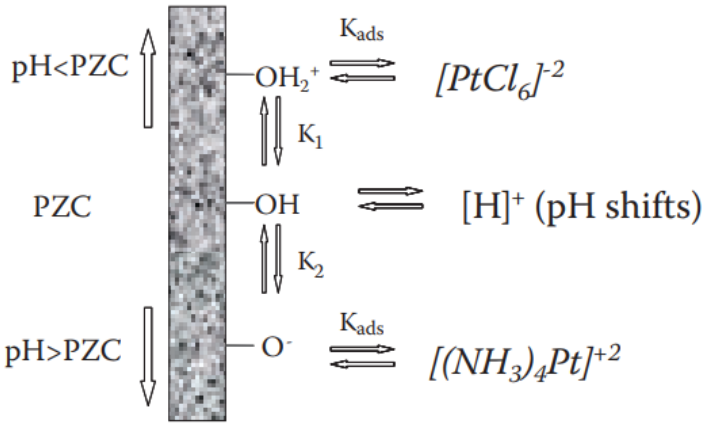

Fig. 1.22 – Diagram showing the charged states of the metal hydroxyl group when the pH of the aqueous environment is at, above, and below the PZC of the oxide surface. This diagram also shows which platinum metal complex can be adsorbed via electrostatic interaction at pH above and below the supporting material PZC, which opposes the charge of the surface hydroxyl groups. Reproduced from [217].

In this example, below the PZC when the surface exhibits a net positive charge, a negatively charged platinum complex, $[PtCl_6]^{2-}$ (chloroplatinic acid, CPA) can be adsorbed via electrostatic interactions onto the surface of the oxide. On the other hand, above the PZC when the surface exhibits a net negative charge, a positively charged complex, $[Pt(NH_3)_4]^{2+}$ (platinum tetraammine, PtTA), can be adsorbed.

The PZC of the supporting material will determine the type of metal precursor that will be used in the uptake survey and subsequent full-scale impregnation. If the PZC is above 8.00, the material is considered a high-PZC support. Below 6.00, a low-PZC support. If the PZC was in between 6.00 and 8.00, it is considered a mid-PZC support.

The surface of a low PZC support will become negatively charged at high (basic) pH values and will therefore attract cationic metal complexes. Conversely, the surface of a high PZC support will become positively charged at low (acidic) pH and will attract anionic metal complexes.

The supporting material-metal complex interactions at low and high pH are summarised in Table 2. This information is required to determine the choice of precursor and range of pH values for the metal uptake survey. For instance, a supporting material with a PZC of 4 will not adsorb an anionic metal complex, even at a high pH.

Table 2 – Summary of interactions between high and low-PZC supporting materials at different pH solutions.

	Low PZC Support	**High PZC Support**
Low pH Solution	No metal uptake	Anionic metal complexes adsorbed
High pH Solution	Cationic metal complexes adsorbed	No metal uptake

1.6.2 SEA for Multimetallic Nanoparticles

Not only can SEA be used to synthesise supported MMNPs, this procedure can be expanded to synthesise supported multimetallic nanoparticle systems.[214,218–223]

For the synthesis of multimetallic nanoparticles, such as BMNPs, there are two types of SEA that can be applied: Co-SEA, and sequential SEA (Seq-SEA). These procedures are outlined in Fig. 1.23.

Fig. 1.23a shows how the traditional impregnation method Dry Impregnation (DI) leads to larger, more agglomerated nanoparticles where metals A and B are often segregated.

Fig. 1.23b shows how co-SEA can be performed. In this example, a negatively-charged surface can simultaneously adsorb cations of metals A and B. Following H_2 reduction at high temperature, alloyed BMNPs form that are smaller and more dispersed than those obtained from DI.

Finally, Fig. 1.23c shows how SEA can be carried out sequentially. For instance, metal A can be adsorbed and reduced (or oxidised) to form a MMNP. The nanoparticle will form a surface in its own right, with its own PZC that differs from that of the supporting material. Using the metal A–support system as a new supporting material, the precursor for metal B can be deposited separately through a second SEA cycle.

Following H_2 reduction at high temperature, a core@shell structure is formed. Further reduction and heating can cause alloying of the metals.

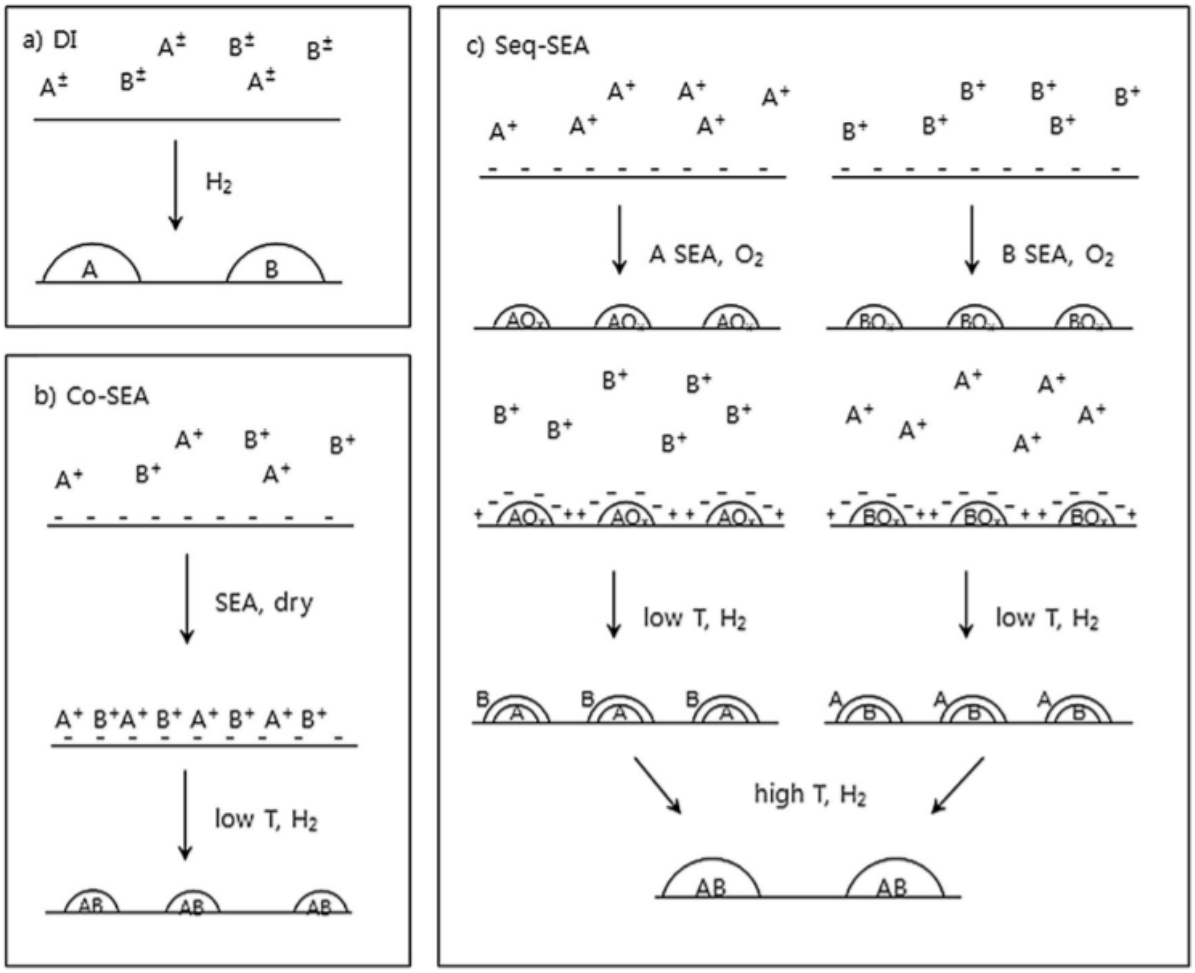

Fig. 1.23 – Diagram showing the two SEA methods that can result in BMNPs. In comparison, dry impregnation (DI) is also included. Reproduced from [214].

1.6.3 The Chemistry of the Procedure

At its core, SEA relies on metal complex-supporting material interaction. Specifically, electrostatic adsorption between metal precursors and the surface of the supporting material. This increased interaction between the metal and supporting material, which is much weaker with the traditional impregnation methods, affords the increased control over the crucial parameters of designing a supported multimetallic nanoparticle system.[217]

1.6.3.1 Metal Complex-Oxide Surface Electrostatic Interaction

This method mainly utilises metal oxides as the supporting material, although other materials such as oxidised carbon may also be used.[214] For the purposes of this section and throughout the scope of the project, metal oxides will be discussed.

The extent of adsorption may be limited by the maximum density of packing. For example, as shown by Fig. 1.24, CPA adsorbs as a close-packed monolayer retaining one hydration sheath, which corresponds to 1 complex per nm^2 (1.6 µmol m^{-2}). The PtTA complex, on the other hand, retains two hydration sheaths surrounding the complex, which limits its maximum packing density to roughly 1 complex per 2 nm^2 (0.86 µmol m^{-2}).[224]

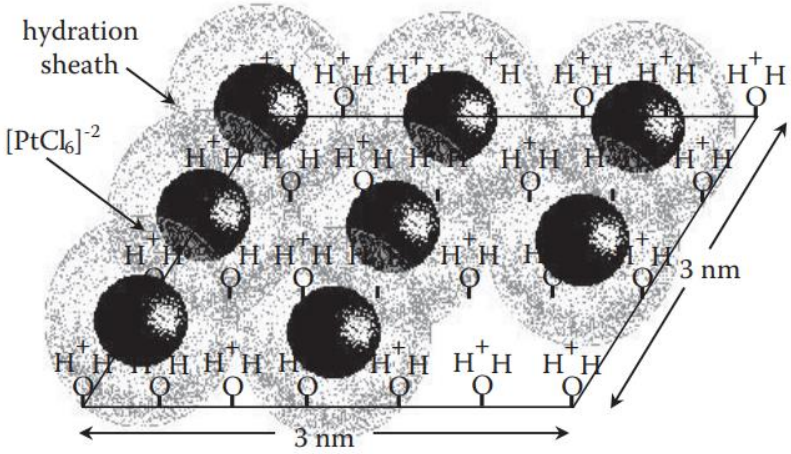

Fig. 1.24 – Adsorption of the anionic CPA complex on a protonated oxide support, displaying a single hydration sheath. Reproduced from [217].

Fig. 1.25 shows the typical uptake profile of a metal precursor over an oxide supporting material with changes in pH.

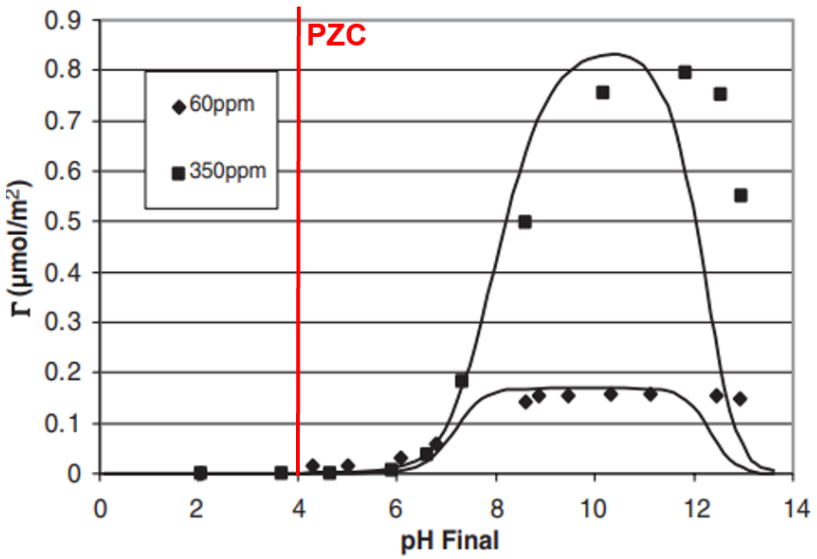

Fig. 1.25 – An example of an uptake profile of a metal oxide, in this case PtTA, onto amorphous silica (PZC=4). Two different concentrations of metal complex are displayed. The x-axis unit, pH final, takes into account pH shift caused by the addition of silica. Modified from [217].

The metal uptake, Γ, is measured in µmol of metal adsorbed per m^2 of supporting material surface area. Its value is obtained using Equation 4:

$$\Gamma_M\ (\mu\text{mol m}^{-2}) = \left(\frac{10^6\ \mu\text{mol mol}^{-1}}{\text{Surface Loading}\ (\text{m}^2\ \text{L}^{-1}) \times \text{M A}_r\ (\text{g mol}^{-1}) \times 10^3\ \text{mg g}^{-1}}\right) \times \left([\text{M}_{\text{initial}}] - [\text{M}_{\text{final}}]\ (\text{mg L}^{-1})\right)$$

Equation 4 – Equation that determines the metal uptake. M=Metal. For more on surface loading, refer to Equation 5.

The example displayed in Fig. 1.25 uses the cationic PtTA complex and amorphous silica. The PZC of the silica is 4. In an aqueous environment above a pH of 4, the surface hydroxyl groups become deprotonated. The extent of deprotonation increases the further above the pH of the aqueous environment is. In this example, at a final pH of 6, the extent of deprotonation and consequent negative charging of the surface is low, thus the uptake of PtTA onto the surface is accordingly low. As pH increases, however, extent of deprotonation and net negative charge increases, causing an increase in uptake of PtTA. However, once the pH of the solution increases past a certain point, the ionic strength of the solution becomes significant and this has a screening effect between the oxide surface charge and the metal complex.[224,225]

1.6.3.2 Oxide pH Buffering

When discussing the concentration of metal oxide in solution, a parameter known as *surface loading* (SL) is used. The surface loading is defined as the surface area of oxide per volume of solvent, as shown by Equation 5:

$$\mathrm{SL_{oxide}\ (m^2\ L^{-1})} = \frac{\mathrm{Mass_{oxide}\ (g)} \times \mathrm{SA_{oxide}\ (m^2\ g^{-1})}}{\mathrm{Vol_{solvent}\ (L)}}$$

Equation 5 – Definition of surface loading (SL) with respect to mass and surface area (SA) of the oxide, and volume of the solvent.

When a metal oxide is added to water or an aqueous solution, a shift in pH towards the PZC of the oxide occurs. This shift increases with the surface loading of the oxide, tending towards the PZC. The extent of pH shift can be measured using a process known as mass titration.[217] This process can also be used to experimentally determine the PZC of the oxide. At very high surface loadings of at least 5000 $m^2\ L^{-1}$, the pH will be shifted to the PZC at a wide range of initial pH values. The range of initial pH values that are shifted to the PZC is known as the *plateau*. As the surface loading of the metal oxide increases, the width of the plateau increases, as seen in Fig. 1.26.

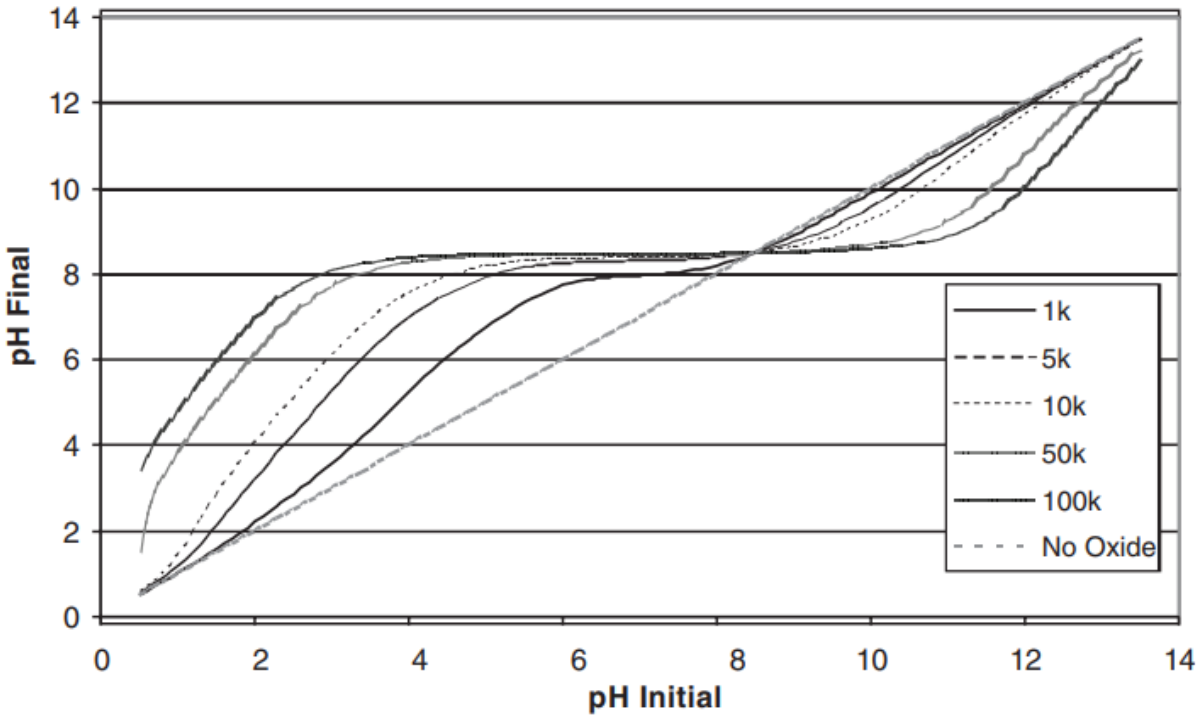

Fig. 1.26 – The pH shift of aqueous pH-adjusted solutions with increasing surface loading of an oxide, in this case, alumina. Reproduced from [217].

A surface loading of 1000 m^2 L^{-1} of alumina does not cause a significant plateau. However, at higher surface loadings, in particularly 100,000 m^2 L^{-1}, the plateau is reached at a wide range of initial pH values. Practically, surface loadings in the 5000-10000 m^2 L^{-1} range are sufficient for determining the PZC of an oxide.

When performing an uptake survey of deposition of metal complexes on an oxide surface, surface loadings of approximately 500 m^2 L^{-1} are used. This is sufficient to cause a significant shift between the initial and final pH. As such, a separate mass titration should be carried out at this concentration to anticipate what the pH shift and thus the final pH would be at a given initial pH. Alternatively, further pH adjustments can be made after the addition of the oxide to afford more control over the final pH.

1.6.4 Advantages and Disadvantages of SEA Compared to Impregnation

The main advantage of SEA against traditional impregnation methods is the improved control over particle size and morphology. Fig. 1.27 highlights the advantages and disadvantages of IWI (known as “dry impregnation” in the figure), wet impregnation, and SEA.

Types of Catalyst Impregnation

Type of impregnation	Distinguishing characteristics	Advantages/disadvantages
Dry impregnation (DI)*	Use sufficient metal solution to fill pore volume of catalyst support; adjust metal concentration for desired weight loading	A: Simplest to employ; no filtering; metal content is fixed D: Strong precursor-support interaction is not guaranteed
Wet impregnation (WI)	Amount of solution in excess of pore volume of support; precursors that interact weakly with support are washed/filtered away	A: Mixing is improved D: Filtering required; metal loading must be measured; metal wasted if it does not strongly interact with support
Strong electrostatic adsorption (SEA)**	Excess solution; pH held at optimal value for strong precursor interaction with support	A: Strong; monolayer adsorption of metal precursor D: Optimal pH must be determined and achieved during preparation

Fig. 1.27 – A brief overview of the two types of traditional impregnation: IWI (known as “dry impregnation” here), wet impregnation, and SEA. Some advantages and disadvantages of each have been highlighted. Reproduced from [217].

SEA, in addition to the greater control over morphology and size, affords less potential for material “wasted” over traditional impregnation methods, since the interaction between the supporting material and the metal precursors is far greater as a result of the electrostatic interaction. Whereas impregnation reactions can be seen as “crude”,

SEA provides a much more rational synthesis method for multimetallic MNP synthesis, which allows a high degree of fine-tuning.[214]

However, one of the main disadvantages of SEA is that an optimal pH must not only be determined beforehand, which can only be determined experimentally, but the pH must be achieved and maintained during the procedure, with information on pH shifts needing to also be determined experimentally. In addition, the PZC value must be determined for each new support. This becomes more of an issue when investigating addition of a second metal during a seq-SEA procedure, in which the PZC of the MMNP/support complex also needs to be determined. This requires a large quantity of this material to obtain the high surface loadings required to determine PZC. This extra data that must be obtained increases the length of experimental time to obtain results and catalytic data. Finally, sourcing certain anionic or cationic precursors for certain metals can be a challenge since they may not always be readily available.

However, the potential gain of control, small particle sizes, and rational addition of a second metal make this procedure an attractive possibility for catalyst design for the CO_2 hydrogenation reaction despite the drawbacks of extra experimental data required.

1.6.5 Reported SEA-Synthesised Catalysts

There have been several reported applications of multimetallic catalysts that were synthesised via this method. Thus far, all these catalysts have been bimetallic.

Regalbuto's seminal research involved the rational synthesis of PdPt BMNPs on a range of supporting materials.[214] This synthetic method, published in 2015, chronicled how SEA could be applied to BMNP synthesis.

Uptake surveys of Pd and Pt individually were carried out on SiO_2, Al_2O_3, oxC, and C, as shown by Fig. 1.28. These datasets show the typical "volcano" plot expected with an uptake survey, and a clear optimal value for final pH.

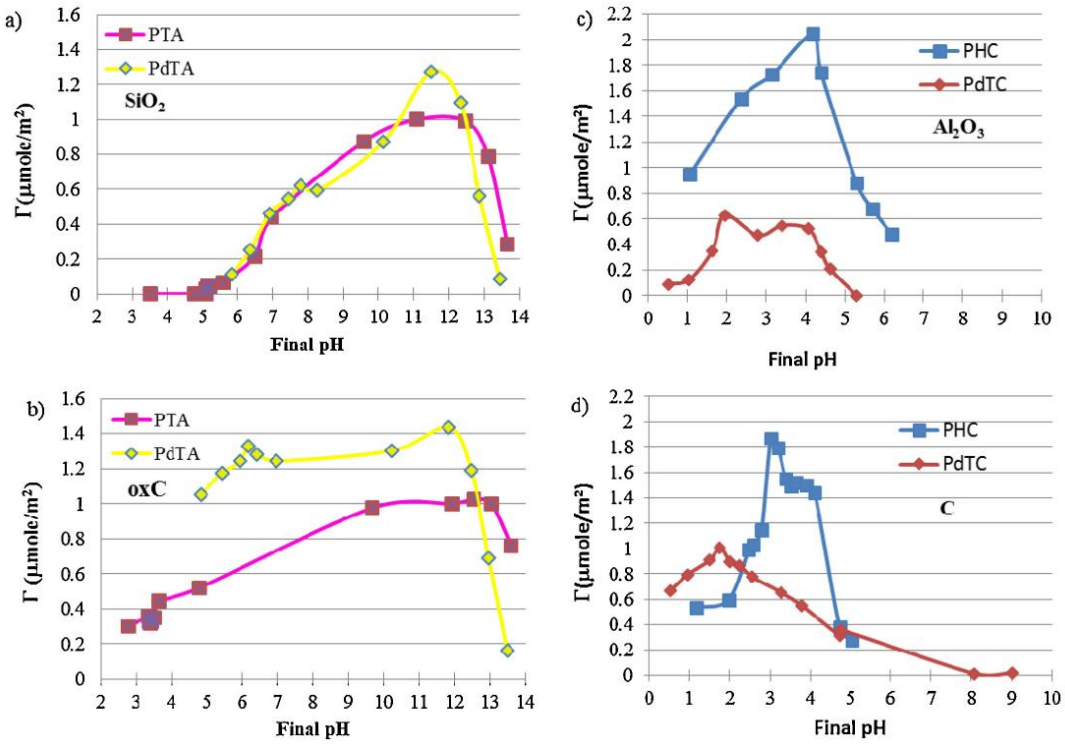

Fig. 1.28 – Uptake survey results of Pd and Pt tetraammine on a range of supporting materials. PTA=Pt tetraammine; PdTA = Pd tetraammine; PHC = Pt hexachloride; PdTC = Pd tetrachloride. Reproduced from [214].

These plots also highlight the difference between high and low PZC supporting materials. SiO_2 and oxC (Fig. 1.28a,c) are low-PZC supports, whereas Al_2O_3 and C (Fig. 1.28b,d) are high-PZC supports. As such, Pd and Pt tetraammine (PdTA, PtTA) experienced high uptake at high pH on SiO_2 and oxC, and Pt hexachloride (PHC) and Pd tetrachloride (PdTC) experienced high uptake at low pH on Al_2O_3 and C.

BMNP PdPt catalysts were prepared via seq-SEA and co-SEA. Co-SEA yielded well-dispersed and homogeneous PtPd alloys of size 1-2 nm. With seq-SEA, core@shell particles were formed. Additional cycles of SEA of the second metal increased the metal loading of the shell, affording some flexibility to the composition of the catalyst, albeit with more experimental steps. Particle sizes increased with each SEA cycle, reaching 3 nm at maximum loading. By comparison PdPt BMNPs were prepared via IWI. These particles were large and non-homogeneous.

In 2010, D'Souza and Regalbuto published an article in which PtCo/C and PdCo/C alloyed and core@shell BMNPs were prepared using SEA.[221] First, Co_3O_4 was added to C by addition of cobalt nitrate followed by calcination at 673 K, forming Co_3O_4/C, which was measured to have a PZC of 7 and a surface area of 60 m^2 g^{-1}. PdTA and

PtTA were used as Pd and Pt precursors. Uptake surveys showed no uptake of PdTA and PtTA onto C directly, so all uptake was on the Co_3O_4 surface. Uptake surveys showed the optimal uptake occurred at a final pH of 11. Following impregnation at this pH, the samples were reduced in H_2/Ar.

TEM imagines showed all particles of PtCo/C and PdCo/C were found to be 1-3 nm in diameter. EDX showed that a series of particles reduced at 773 K, PtCo/C formed an alloy. When PdCo/C was reduced at a lower temperature of 473 K, a core@shell morphology was observed, with a Co core and a Pd shell.

These catalysts could be used in electrochemical processes, however the article did not detail any specific reaction nor provide any catalytic information.

In 2022, De Castro *et al*., including Regalbuto, synthesised alloyed PdCu/SiO_2 BMNPs prepared by co-SEA.[223] The procedure resulted in very small BMNP PdCu alloys at low dilutions, and MMNP Pd clusters at high dilutions.

Independently of Regalbuto, in 2021, Ma *et al*. reported the use of SEA to synthesise intermetallic PtCo/C BMNP catalysts smaller than 3 nm in size for use in oxygen reduction reactions (ORR).[222] SEA was useful for catalyst design for this reaction, which requires very small nanoparticles. The team reported IWI led to lack of control over particle size, with large particles and no long-range order of the metals.

The team used the co-SEA method. They reported C as a high-PZC support, thus using anionic chloride complexes of Pt and Co, $[PtCl_6]^{2-}$ and $[CoCl_4]^{2-}$, respectively, in a 1:1 Pt:Co molar ratio. Optimal final pH values were reported to be pH 0.5. Samples were reduced in 5% H_2/Ar at 573 K. TEM imaging confirmed particle sizes of 2 nm on average when synthesised at pH 0.5, and XRD data showed homogeneous alloying between Pt and Co; the main reflection at a 2θ value of 39° was assigned as PtCo(111). The team reported that different pH values (0.5-3) resulted in different morphologies and different particle sizes, which particle size increasing with pH, reaching a mean of 4.4 nm at pH 3.

The sub-3 nm intermetallic PtCo/C catalyst was found to have enhanced activity, and importantly, enhanced stability over other catalysts for the ORR reaction, showing a mere 3% loss in activity over 10,000 reaction cycles. The team hypothesised that this procedure could be applied to many other formulations for the ORR reaction. This

study exemplifies how SEA can be applied to highly rational and controlled synthesis of a multimetallic catalyst for a specific industrial reaction.

1.7 Aims and Objectives

The aims and objectives for the experimental section of this project will be to investigate and evaluate the use of Regalbuto's highly controlled and rational SEA synthesis for multimetallic nanoparticles. These will be applied to the hydrogenation of CO_2 to methanol.

The experimental section will involve synthesis of BMNP catalysts via SEA and other methods. Information such as PZC and optimal reduction temperatures will be determined experimentally. Characterisation of these catalysts through an array of techniques such as XRD, XPS, imaging using electron microscopy, and EDX, to gain insight into the catalysts produced via the synthesis methods will be carried out. Finally, these catalysts will be tested to determine their activity towards CO_2 hydrogenation, and selectivity towards methanol. Following this, an evaluation will be given about the viability of the SEA method for synthesising multimetallic nanoparticle catalysts for the CO_2 hydrogenation reaction.

2 Experimental

This section details the experimental procedures, as well as the characterisation techniques used throughout the project. All chemicals used were sourced from Sigma-Aldrich, Merck, or American Elements.

2.1 Strong Electrostatic Adsorption Procedures

The Strong Electrostatic Adsorption procedure consisted of four main stages. The first was to determine the PZC of the supporting material. The second was to determine the pH of optimal uptake of the metal complex to the supporting material through the use of uptake surveys. Thirdly, the reduction temperature of the metal complex was determined via TPR. Finally, a scaled-up impregnation was carried out at the optimal pH determined by the uptake survey.

2.1.1 Determining the Point of Zero Charge

For each supporting material, or separate batch of supporting material, the first stage in determining the PZC was to find the material's specific surface area. This would be required to calculate the appropriate surface loading, and to determine if the support exhibited a high enough surface area for use in SEA. For practical purposes, a surface area of at least 40 $m^2\ g^{-1}$ would be required for this procedure.

The surface area of the supports were measured using nitrogen adsorption and BET surface area analysis. The Nova Quantachrome 2200 was used in order to take these measurements. At least 200 mg of supporting materials were weighed out and placed into a 9 mm glass tube with bulb. The supporting materials were first degassed at a temperature of 453 K and a pressure below 150 torr for 3 hours. For analysis, the samples were cooled to 77 K using liquid N_2 as a coolant. Using N_2 as the adsorbent, a 40-point measurement was taken, involving 20 points of adsorption and 20 points of desorption. The relative pressures of N_2 (P/P_0) ranged from 0.05 to 0.3.

If the supporting material was determined to be of sufficient specific surface area, the PZC could be determined.

A 1 M aqueous solution of HCl (pH=0) was sequentially diluted ten-fold to form solutions of pH 1, 2, 3, 4, 5, and 6. Likewise, a 1 M aqueous solution of NaOH (pH=14) was sequentially diluted ten-fold to form solutions of pH 13, 12, 11, 10, 9, and 8. For a pH of 7, deionised water was used. The volume of each solution was 3.6 mL. Not all

of these pH-adjusted solutions were used in all PZC experiments, for example, if the quantity of supporting material was limited.

The pH probe was calibrated using three buffer solutions of pH 4.01, 7.01, and 10.06. During usage, the probe was checked against these buffer solutions every 30 minutes. Following calibration, the initial pH of each solution was measured with the pH probe to ensure the actual initial pH matched the expected pH value.

For each solution, the appropriate quantity of supporting material was weighed out such that the surface loading was at least 5,000 m^2 L^{-1}. The supporting material was added to the solutions. The resulting slurries were stirred vigorously for 30 minutes. The final pH values of each solution were measured with the pH probe and plotted against their corresponding initial values. The plateau value of the final pH graph was taken as the PZC. If the PZC was above 8.00, the material was considered a high-PZC support. Below 6.00, a low-PZC support. If the PZC was in between 6.00 and 8.00, it was considered a mid-PZC support.

2.1.2 Determining the Optimal pH of Metal Uptake onto the Support

Uptake surveys were performed to determine the pH that corresponded to the highest metal uptake. First, a 1 mM aqueous solution of the metal precursor was prepared. For an uptake survey of Pd on TiO_2 for example, a 1 mM solution of Pd tetraammine (PdTA) was prepared.

The metal precursor solution was dosed into 25 mL volumetric flasks, then into beakers for pH measurements. Each solution was pH-adjusted using aqueous NaOH and HCl solutions. Highly concentrated acid and base solutions were used for large pH adjustments with minimal change in volume, and more dilute solutions were used for finer adjustments. 5 mL was extracted from each pH-adjusted metal precursor solution.

For each solution, supporting material was added at a surface loading of 500 m^2 L^{-1}. The resulting slurries were stirred vigorously for 1 hour. The final pH of each solution was measured, and 5 mL was extracted from each solution. The final pH solutions were centrifuged at 4350 rpm for 10 minutes and filtered to remove all suspended supporting material. The concentration of metal precursor in the solution before and after exposure to the supporting material was measured using the Agilent 4100 MP-

AES. The change in concentration between each initial and final solution pair was used to determine the metal uptake at the corresponding final pH.

The final pH value that resulted in the highest change in metal concentration, and therefore the highest uptake, was determined as the pH of optimal metal uptake.

2.1.3 Determining the Reduction Temperature

TPR was utilised to determine the temperature of reduction of the support-metal precursor complex to the supported metal nanoparticle complex. First, the optimal-pH sample was synthesised. The sample was pre-treated under He at 393 K for 1 hour. For the reduction analysis, 10% H_2/Ar was used at a flow rate of 30 mL min^{-1} and an attenuation of 4. Using a ramp rate of 10 K min^{-1}, the sample was heated up to a temperature of 1173 K.

The signal change was plotted against temperature, and the peak signal changes were compared with literature values to determine the required temperature of reduction.

2.1.4 Scaled-Up Impregnation

Following on from all the information gained from the PZC, uptake survey, and TPR analysis, the procedure was scaled up. Typically, a 1 mM solution of metal precursor with a volume of 500 mL was synthesised. The solution was pH-adjusted to the initial pH that corresponded to the final pH of the optimal-uptake solution of the uptake survey. Supporting material was added at a surface loading of 500 m^2 L^{-1} and stirred vigorously for 1 hour. The slurry was centrifuged and the supernatant was decanted and pH-tested. The solid, the support-metal precursor complex, was kept and dried in an oven at 368 K for 16 hours.

The dried material was reduced under flowing hydrogen in argon in a tube furnace at a temperature approximately 50 K above the reduction temperature determined with TPR for 2 hours. The flow rate was 100 mL min^{-1} and a ramp rate of 3 K min^{-1} was used.

2.2 Chemical Vapour Impregnation

With metals such as Zn, where SEA was not feasible due to the lack of a suitable precursor that does not react with acids and bases to form precipitates, chemical vapour impregnation (CVI) was used.

The Zn precursor, $Zn(acac)_2$, and supporting material were weighed out to match the desired molar ratio of Zn to supporting material. The two solids were physically mixed in a vial for 2 minutes. Once mixed, the solids were transferred to a Schlenk tube. The tube was connected to a high-vacuum Schlenk line and lowered into an oil bath heated to 353 K. The temperature of the oil bath was then increased to 406 K, and the Schlenk tube was left in the oil bath at this temperature for 1 hour, forming a complex of $Zn(acac)_2$ and the supporting material.

This complex was then calcined in a static air furnace at 773 K (ramp = 5 K min^{-1}) for 16 hours to decompose and remove the organic component. This formed the product ZnO/TiO_2.

For the purposes of this project, 5.1 mmol and 21.2 mmol of $Zn(acac)_2$ and TiO_2 respectively were used in synthesis. This was expected to yield ZnO/TiO_2 with approximately 15 wt.% ZnO.

2.3 High Surface Area ZnO (HSA-ZnO) Synthesis

For the purpose of the synthesis of bimetallic PdZn nanoparticles as catalysts, high surface area ZnO was considered as a supporting material. In this procedure, $Zn(NO_3)_2 \cdot 6H_2O$ and $(NH_4)_2CO_3$ solutions were reacted in a 1:2 molar ratio. The mixture was vigorously stirred and held at a temperature of 333 K for 1 hour. The white precipitate, $ZnCO_3$, was filtered under vacuum and washed with 2 L deionised water. The washed $ZnCO_3$ was dried at 383 K for 16 hours. The dried sample was then finely ground into a powder using a pestle and mortar. Finally, the pulverised sample was calcined in flowing air for 4 hours at 573 K. This formed HSA-ZnO, which could theoretically have a surface area of up to 102 $m^2\ g^{-1}$.

This method was devised by fellow student Isla Gow, and was a modification of the Farag method.[226]

2.4 Catalytic Testing

Once the materials had been synthesised (but not reduced), either through SEA, CVI, or a combination of the two methods, the materials were tested for their catalytic activity for the CO_2 hydrogenation reaction. Each unreduced catalyst sample was pelleted to a diameter of 425 microns using a 10 tonne press and a 600-micron sieve over a 425-micron sieve. For each sample, 500 mg of pelleted catalyst was used.

Each test was carried out using the high throughput reactor (HTR), located at the Cardiff Catalysis Institute (CCI) at the University of Cardiff. The prepared catalysts were reduced in-situ using 10% H_2/Ar at 400 °C for 1 hour. For the CO_2 hydrogenation reaction, a gas feedstock of CO_2 and H_2 in a 1:3 molar ratio was flowed over the catalysts. Reactions were carried out at temperatures of 230, 250, and 270 °C (503, 523, and 543 K), at a constant pressure of 20 bar and a flow rate of 30 mL min^{-1}.

2.5 Characterisation Methods

Throughout the project, samples were characterised using several different methods in order to obtain information on structure, surface area, elemental composition, reduction temperatures, oxidation states, and more, about products, unexpected by-products, and intermediates.

2.5.1 X-ray Diffraction (XRD)

Powder X-ray Diffraction (PXRD, or simply XRD) was used to determine the identity of all samples, and to check for any impurity phases.

In an X-ray tube, electrons are accelerated towards a target (typically Cu or Mo), ejecting a core electron upon collision. An electron in a higher-energy orbital may fill the hole left following ejection, emitting an X-ray photon. The most common X-ray type used in XRD experiments is Cu Kα (2p-1s electron transitions in Cu). This provides a beam of X-rays where the wavelength is on the same size order of magnitude as interatomic distances in crystalline solids. The X-ray tube moves such that the X-rays are emitted at a range of angles relative to the sample being analysed, interacting with the lattice planes of the substrate. Incident X-rays may be scattered upon interaction with an atom or ion's electrons and be elastically reflected. In the case of elastic reflection, the angle of reflectance equals the angle of incidence. The reflected beams enter a detector.

Each lattice plane has an angle in which X-rays are detected, determined by the Bragg equation (Equation 6).

$$2d \sin\theta = n\lambda$$

Equation 6 – The Bragg equation. d refers to the spacing between lattice planes, θ is the angle of incidence, n is a multiplier, and λ is the wavelength of the incident X-ray beam.

This results in a diffraction pattern that is measured in XRD experiments. All samples prepared in this project were powders. Powders are arranged in a large number of orientations, resulting in diffraction intensity being a direct function of diffraction angle (2θ). Since all crystalline systems have slightly different lattice parameters, PXRD can provide a “fingerprint” pattern for most crystalline samples.[227]

For all samples in this project, powdered samples (~100 mg) were mounted into a steel holder for automated sample investigation, via a mounting apparatus that prepares the sample and exposes a flat surface for the X-ray target. Steps of 0.01° were used. Cu Kα was used as the X-ray source, emitting photons of wavelength 1.5406 Å. A single-crystal Si wafer was used as the reference point. For all samples, a 0.6 mm divergence slit was used. All patterns were collected at 2θ range 5-80°, although when discussing results, smaller 2θ ranges may be presented in the absence of reflections at high or low 2θ values. A step angle of 0.02° and step time of 0.1 seconds was applied.

The width of reflection peaks within a pattern can be used to gain information on particle sizes of nanoparticles. This can be determined using the Scherrer equation (Equation 7).

$$\tau = \frac{K\lambda}{\beta \cos\theta}$$

Equation 7 – The Scherrer equation, used to determine particle size in nanoparticles. τ defers to the particle size; K is a dimensionless shape factor; λ is the X-ray wavelength, β is the broadening of the reflection peak, measured at full-width half-maximum (FWHM), subtracting instrumental line broadening (Si standard), measured as 2θ angle; and θ refers to the incident (Bragg) angle of the reflection.

This equation shows that broader reflection peaks represent a smaller nanoparticle size.[228]

2.5.2 Brunauer-Emmett-Teller (BET) Surface Area Analysis

For the scope of this project, surface area analysis marked the foundation of most experimental procedures. Surface area values were required for PZC experiments, uptake surveys, and impregnation procedures, which were fundamental to the experimental research undertaken. Specific surface areas ($m^2\ g^{-1}$) were measured for all supporting materials and potential supporting materials in which SEA could be carried out. Surface area analysis was also used to determine the viability of certain supports for application in SEA.

BET theory was used to obtain these measurements. BET theory can measure both surface area and pore size.[229] But for the scope of this project, BET was used for surface area analysis only.

BET experiments use an adsorbent gas, typically N_2, that adsorb onto the surface of the analyte. This is carried out at the boiling point of nitrogen, 77 K. The N_2 gas adsorbs onto the analyte surface in a monolayer at this temperature. The volume of adsorbed N_2 correlates to the surface area of the analyte particles, allowing for the surface area to be calculated since the size of the N_2 molecule is known.

The IUPAC defines six known isotherm types of adsorption and desorption, shown in Fig. 2.1.[230]

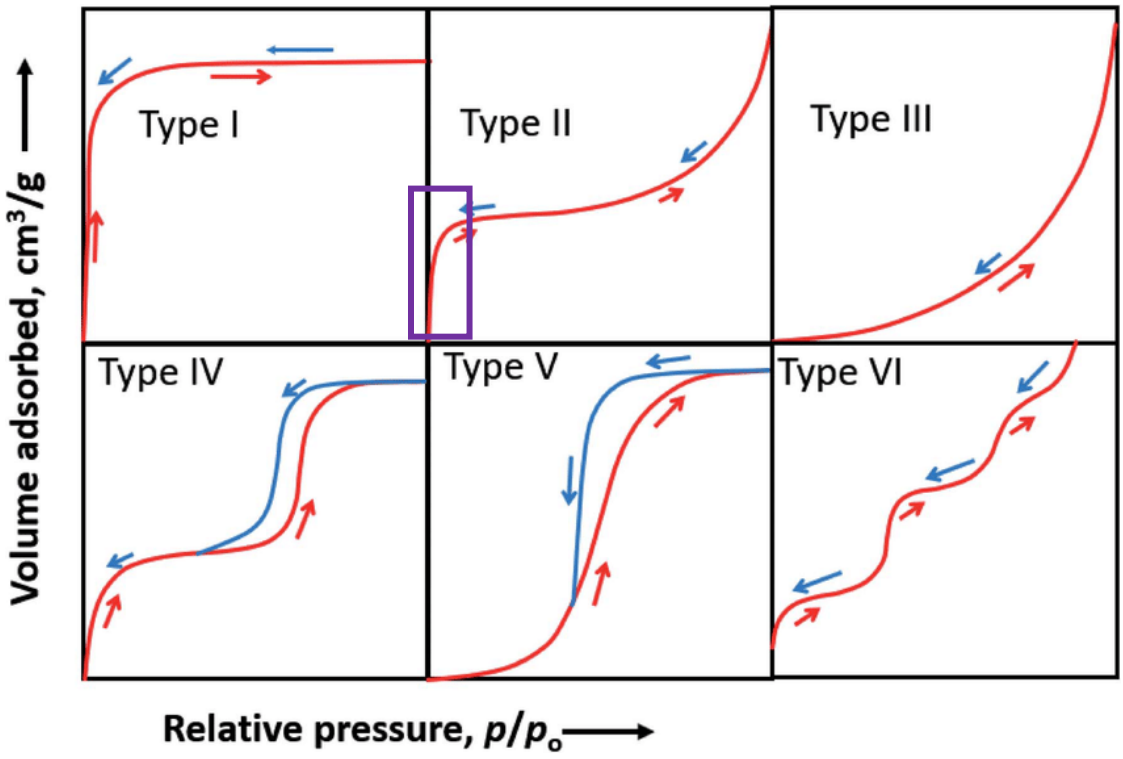

Fig. 2.1 – The six IUPAC-defined isotherms of adsorption and desorption. The region of interest for the scope of this project has been marked within the type II isotherm. Modified from [230].

BET theory applies only to type II (disperse, nonporous or macroporous solids), and type IV (mesoporous solids) isotherms. For the purpose of this project, the type II isotherm is of interest, specifically the region highlighted with the purple box. This is the region of p/p_0 values which results in a linear correlation with volume adsorbed. The BET equation (Equation 8) is then used to calculate the surface area.

$$\frac{p}{n_a(p_0 - p)} S_{total} = \frac{1}{n_m C} + \frac{(C-1)}{n_m C} \cdot \frac{p}{p_0}$$

Equation 8 – The BET equation used to calculate surface area. p=pressure; p_0=saturation pressure; n_a=gas adsorbed; n_m=monolayer capacity, 1/(gradient-intercept); C=BET constant, 1+(gradient/intercept); S_{total} = surface area.

To obtain the specific surface area, the calculated surface area is divided by the sample mass. The BET constant, C, is a measure of the adsorbent-adsorbate interaction. C should be between 50 and 200. If this value is lower than 20, the BET method is invalid. Greater than 200 suggests significant porosity.

Samples were weighed out in a vessel consisting of a long tube 9 mm in diameter with a bulb at the bottom. To gain accurate measurements, samples were first degassed. This was to remove any organic residues or moisture which could affect both the measured surface area reading and the measured mass of the sample. Degassing was carried out under near-vacuum and at temperatures of 453 K for 3 hours. Following degassing, the sample tube was weighed, and the mass of sample was taken as the difference between the degassed sample and the empty vessel. Typically, approximately 150 mg of sample was used for analysis.

Surface area measurements were taken using the Nova 600 BET instrument, with N_2 as the adsorbent gas, and at temperatures of 77 K achieved through the sample bulb being lowered into a Dewar of liquid nitrogen during recording. 40-point readings were taken for each analyte, with 20 adsorption and 20 desorption points. This was to minimise instrumental error, allowing for more accurate surface area measurements that were required given the importance of these readings for further experiments. Note that experimental errors could still potentially arise, such as weighing errors due to small quantities of powder sticking to the top of the BET tube.

2.5.3 Microwave Plasma Atomic Emission Spectroscopy (MP-AES) Elemental Analysis

Microwave Plasma Atomic Emission Spectroscopy (MP-AES) is a technique for analysing concentrations of elements in solution. In uptake surveys, this technique was crucial in obtaining the change in metal concentration before and after supporting materials were added, thus allowing the value of metal uptake to be calculated. For instance, concentrations of Pd were measured using MP-AES before and after TiO_2

was added, and the difference between the two values was used to determine Pd uptake on TiO_2. Prior to testing, all solid was removed via centrifuging and syringe filtration. In cases where metal concentration was expected to be greater than 100 ppm, solutions were diluted two-fold with deionised water.

This technique utilises microwaves in a nitrogen atmosphere to produce a nitrogen plasma discharge. During testing, the solutions are nebulised and passed through the plasma, promoting electrons in the sample to an excited state. Upon returning to their ground state, the electrons release a photon in the UV or visible range. This produces an emission spectrum that is unique to each element. A detector measures the intensity of emissions of specific wavelengths to determine the quantity of the element within the sample. MP-AES can detect elements with weight-fractions low as parts per billion within the sample.[231]

For each element tested, be it Pd, Na, Pt, or Au, calibration solutions were prepared and used to calibrate the MP-AES machine. These typically involved three or four-point calibrations and were prepared via dilutions of a 1000 wtppm solution. For instance, Pd calibration solutions consisted of 100, 50, 10, and 1 ppm Pd. Check solutions of concentrations not equal to calibration solutions, such as 25 ppm Pd, were used to test the accuracy of the calibration.

Pd was detected using wavelengths of 340.458 and 360.955 nm. With each sample, three measurements were taken at each of these wavelengths. Readings for deionised water were taken after each sample to check the calibration remained adequate (each reading for deionised water should display close to 0.00 ppm), and to rinse the tubes of any residual metal.

2.5.4 Temperature Programmed Reduction (TPR)

In scaled-up impregnations, TPR was used to determine the temperature at which reduction and decomposition from the metal precursor to the metal nanoparticle occurred under flowing H_2 gas. This yielded information on what temperature to carry out the reduction stage at. For these experiments, the Quantachrome Instruments ChemBET Pulsar TPR/TPD was used.

This process involved raising the temperature at a constant rate (10 K min^{-1}) from room temperature to 1173 K, while flowing H_2/Ar over unreduced samples. A thermal conductivity detector (TCD) measured any changes of the thermal conductivity of the

gas stream, thus indicating reduction was occurring. For instance, a metal precursor such as PdTA reducing to the metal nanoparticle would consist first of thermal decomposition via liberation of ammonia, followed by formation of hydrogen and nitrogen chlorides carried off in the gas stream, reducing Pd^{2+} to Pd^{0}.[232] These changes in gas composition cause a change in the thermal conductivity of the gas stream which directly correlate to the rate of evolution of these gases, which in turn correlates to the rate that reduction is occurring, which the TCD measures. Any peaks observed in a TPR profile correspond to the temperature at which the maximum rate of reduction occurs.[233]

In order to obtain fine measurements, the TCD sensitivity was increased before heating started. Adjustments were carried out, with the attenuation being lowered step-wise in halves. TPR procedures for this project were carried out with an attenuation of 4. Approximately 50 mg of sample was used for TPR analysis.

2.5.5 X-ray Photoemission Spectroscopy (XPS)

Experimentally, XPS was used to obtain both quantitative and qualitative information. Specifically, elements present, quantitative elemental analysis, and metal oxidation states.

In XPS, X-ray photons are generated through a process similar to XRD. A beam of X-rays are fired onto the sample. Electrons within atoms at or within a few nm of the surface of the sample absorb the high-energy photons, and are eventually ejected from the sample with a certain kinetic energy and into a detector. The ejection of electrons following exposure to high-energy photons is known as the photoelectric effect. For a given element, the work function, ϕ, is defined as the minimum energy required to eject electrons. The energies of the ejected electrons are plotted against the relative number of electrons produced. Atoms in the sample are analysed according to the XPS equation (Equation 9):

$$\mathbf{E_{binding} = E_{photon} - (E_{kinetic} + \phi)}$$

Equation 9 – The XPS equation. $E_{binding}$ is the binding energy of the electron to the atomic nucleus; E_{photon} is the energy of the X-ray photon; $E_{kinetic}$ is the kinetic energy of the ejected electron; ϕ is the work function of the atom.

In this equation, since E_{photon} is known, and $E_{kinetic}$ and ϕ are measured by the detector, $E_{binding}$ is the only unknown, which the equation can determine. Since each element

has different binding energies (BE) with its electrons, qualitative and quantitative elemental analysis can be determined when electron counts are plotted against BE. Each element will have multiple peaks, since electron shells and subshells all exhibit different BE values for a given element (further orbitals from the nucleus have lower BEs).

BE doesn't only depend on the nucleus the electron is orbiting. The greater chemical environment can also have an impact, such as any bonding to the atom. For example, an O atom in an organic molecule will have a slightly different 1s BE to an O atom in a metal oxide. In multimetallic compounds, alloying between two metals, or the formation of core@shell particles, also provide a different chemical environment to a monometallic sample.

The oxidation state of a metal can also have an impact on the BE value for a specific atomic subshell. Electrons in an oxidised metal, such as Pd(II), will have a greater BE than a neutral Pd atom, due to the positive charge present in a cation having a greater effect on the electrons. As such, XPS can also be used to determine oxidation states of metals.[234]

For these experiments, XPS was performed on a Thermo Fisher Scientific K-α+ spectrometer. Samples were mounted by pressing in to recesses in a Cu based top plate for the sample holder and analysed using a micro-focused monochromatic Al x-ray source of power 72 W. The analysis area was defined by an ellipse of approximately 600x400 microns. Data was recorded at pass energies of 150 eV for survey data and 40 eV for high resolution data with 1 eV and 0.1 eV step sizes respectively. Charge neutralisation of the sample was achieved using a combination of both low energy electrons and argon ions. Data analysis was performed in CasaXPS using a Shirley type background and Scofield cross sections, with an energy dependence of -0.6.

2.5.6 Electron Microscopy Imaging and Elemental Mapping

Catalyst samples were imaged using a JSM-6610 Scanning Electron Microscope. Imaging the samples enabled structural information on the micron-scale to be gained and EDX measurements to be taken.

Scanning Electron Microscopy (SEM) involves a focused electron beam directed towards the sample under vacuum. The electrons hit the surface of the sample and

eject an electron in the valence orbitals. The ejected electron is referred to as a secondary electron. The secondary electrons are directed towards a detector, forming an image of the topography of the sample.[235]

Energy Dispersive X-ray (EDX) Spectroscopy was utilised for elemental mapping. In a typical set-up, a beam of high-energy electrons hits an atom within the sample. A core electron is ejected from the atom, and an electron in a higher-energy orbital fills the hole. The movement of the higher-energy electron releases an X-ray photon equal in energy to the difference between the higher and lower-energy shell. Each element emits X-ray photons of a "fingerprint" energy. The detector can measure the location and number of emissions, yielding structural and compositional information.[236]

In this project, elemental mapping was used for qualitative analysis of the distribution of Pd and Zn throughout BMNP samples in order to determine the structure of these catalysts, and to determine a mode of growth of ZnO when applied to the supporting material via CVI. EDX data also provides quantitative elemental analysis, but this was used only to compliment other elemental analysis methods in this project such as XPS and MP-AES.

TEM images were also taken using a JEOL JEM 2100 electron microscope. The sample was placed on a carbon-coated 300-mesh Cu grid. An acceleration voltage of 200 kV was used. Images were taken at varying magnifications and the focus was continuously adjusted to ensure high-quality images.

2.5.7 Infrared and Raman Spectroscopy

Infrared Spectroscopy (IR) was carried out to test for supporting material "cleanliness", to ensure the support was devoid of organic contamination prior to uptake surveys. All samples were tested using a Nicolet iS5 FTIR Spectrometer. The samples were placed on a diamond ATR crystal.

The wavenumber range was set to 400-4000 cm^{-1} (resolution 1 cm^{-1}) and absorbance of each sample was measured. To obtain a high signal-to-noise ratio, 64 scans were taken for each sample. To minimise background noise in sample measurements, a background spectrum of air was taken before each sample. 64 scans were taken for each background spectrum.

Raman spectroscopy was used to obtain information on speciation of a sample at low pH values. A Si standard was used as the reference point.

Both techniques gain information on the structure of molecules through determination of vibrational modes. When a molecule absorbs an infrared photon, the energy from the photon can cause a bond within a molecule to increase its vibrational energy state, which is quantised. This is caused by interactions between the electric field of the radiation, and the bonds within molecule itself.

For Raman spectroscopy, Rayleigh (elastic) scattering is filtered out. Instead, the inelastic scattering modes, shown in Fig. 2.2, are measured. This includes the Stokes and anti-Stokes scattering.

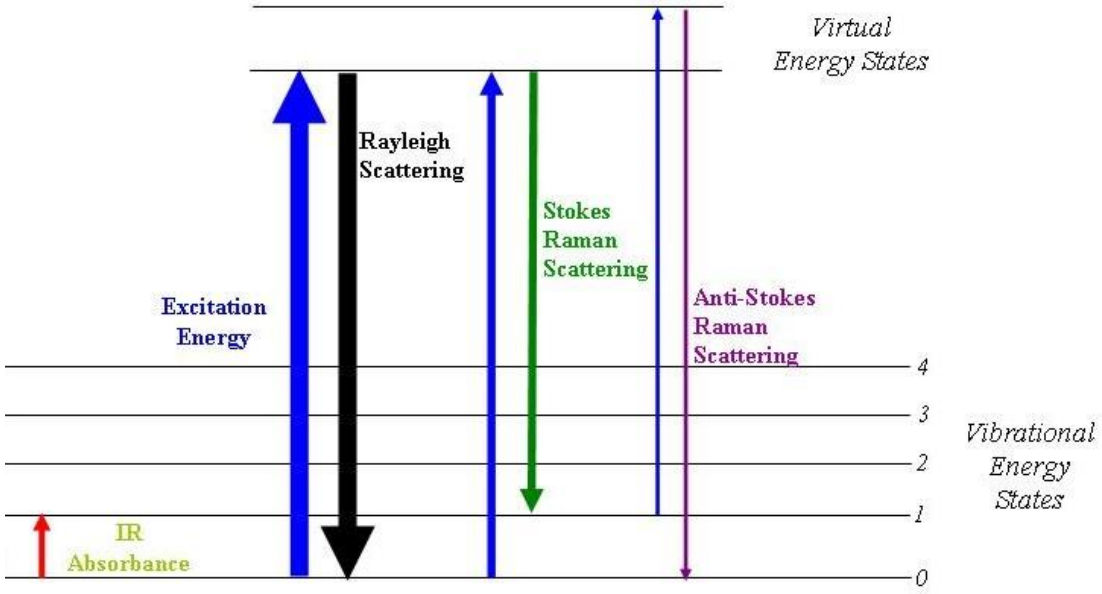

Fig. 2.2 – Modes of IR photon scattering with regards to the vibrational energy states within a molecule. This displays the increase in vibrational energy state of a simple IR absorption, the elastic Rayleigh scattering promotion to virtual energy states, and the inelastic Stokes and anti-Stokes scattering measured in Raman spectroscopy. Reproduced from [237].

In general, IR spectroscopy is useful for measuring vibrational modes within organic functional groups, such as C-C, C=C, C≡C, C-O, C=O, C-H, C-X (X=halogen), and more. Each of these modes have well-documented wavenumber values, allowing for identification of molecules. Raman spectroscopy is useful in measuring vibrations with inorganic molecules, such as metal-ligand complexes. In both techniques, group theory can be used to determine the number of expected vibrational modes. In addition, using IR and Raman spectroscopy, group theory can be applied to determine structural isomers of complexes.[238]

3 Results and Discussion

Following the theory and information gathered throughout this research project, the SEA method was put into practice in order to synthesise multimetallic MNP catalysts for the hydrogenation reaction of CO_2 to methanol. Throughout this chapter, experimental data will be presented and discussed. This includes data gathered on supporting materials, PZC experiments, uptake surveys, characterisation of catalytic materials formed, and catalytic testing for the CO_2 hydrogenation reaction. MMNP and BMNP catalysts were synthesised and tested. Finally, the SEA method will be critically evaluated for its feasibility in synthesis of multimetallic MNP catalysts for this reaction.

3.1 Experimental Supporting Material Analysis

In order to build up to multimetallic systems, it was important to first build an understanding of the supporting materials. Throughout this project, several supporting materials were initially considered to serve as the foundation for the multimetallic systems. These were TiO_2 (P25), SiO_2 gel, γ-Al_2O_3, and commercial ZnO.

3.1.1 Surface Area Analysis

For each of the four supporting material candidates, the specific surface areas were determined using BET analysis (Table 3). The SiO_2 gel and γ-Al_2O_3 samples were tested both calcined at 773 K and uncalcined, to assess any potential loss in surface area once the supporting material had been calcined or heat treated.

The results of this analysis showed commercial ZnO, with a specific surface area of 6 $m^2\ g^{-1}$, would be unsuitable for this application. This is because, in order to obtain a sufficient surface loading required for further experiments to determine the PZC of the supporting material, and the eventual uptake surveys and impregnation procedures, would require a larger-than-practical quantity of supporting material. For instance, in an experiment to determine the PZC, which would require surface loadings of at least 5,000 $m^2\ L^{-1}$, more than eight grams of ZnO would be required per 10 mL of water to obtain such a surface loading.

Table 3 – Specific surface areas obtained for four supporting materials using BET analysis. Silica and alumina have both their calcined (773 K) and uncalcined surface areas taken. TiO_2 (P25) and commercial ZnO were only considered post-calcination. The BET constant shows the validity of the method: if the constant were lower than 20, the affinity of the adsorbent with the adsorbate would be considered too low for the method to be deemed valid.[229]

Supporting Material	Specific Surface Area / m^2 g^{-1}	BET constant
TiO_2 (P25), calcined	56	77.415
TiO_2, anatase only	47	80.412
SiO_2 gel, uncalcined	495	81.367
SiO_2 gel, calcined	371	92.442
γ-Al_2O_3, uncalcined	128	126.456
γ-Al_2O_3, calcined	132	93.494
Commercial ZnO, calcined	6	146.606

In order to improve the practicality of further experiments with the supporting material, a minimum specific surface area was decided to be 40 m^2 g^{-1}. This would correspond to 1.25 grams of supporting material per 10 mL of water to obtain the desired minimum surface loading for PZC experiments. As such, the remaining three supporting materials were considered for further experimentation.

3.1.2 Point of Zero Charge Analysis

For four supporting materials: TiO_2 P25, TiO_2 anatase only, SiO_2 gel, and γ-Al_2O_3, the point of zero charge (PZC) was determined. For the purposes of this experiment, surface loadings of greater than 10,000 m^2 L^{-1} were used, ensuring a wide range of

initial pH values that would result in a final pH that is equal to the PZC. At these surface loadings, the PZC “plateau” occurs when the initial pH is between approximately 4 and 10. Fig. 3.1 displays the initial pH-final pH graphs obtained from this analysis.

For each of these supporting materials, a clear plateau at the PZC was observed, with only the initial pH values at the extreme acidic and extreme basic values resulting in a final pH value that differed from the PZC.

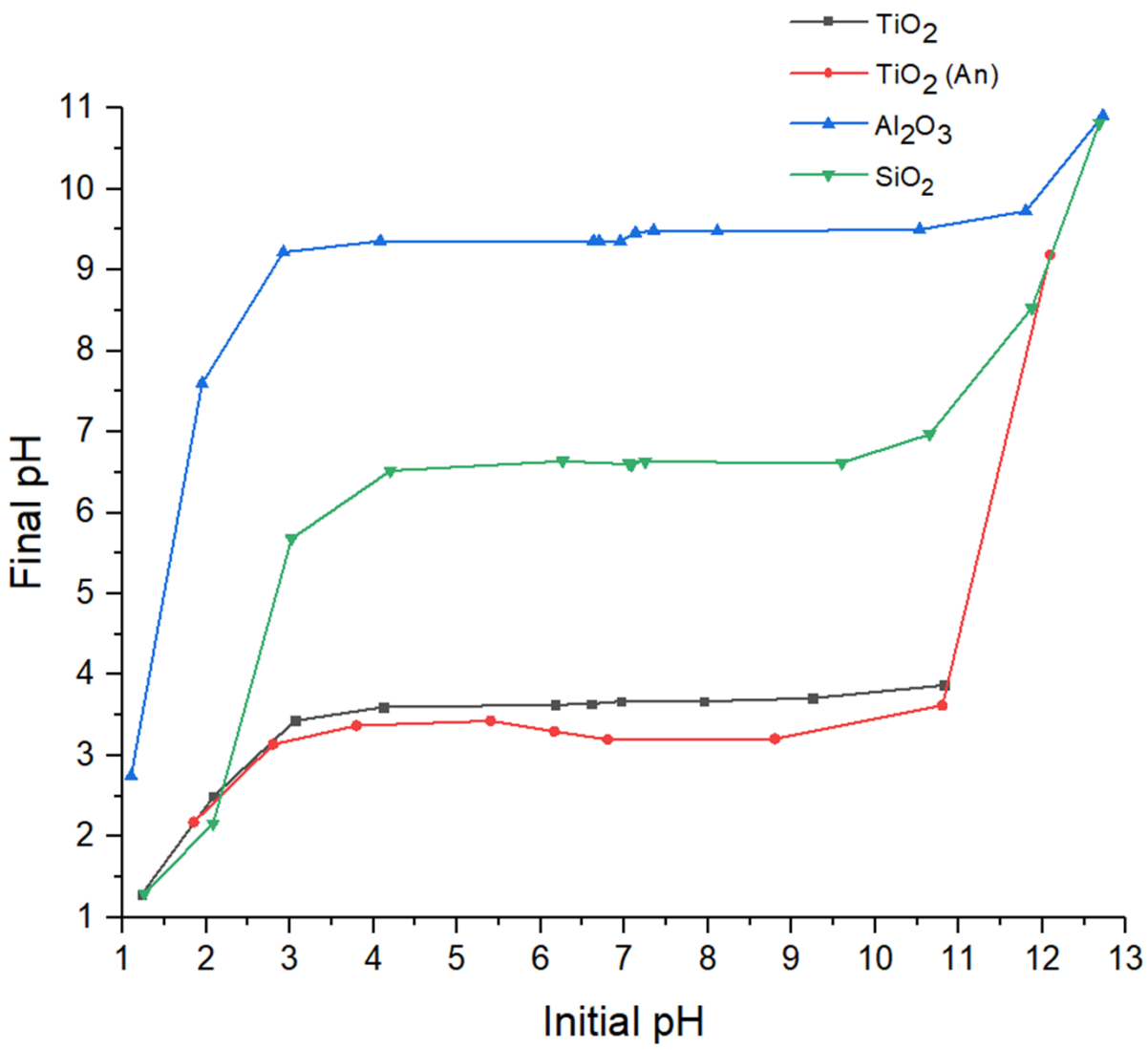

Fig. 3.1 – PZC graphs of four supporting materials: a) TiO_2 P25; b) TiO_2 (anatase only); c) γ-Al_2O_3; d) SiO_2 gel.

The data displayed in Fig. 3.1a shows that the PZC of TiO_2 P25 can be taken as 3.6. As such, this supporting material is considered low-PZC. Note that for P25 TiO_2, the

slurries solidified at initial pH values greater than 11, making measurements at higher initial pH values impossible to obtain.

For anatase-only TiO_2 (Fig. 3.1b), a clear plateau was observed between initial pH 4 and 11. This data shows the PZC of anatase-only TiO_2, hereafter known as ana-TiO_2, can be taken as 3.3. As such, this supporting material is considered low-PZC. For SiO_2 gel (Fig. 3.1c), a clear plateau was observed between initial pH 4 and 10. This data shows the PZC of SiO_2 gel can be taken as 6.6. As such, this supporting material is considered mid-PZC. For γ-Al_2O_3 (Fig. 3.1d), a clear plateau was observed between initial pH 3 and 10.5. The data shows that the PZC of γ-Al_2O_3 can be taken as 9.4. As such, this supporting material is considered high-PZC.

Table 4 summarises the information obtained from this PZC analysis.

Table 4 – Summary of the PZC analysis of four supporting materials: TiO_2 P25; Anatase only TiO_2; SiO_2 gel; and γ-Al_2O_3. The type of metal complex this support would take at pH value opposite to the PZC has been included.

Supporting Material	PZC	Low/Mid/High-PZC Support	Type of Metal Complex
TiO_2 (P25)	3.6	Low	Cationic
Ana-TiO_2	3.3	Low	Cationic
SiO_2 gel	6.6	Mid	Cationic
γ-Al_2O_3	9.4	High	Anionic

3.1.3 The Effects of Calcination

Supporting material oxides, especially old samples, attract moisture, CO_2, ions such as Na^+, and VOCs from the environment that will adsorb onto the surface, and therefore may make the surface “unclean”. This could potentially hamper its ability to uptake metals from solution. As such, pre-calcination of the supporting materials may be a necessary step to increase the metal uptake.[239]

The three supporting materials previously discussed were pre-treated with flowing air, flow rate of 30 mL min^{-1}, at 773 K (ramp rate of 10 K min^{-1}) for 3 hours, followed by natural cooling.

Fig. 3.2 shows the XRD obtained for each of these supports, before and after they were calcined. Fig. 3.2a shows the TiO_2 pattern did not change following calcination. Fig. 3.2b shows there was a slight reduction in the intensity of the SiO_2 diagnostic reflection. However, Fig. 3.2c shows γ-Al_2O_3 also shows reflections lowering in intensity. Notably, the reflection at 33° becoming a shoulder rather than a sharp peak.

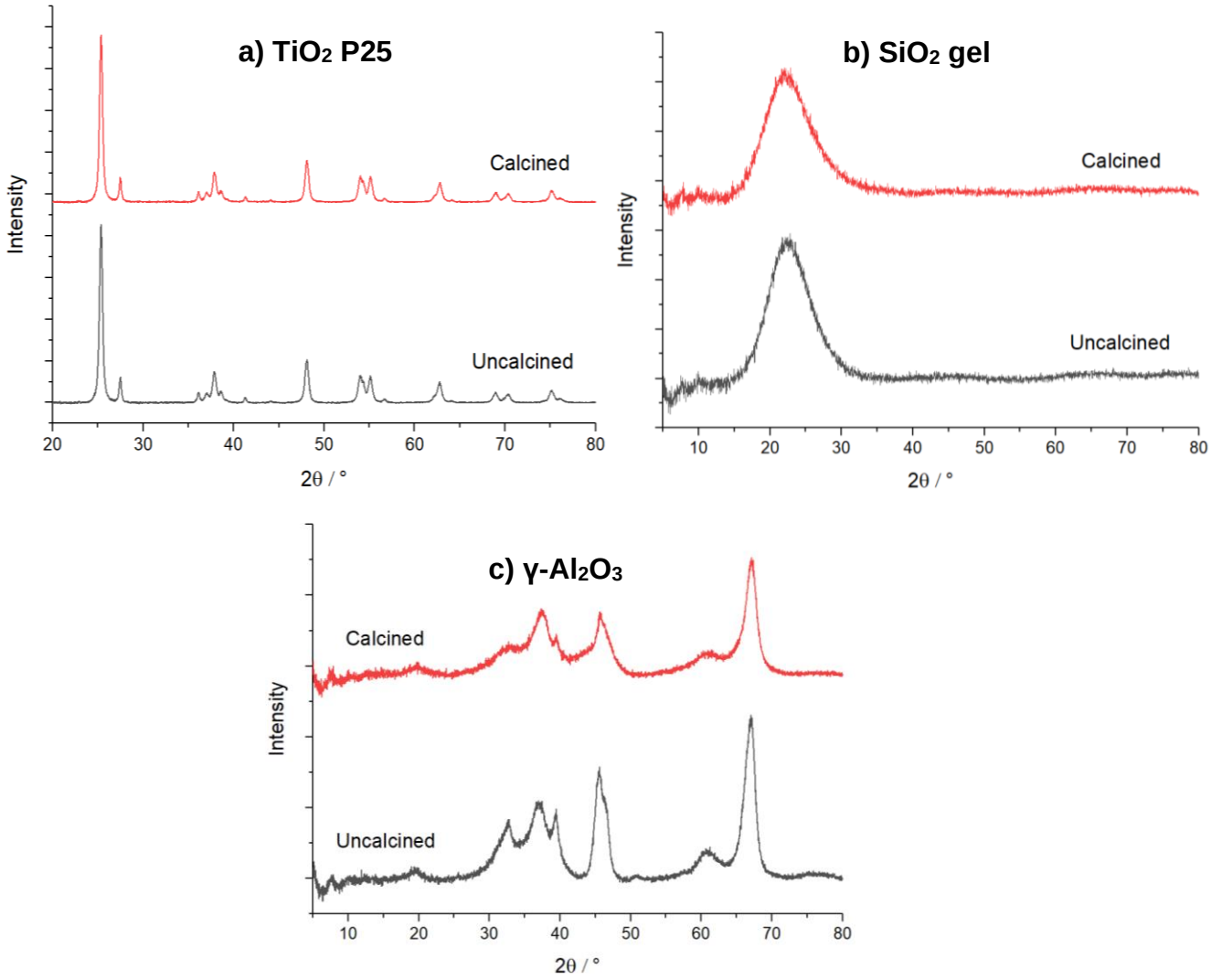

Fig. 3.2 – XRD patterns of a) TiO_2 P25; b) SiO_2 gel; c) γ-Al_2O_3, before and after calcination.

As previously discussed, changes to the surface area were observed before and after calcination (refer to Table 3). SiO_2 underwent a significant reduction in surface area

from 495 to 371 m^2 g^{-1}. Since the broad peak at 24° does not narrow after calcination, this shows no agglomeration of particles is occurring. However, the intensity of this peak is reduced. As such, this could suggest the calcination results in a loss of crystallinity, which could remodel the surface.

γ-Al_2O_3 underwent a slight increase in surface area from 128 to 132 m^2 g^{-1}, however this change is small enough it could be down to experimental error, which may arise through sample loading issues such as sample sticking to the side of the tube, and potential weighing errors. However, the changes to the XRD pattern would also suggest a loss crystallinity following calcination.

FT-IR spectra were taken before and after calcination. Fig. 3.3 displays these spectra.

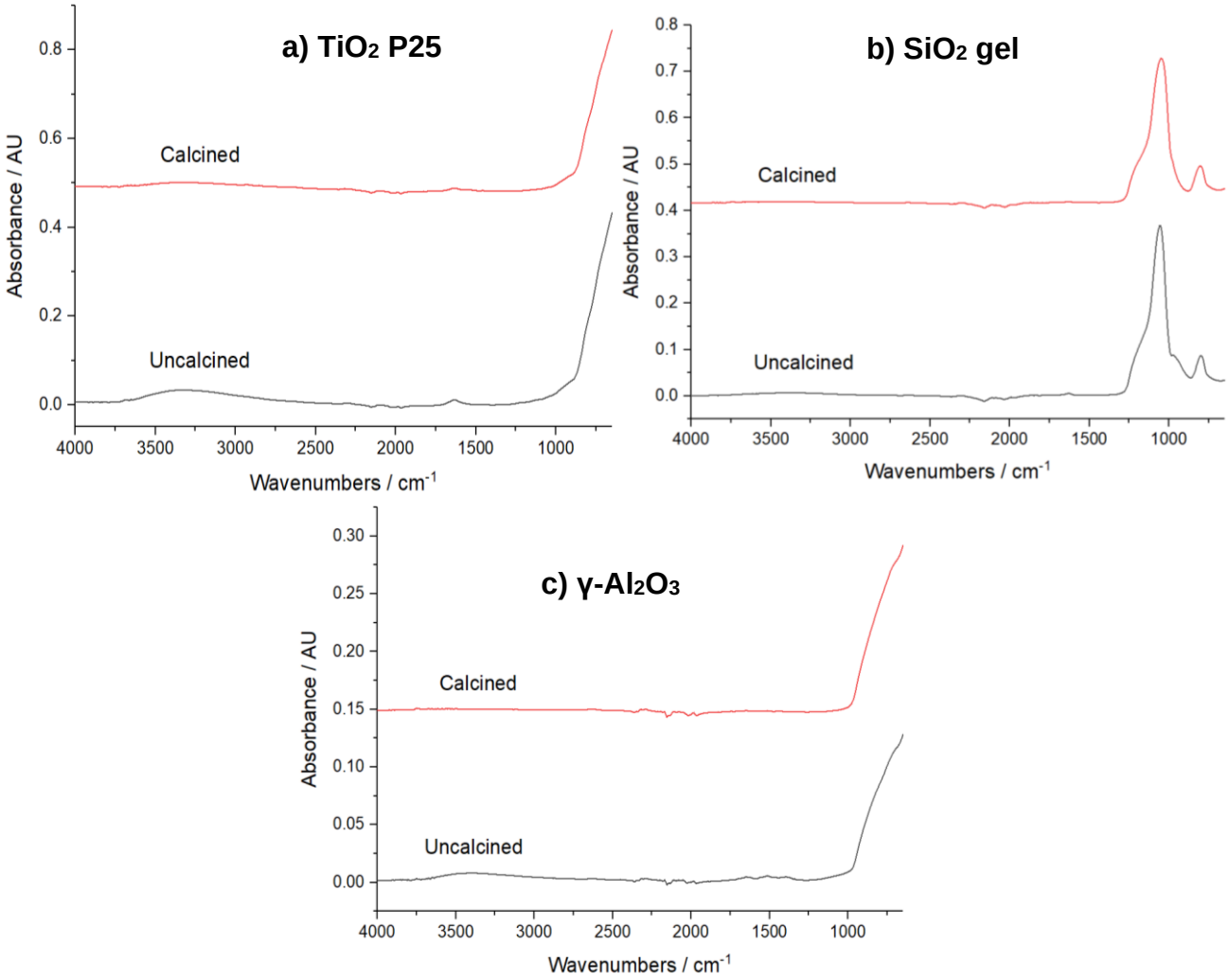

Fig. 3.3 – FT-IR spectra of a) TiO_2 P25; b) SiO_2 gel; c) γ-Al_2O_3, before and after calcination. Absorbance is measured as the absorbance of infrared radiation by the sample.

The spectra for all 3 supporting materials show a loss of the broad hump at 3000-3800 cm^{-1} following calcination. This corresponds to stretching vibrations of an O-H bond,

showing the presence of water on the surface of an uncalcined supporting material that is almost entirely removed upon calcination. Owing to the hygroscopic nature of TiO_2, however, some water is retained, as seen in Fig. 3.3a.

All three spectra show losses of very small peaks and features that occur in the 1500-2500 cm^{-1} range, which is indicative of a very low quantity of organic contaminants on the surface of uncalcined supporting materials.

This data shows that calcination can serve to remove water and low quantities of other contaminants from the surface. However, losses in crystallinity or surface area may occur.

3.2 Monometallic Palladium Nanoparticles

With information gained on the nature of the surface of the supporting materials, such as surface area, PZC, and the effect of calcination, the SEA method can be applied to add metals onto the surface. For the purposes of this section, TiO_2 P25 was used as the supporting material, and Pd was the metal that was added to the supporting material via SEA.

3.2.1 Palladium Precursor Speciation

The Pd precursor used was $[Pd(NH_3)_4]Cl_2$, referred to hereafter as Pd tetraammine, or PdTA. This is a brown water-soluble salt that features a complex with a Pd(II) centre and four NH_3 ligands with square planar geometry.

Since the metal uptake survey requires exposure of this salt to aqueous HCl up to a concentration of 0.1 M (pH=1), and aqueous NaOH up to a concentration of 0.1 M (pH=13), changes to the salt may occur that may impact the outcome of the uptake survey. For example, ligand exchange between the ammine ligand and Cl^- or OH^- in the pH-adjusted solutions may occur.

The most obvious change occurred when a 1 mM aqueous solution of PdTA was pH-adjusted to a pH of 1 with HCl. A yellow precipitate rapidly formed. This precipitate was filtered, and the solid was analysed using Raman spectroscopy. A spectrum of the original Pd precursor salt was also taken. These spectra are displayed in Fig. 3.4.

The sharp high-intensity peak at approximately 500 cm^{-1} on Fig. 3.4a was assigned as the Pd-N stretch. A low-intensity double peak at 300 cm^{-1} and <200 cm^{-1} was assigned as a Pd-Cl stretch which could occur due to ionisation isomerisation. N-H

stretches occurring within the ammine ligands are expected to occur in the 3300-3500 cm^{-1} range, which are not displayed on this spectrum.

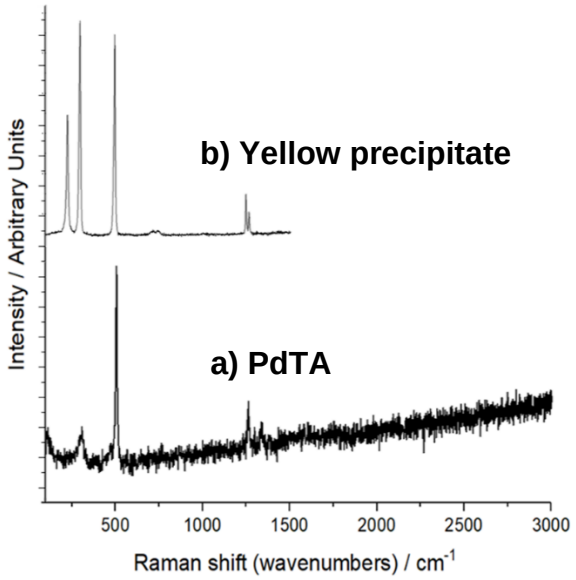

Fig. 3.4 – Raman spectra of a) PdTA and b) the yellow precipitate formed when PdTA was exposed to 0.1 M aqueous HCl.

Fig. 3.4b shows that the Pd-Cl stretch, only a minor feature on the PdTA salt spectrum, is now a major feature on the spectrum of the yellow precipitate. However, the Pd-N stretch is still a major feature on the yellow precipitate spectrum. Therefore, the precipitate contains both Pd-N and Pd-Cl interactions.

Since there are two Pd-Cl stretch peaks observed, group theory can be used to determine the symmetry and isomerisation of this complex, and therefore its stoichiometry. The trans isomer of a square planar complex is of D_{2h} symmetry, whereas the cis isomer is of C_{2v} symmetry. Group theory suggests the trans isomer would have one Raman-active Pd-Cl stretch, whereas the cis isomer would have two. Since two peaks are observed, the symmetry of this complex can be assigned as C_{2v}, which is indicative of the cis isomer. As such, this yellow precipitate was identified as cis-$[Pd(NH_3)_2Cl_2]$.

Raman spectroscopy was used to determine if any changes were occurring to the PdTA salt at higher pH. When a 1 mM aqueous PdTA solution was pH adjusted to a pH of 13 with NaOH, no colour change or precipitation was observed.

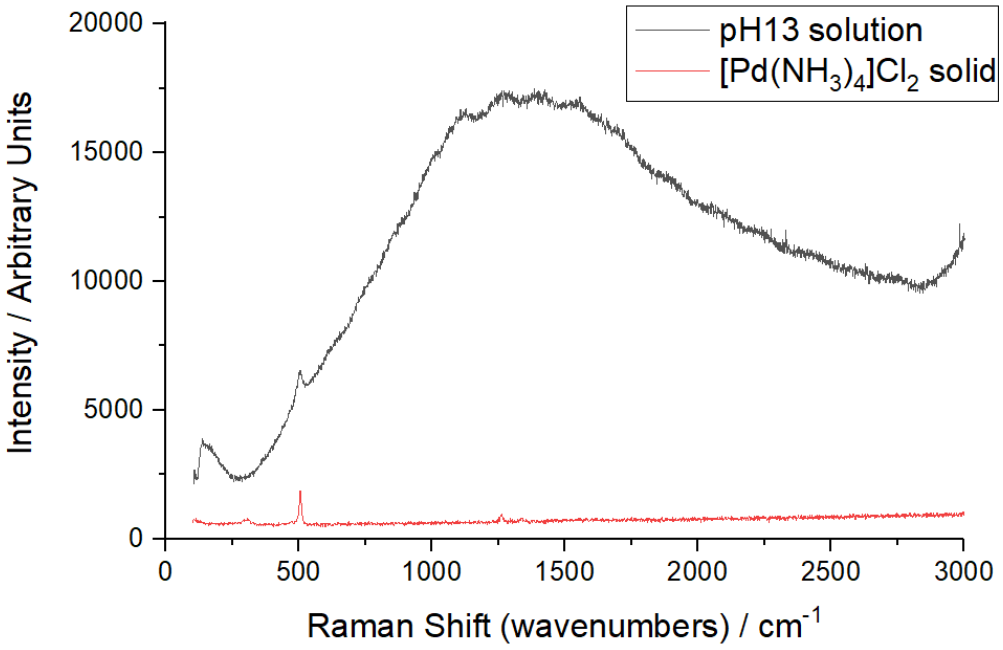

Fig. 3.5 – Raman spectra of PdTA in a pH 13 solution. This has been superimposed on the PdTA solid spectrum.

As shown by Fig. 3.5, the Pd-N peak was observed at 500 cm^{-1}, suggesting retention of the Pd-N interaction. However, since this spectrum was taken in solution, other features were difficult to observe, even on full laser power, thus could not conclusively determine any loss of Pd in solution.

Elemental analysis of the solution using MP-AES was carried out, but this showed no change in the concentration of Pd in the solution, remaining at approximately 100 ppm both at native pH and pH 13. Since each solution was filtered and centrifuged before testing, this shows no measurable precipitation occurred.

Finally, a sample of TiO_2 was exposed to 0.1 M aqueous HCl, and a separate sample was exposed to 0.1 M aqueous NaOH solutions for 1 hour each. BET surface area analysis showed no measurable loss in surface area following this treatment (56 m^2 g^{-1}).

3.2.2 Pd/TiO_2 Uptake Surveys

The pH of optimal Pd uptake on TiO_2 P25 was determined through an uptake survey. Due to the observed speciation and subsequent loss of solubility of the PdTA salt at low pH, and the fact TiO_2 is a low-PZC support which will favour high pH values for optimal uptake, the range of pH values tested was in the range of 6 to 13.

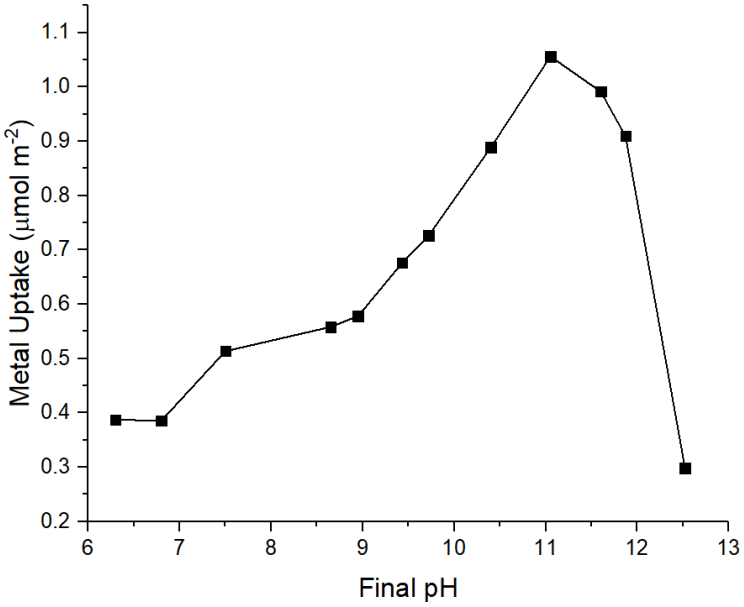

Fig. 3.6 – Metal uptake survey of Pd onto TiO_2 P25, uncalcined.

The results of the uptake survey, displayed in Fig. 3.6, show a pattern that is similar to the uptake surveys reported by John Regalbuto and co-workers.[214] The further from the PZC, the greater the uptake of Pd. A clear optimum is observed, at a final pH of approximately 11. The corresponding initial pH for this final pH was 11.8, which was pH-shifted to 11 due to the addition of TiO_2. At extremely basic pH values, as predicted, the uptake rapidly decreased due to the ionic screening effects previously discussed.

Although the shape of the curve was in line with expectations, the actual uptake value was considerably lower than expected. The maximal uptake value was approximately 1.05 µmol m^{-2}, or approximately a 0.63 Pd wt.% loading. Assuming a 1 mM solution of PdTA has a Pd wt.% of 106 ppm, and the surface loading is 500 m^2 L^{-1}, the maximum possible uptake of Pd, if all the Pd in the solution was adsorbed onto the surface of the TiO_2, would be 2 µmol m^{-2} (approximately 1.2 Pd wt.% loading). Therefore, only approximately 52% of all the available Pd was adsorbed.

A repeat of this uptake survey was carried out in which the TiO_2 was pre-calcined. This, however, did not improve the maximum Pd uptake, which was still approximately 1 µmol m^{-2}. Although in theory calcination should increase the number of available adsorption sites, the FT-IR results shown in Fig. 3.3 show that contamination by organic compounds is very low, and that removing these would have very little effect.

Since the TiO_2 is immersed in water during the procedure, the presence or absence of water on the support before the experiment would also not impact the metal uptake.

Fig. 3.7 displays the results of a third repeat of this experiment, in which calcined TiO_2 P25 was used, and the concentration of Na was analysed as well. This is because Na^+ in solution, which increases in concentration with pH, could be competing with the PdTA complex for adsorption.

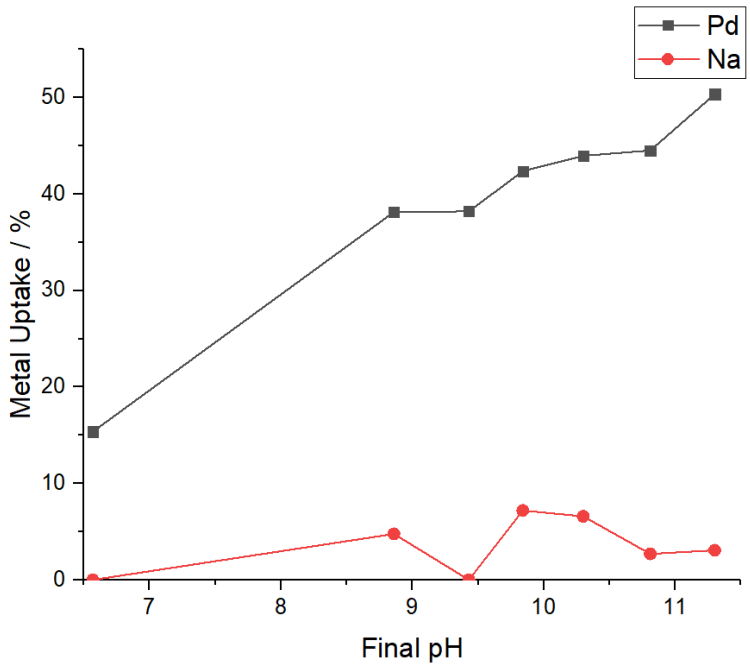

Fig. 3.7 – Metal uptake survey of Pd onto TiO_2 P25, calcined. The uptake of Na was also measured.

A clear trend of Na uptake was not observed. The highest uptake of Na, 7%, occurred at a final pH of 9.8. Even as the concentration of Na in solution increased with pH, the uptake of Na was consistently low, showing little to no competition between Pd and Na. Since there was measurable uptake of Na onto TiO_2, however, this uptake survey was repeated, but using aqueous ammonia (ammonium hydroxide, AH) as the base instead of NaOH. Using AH as the base actually reduced the uptake of Pd, with the maximal uptake being approximately 30%. The reason behind this is currently unknown, however, speciation of the metal precursor has been suggested as a potential factor.

To ensure 1 hour of contact was enough time for maximal uptake to be achieved, the optimal-pH solution was re-created, using an initial pH of 11.8 (Fig. 3.8). Samples were

periodically extracted from the solution and the concentration of Pd in solution was determined.

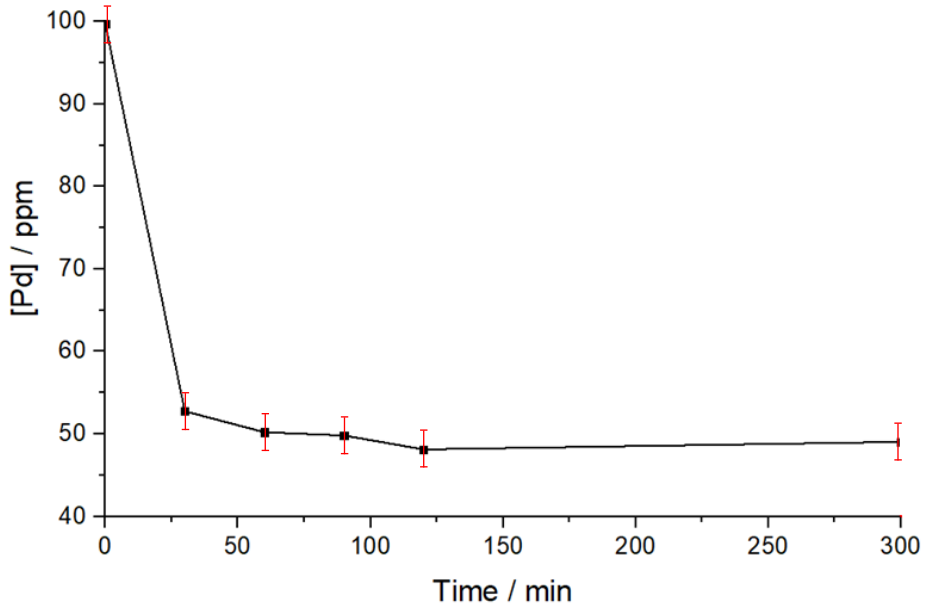

Fig. 3.8 – Pd concentration in solution after 30, 60, 90, 120, and 300 minutes of exposure to the supporting material.

This data shows that more than 95% of the Pd that will be taken up within 60 minutes will be taken up within the first 30 minutes. In fact, after the first 30 minutes, there was little change in the concentration of Pd in the solution. Even after 300 minutes, no more than 50% of the Pd had been adsorbed. This shows that the 1 hour of contact with the support was sufficient. The main source of error in this experiment was experimental TiO_2 weighing errors, which were up to ±1%. Compounded with fill errors (±0.6%), dilution errors from MP-AES calibration (±0.3%), and the resolution of the MP-AES readings (0.01 ppm), total errors were taken to be ±2%, or ±2 ppm. The error bars on the dataset reflect these errors, and show that the concentration of Pd from 30 minutes onwards were within experimental and instrumental error.

These results suggest an inherent limit to the uptake of Pd on TiO_2. This limit can be explained by the effect of hydration sheaths, which was previously discussed in chapter 1. John Regalbuto reported that the M-tetraammine complexes (M=Pd, Pt), when adsorbed onto the metal oxide surface, retain two hydration sheaths, which limits the packing density of the complex on the surface of the support.[217] It is currently not known if sequential SEA procedures would increase the metal loading.

Following information gained on the PZC of TiO_2 and the optimal pH of Pd uptake, TPR was used to determine the temperature of reduction of PdTA to Pd nanoparticles. The procedure followed is detailed in Chapter 2.

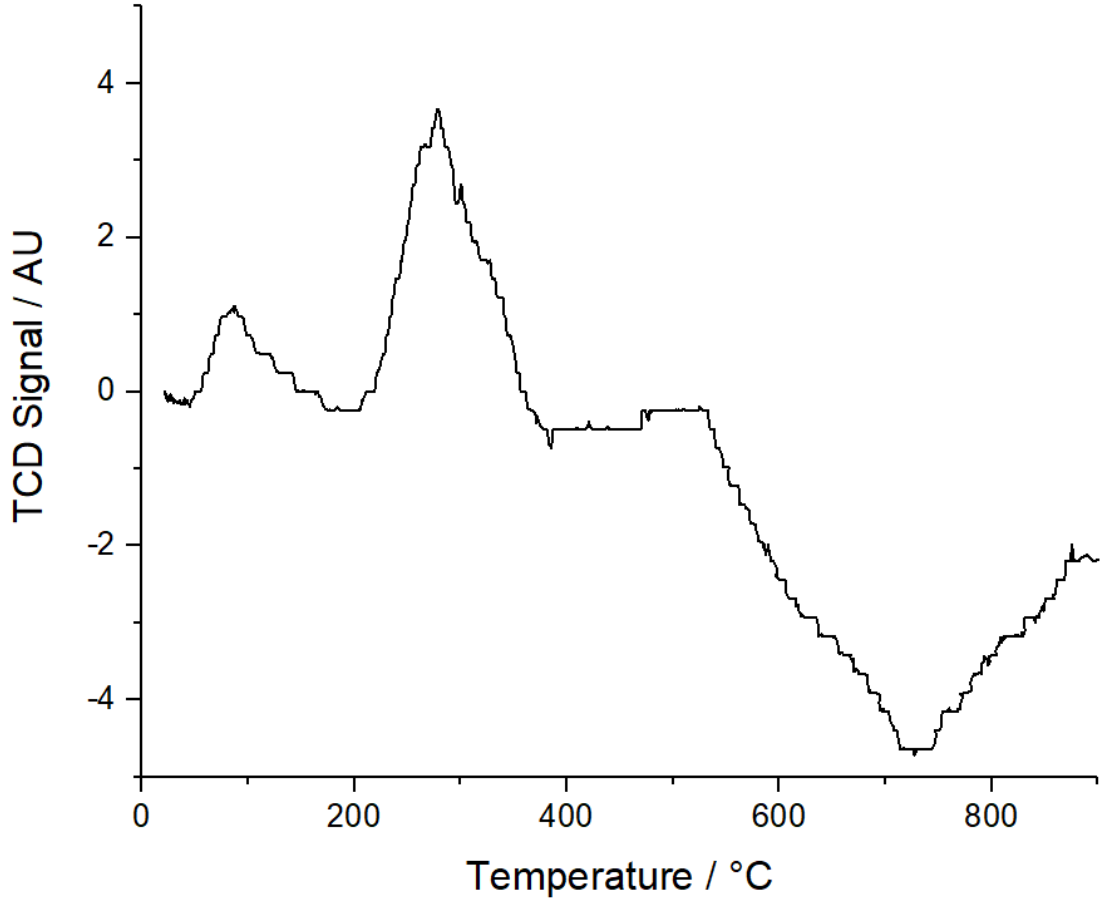

Fig. 3.9 – TPR data for the reduction of PdTA/TiO_2 to Pd/TiO_2 using H_2/Ar as the reducing gas.

The TPR data (Fig. 3.9) showed the main reduction event, marked by the increase in TCD signal, occurring between 210 and 380 °C, peaking at 300 °C. No further events were observed until greater than 550 °C, when a negative TCD signal was observed, likely as a result of changes to the gas flow as a result of the temperature.

Using this information, the reduction temperature in future scaled-up preparations of Pd/TiO_2 was set at 400 °C (673 K). This is slightly above the temperature at which the signal has returned to the baseline following the oxidation peak, suggesting a high enough temperature to result in complete reduction of PdTA, but without being high enough to cause further changes to the sample.

3.2.3 Characterisation

Following the information gained on the uptake of PdTA on TiO_2, a scaled-up impregnation was carried out using a starting pH that yielded a final pH 11, the pH of optimal uptake. Reduction was carried out at 673 K with 100 mL min^{-1} of flowing hydrogen (5% H_2 in Ar). This yielded a larger sample size of SEA-prepared Pd/TiO_2 that could be characterised.

The XRD pattern of Pd/TiO_2, displayed by Fig. 3.10, does not exhibit the presence of Pd nanoparticles. The highest-intensity reflection of metallic Pd, assigned to Pd(111), occurs at a 2θ position of 40°.[240] No peak at this position is observed that exceeds the baseline. This suggests that if the Pd NPs present on the support are < 4 nm in diameter. However, this data alone does not confirm the presence of Pd. As such, further characterisation was required.

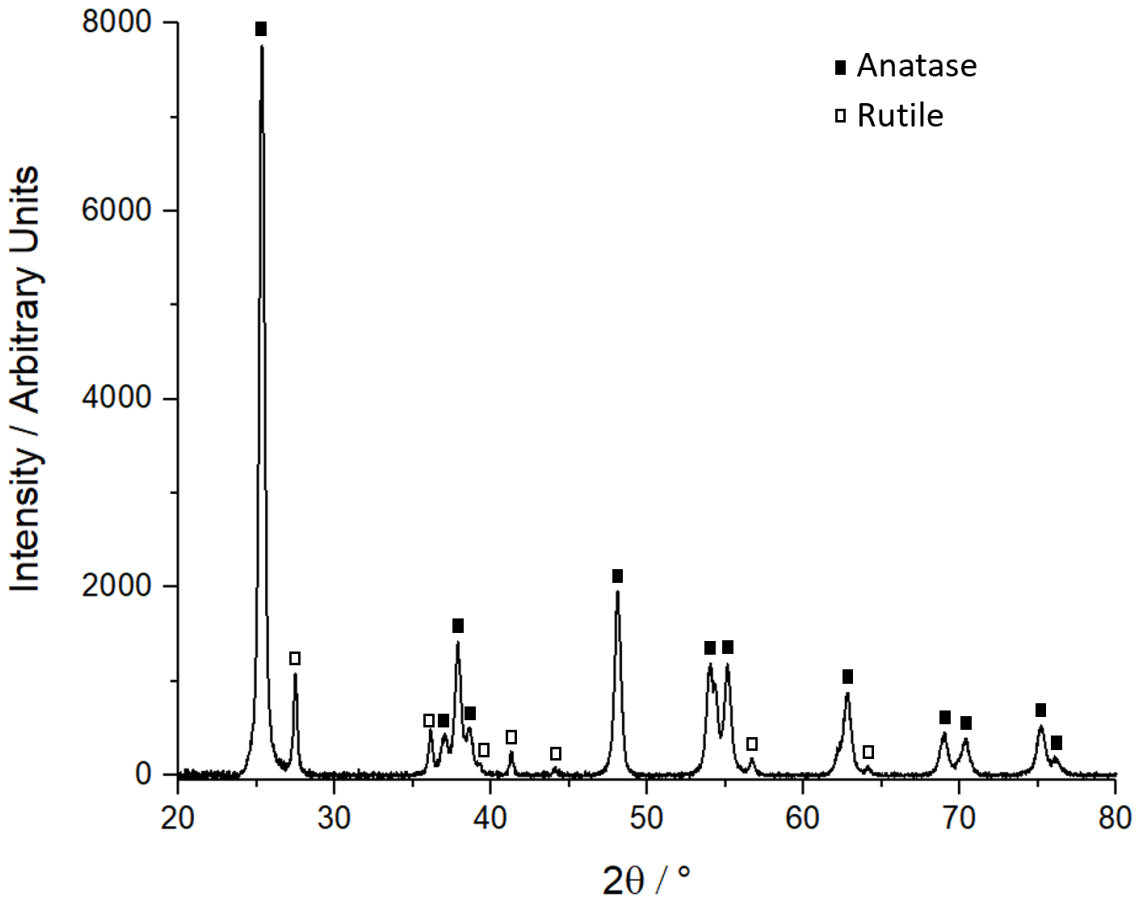

Fig. 3.10 – XRD pattern of SEA-prepared Pd/TiO_2.

Since XRD failed to show the presence of Pd, XPS was used to confirm Pd presence and quantify the loading. Fig. 3.11 shows the XPS spectrum obtained for SEA-prepared Pd/TiO_2.

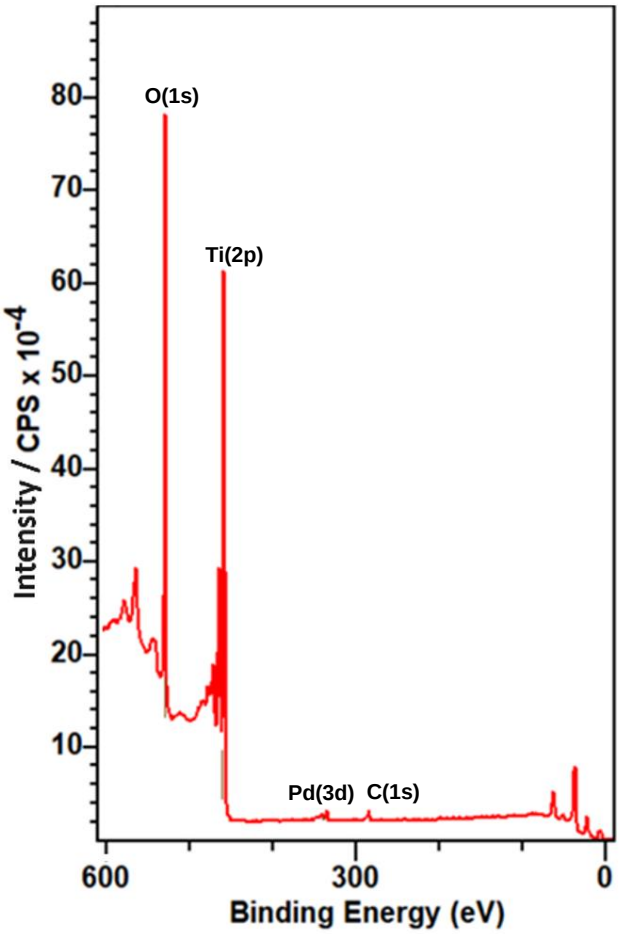

Fig. 3.11 – XPS spectrum of SEA-prepared Pd/TiO_2.

The small peak at 285 eV was assigned as C (1s). This was attributed to organic contaminants, since no organic compounds were used in the preparation of this sample.

The small doublet peak at 335 eV was assigned as Pd (3d). The two peaks are representative of $3d_{5/2}$ and $3d_{3/2}$, as demonstrated in the detailed Pd (3d) scan in Fig. 3.12. The larger peak of the doublet, which occurs at 335 eV, was assigned as Pd $3d_{5/2}$. The smaller peak, at 341 eV, was assigned as Pd $3d_{3/2}$. The position of the $3d_{5/2}$ peak at 335 eV suggests Pd is in its neutral state and is not oxidised.

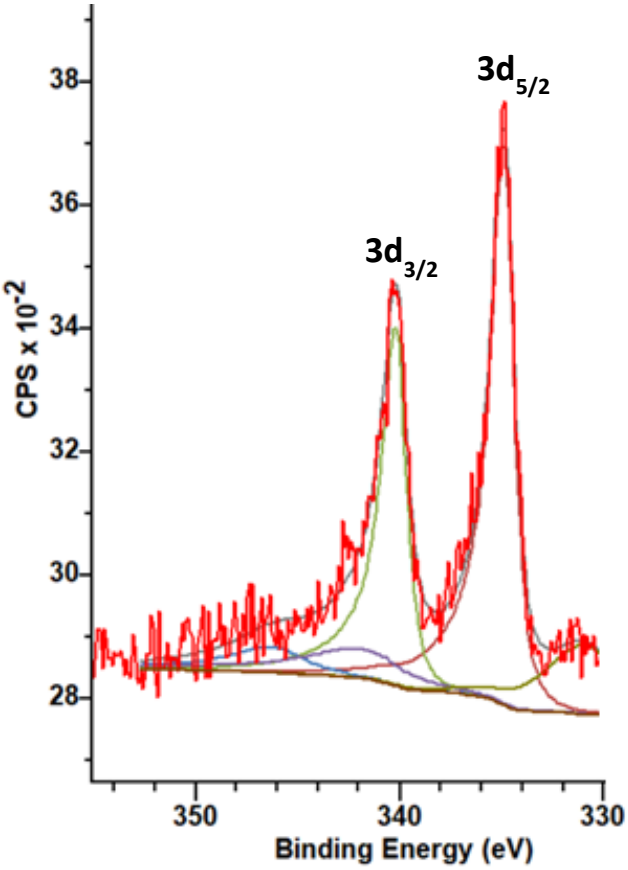

Fig. 3.12 – Detailed Pd (3d) scan within the Pd/TiO_2 XPS spectrum.

In order to check for unreduced PdTA or the presence of PdTA decomposition-related contaminants, N (1s) and Cl (2p) were also scanned for during this experiment. Should the reduction and decomposition of PdTA be incomplete, these elements would be present in the sample. These peaks would be expected to occur at 400 eV and 200 eV respectively.[241,242] Since peaks of these positions are not present on the spectrum, these elements are not present in the sample in any measurable quantity. This suggests full decomposition and removal of the PdTA salt to elemental Pd^0. This is further supported by the position of the Pd ($3d_{5/2}$) peak showing the neutral oxidation state of Pd.

Quantitative data was also obtained for Pd/TiO_2. Table 5 summarises this data.

Table 5 – Quantitative XPS data for SEA-prepared Pd/TiO_2.

Element (Orbital)	**Binding Energy / eV**	**Atomic %**	**Weight %**
C (1s)	285	3.91	**1.86**
O (1s)	530	67.52	**42.93**
Ti (2p)	459	28.20	**53.64**
Pd (3d)	335, 341	0.37	**1.56**

When C (1s) is discounted as organic impurities, this data shows the wt.% of Pd present to be 1.59%. This is considerably higher than the calculated approximate of 0.6 wt.%. In fact, this is higher than the theoretical maximum loading if all PdTA from the solution had been adsorbed. This is because XPS measures up to a depth of 1-10 nm beneath the surface of the sample,[243] which corresponds to several atomic layers. Since the Pd nanoparticles are only present on the TiO_2 surface and not within the bulk TiO_2 lattice, which is unseen by XPS, this leads to an overestimate of the wt.% of Pd within the sample. However, this scan has confirmed the presence of Pd, as well as confirming the decomposition of the precursor and the neutral Pd oxidation state.

EDX quantification of Pd/TiO_2 gave a wt.% of 0.50(8), when an average was taken across three sites. This is more in line with the expected value of Pd within the sample. However, these EDX sites were on the micron scale across, yielding a small sample size for measurement.

TEM imaging of the Pd/TiO_2 catalyst (Fig. 3.13) also confirmed the presence of Pd nanoparticles. All nanoparticles in the image were determined to be less than 5 nm in diameter. The small particle size is consistent with the small sizes reported by Regalbuto.[214,217]

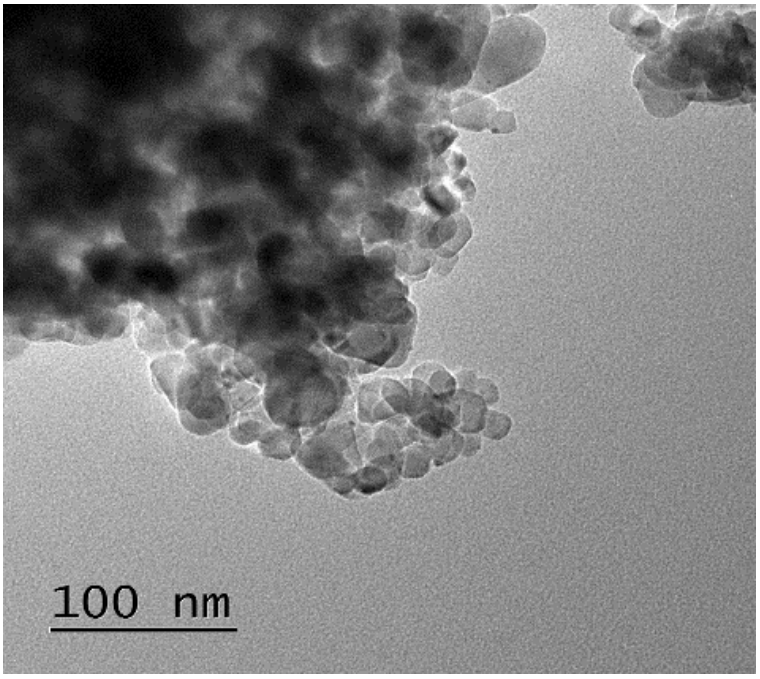

Fig. 3.13 – TEM image of Pd/TiO_2. Pd nanoparticles are clearly visible on the supporting material. All nanoparticles present have diameters of below 5 nm.

3.3 Proof of Concept BMNP $PdPt/TiO_2$ Synthesis Via Co-SEA

In an evolution of the monometallic Pd/TiO_2 sample, the use of SEA in the preparation of supported bimetallic nanoparticle samples was investigated. As proof-of-concept for co-SEA and following Regalbuto's publication, the bimetallic $PdPt/TiO_2$ composition was considered.

3.3.1 Analysis of Supporting Materials and Monometallic Precursors

For this experiment, the Pt precursor used was $[Pt(NH_3)_4]Cl_2$, platinum tetraammine, or PtTA. In aqueous solution, this provided a source of $[Pt(NH_3)_4]^{2+}$ cations. Similar to PdTA, this cationic precursor was used because of the low-PZC nature of TiO_2. Using a 1 mM PtTA solution and a TiO_2 surface loading of 500 $m^2\ L^{-1}$, an uptake survey of Pt on TiO_2 was carried out. Fig. 3.14 shows the results of this uptake survey.

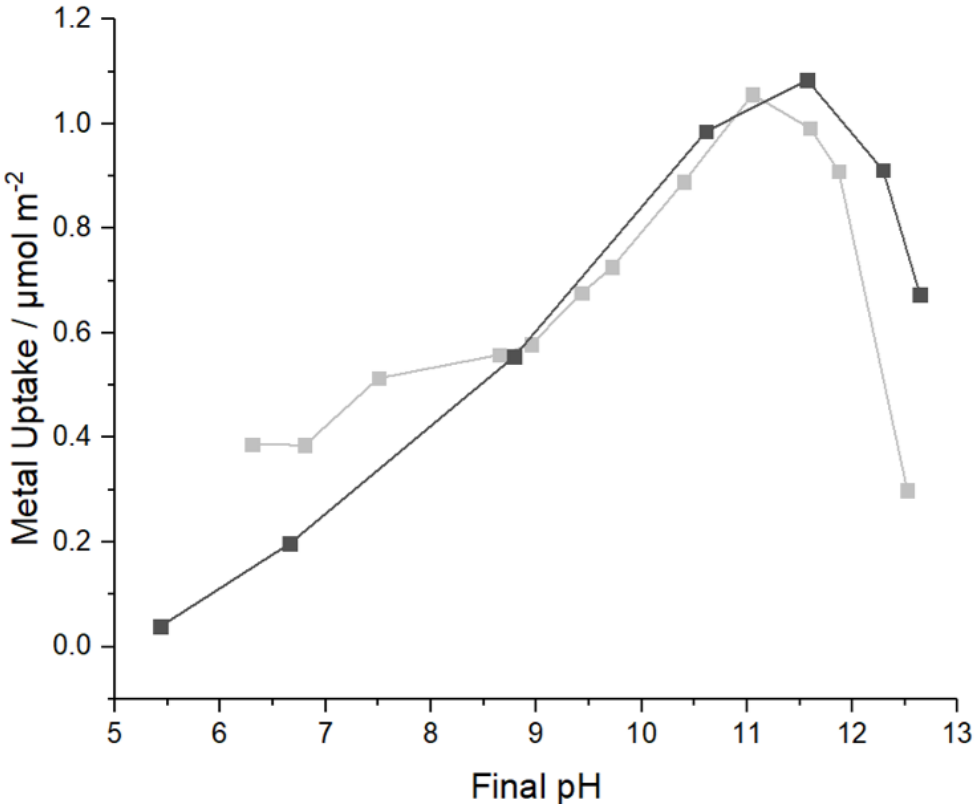

Fig. 3.14 – Metal uptake survey of Pt onto TiO_2, calcined (black). The uptake survey of Pd on TiO_2 has been included for comparison (grey).

The uptake survey of Pt on TiO_2 (black) showed a maximal uptake of 1.05 µmol m^{-2}, which corresponded to 53% of the Pt in solution being adsorbed onto the TiO_2 surface, and a 0.95 wt.% loading. The maximal molar uptake was very similar in value to that obtained with Pd. This further supports the postulate of an inherent uptake limit on TiO_2 of approximately 1 µmol m^{-2}, due to the retention of two hydration sheaths surrounding the complex when adsorbed onto the metal oxide surface limiting the packing density. However, at 0.95 wt.%, the wt.% loading of Pt was higher than Pd. This was owing to the greater atomic mass of Pt compared to Pd.

The maximum uptake occurred at a final pH of 11.5. This was similar to the uptake survey of Pd on TiO_2, which occurred at 11. Both the maximum uptake value and final pH of the Pt/TiO_2 uptake survey closely matched the values obtained in Pd/TiO_2 uptake survey. The similarity of the pH values of maximal uptake allowed a simultaneous uptake survey to be investigated.

Using this information, a proof-of-concept simultaneous uptake survey of Pd and Pt on TiO_2 was carried out. 1 mM of PdTA and 1 mM PtTA aqueous solutions were prepared and mixed together in order to prepare a single solution with both metals. Fig. 3.15 and Table 6 show the results obtained for this uptake survey. The monometallic Pd and Pt uptake surveys have been included for comparison.

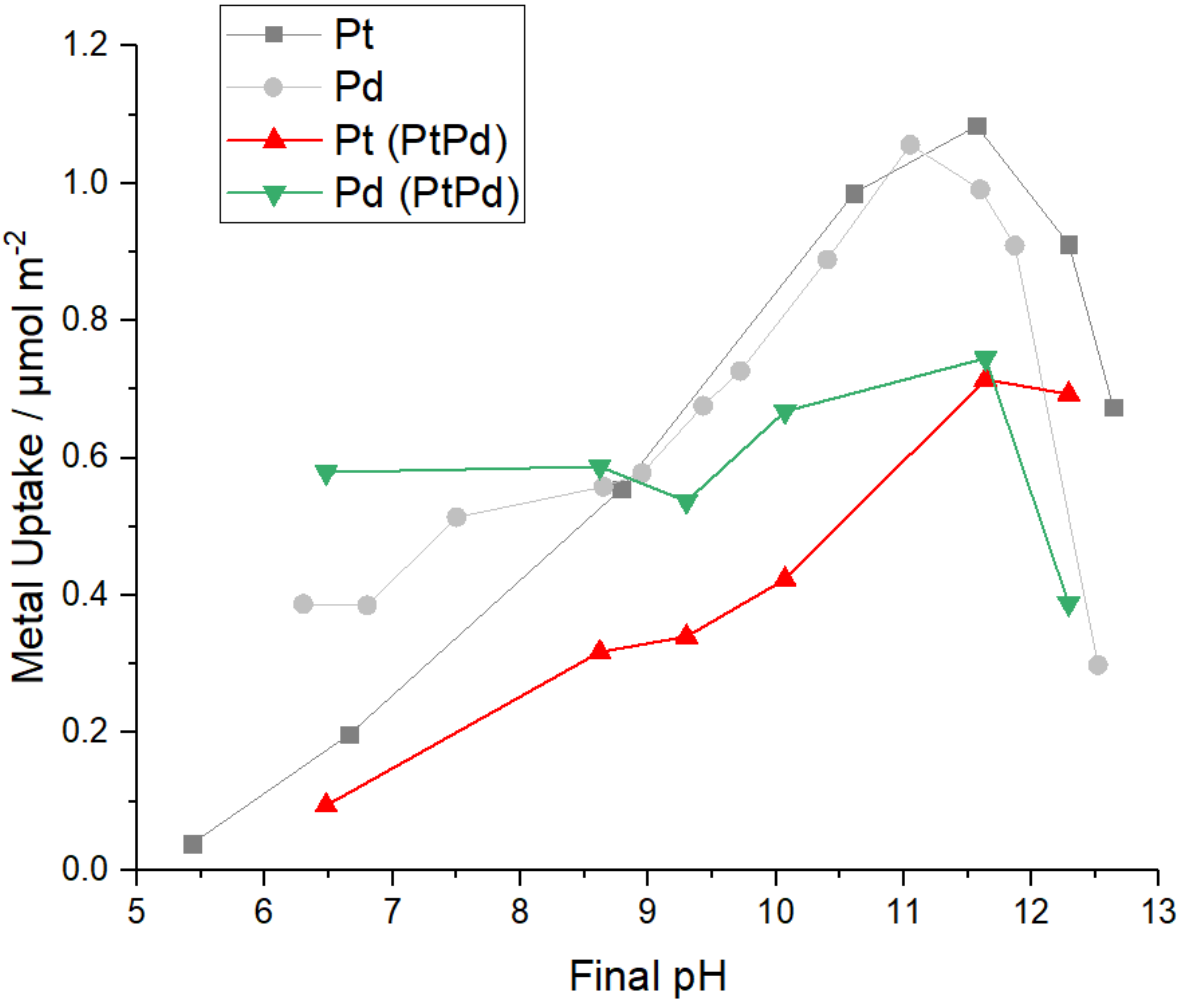

Fig. 3.15 – Simultaneous metal uptake survey of Pd and Pt onto TiO_2, calcined. The Pt component has been displayed in red, the Pd component in green. The uptake surveys of Pd and Pt on TiO_2 has been included for comparison (dark and light grey respectively).

Table 6 – The ratio of Pt:Pd uptake at each data point of the simultaneous Pd and Pt uptake survey on TiO_2. At each data point, the total uptake has been included as well. The pH of optimal uptake has been highlighted in **bold**.

Final pH	**Pt:Pd Uptake Ratio**	**Total Uptake / µmol m^{-2}**
6.48	0.162	0.673
8.62	0.541	0.905
9.30	0.633	0.877
10.07	0.634	1.09
11.64	**0.959**	**1.46**
12.29	1.79	1.08

As expected from the monometallic uptake surveys, the final pH of optimal uptake for $PtPd/TiO_2$ was around 11.5, with the exact value in this dataset being 11.64. Also as expected, the pH of optimal uptake was also where the ratio of the uptake of the two metals was closest to 1:1. The molar uptakes of the individual components were expectedly less than those of the monometallic uptake surveys. However, the overall uptake was greater than that achieved by any of the monometallic uptake surveys, a total of 1.46 µmol m^{-2} at the pH of optimal uptake. The total metal loading was therefore approximately 1.5 wt.%.

This simultaneous adsorption of Pt and Pd on TiO_2 was scaled up. TPR data revealed a reduction temperature of 723 K was required to reduce both precursors to form the $PdPt/TiO_2$ BMNP. The scaled-up impregnation was carried out, and the solid was reduced using 5% H_2/Ar at 723 K (ramp 3 K min^{-1}) for 2 hours and a flow rate of 100 mL min^{-1} of gas. A preliminary PZC experiment determined the PZC of $PdPt/TiO_2$ to be 7.75, marking this material as a mid-PZC supporting material.

3.3.2 Summary and Future Work

The results from the uptake surveys proved the possibility of simultaneous SEA as a method of synthesising a BMNP, affirming the research conducted by Regalbuto. Beyond the scope of this project, this work has potentially paved the way for expansion of this procedure to synthesis of supported TMNPs.

If a TMNP catalyst were synthesised via co-SEA, all three metals would need to have similar or identical optimal pH uptake values. In the case of TiO_2, all metal precursors would need to be cationic. While this is straightforward for metals such as Pd and Pt, which have readily available tetraammine complexes, this may prove challenging for metals such as Au, which do not have a readily available cationic complex which is stable up to a pH of 13.

In order to expand SEA to the synthesis of TMNP AuPdPt/TiO_2 system for a reaction such as methanol synthesis, two SEA steps could be carried out. First, PdPt/TiO_2 could be synthesised through co-SEA, as carried out above, followed by a second SEA step to add Au separately. Since PdPt/TiO_2 was experimentally proven to have a PZC of 7.75, an anionic Au complex at low pH values could be utilised to add Au. Unlike cationic Au precursors, an anionic Au precursor, $HAuCl_4$, is readily commercially available, forming anionic $[AuCl_4]^-$ in aqueous solution.

In order to prove the existence of the three metals, XPS and EDX mapping should be used. In addition to confirming the presence of the metals, EDX would map their distribution, thus determining the structure. XPS could aid in determining electronic interactions, metallic oxidation states, and the extent of alloying present. In addition, EDX and XPS could be used to determine the ratio of the metals. TEM imaging could be used to determine the size of the TMNPs.

Finally, these TMNPs could be catalytically tested for CO_2 hydrogenation to methanol. Such a catalyst could also be tested for other reactions, such as the direct formation of hydrogen peroxide from H_2 and O_2, a reported application for AuPdPt TMNPs.[244]

3.4 Combining Methods to Obtain Bimetallic Compositions

In terms of developing a catalyst for the CO_2 hydrogenation reaction, in an evolution of the monometallic Pd/TiO_2 sample, the use of SEA in the preparation of supported bimetallic nanoparticle samples was investigated. The target bimetallic catalyst for the hydrogenation of CO_2 to methanol was $PdZn/TiO_2$. However, this target catalyst proved far more challenging when using SEA alone compared to the synthesis of $PdPt/TiO_2$.

3.4.1 Unsuccessful Attempts to Use Zn in SEA Procedures

Initial experiments attempted to use SEA for the addition of both metals both simultaneously and sequentially. However, finding a suitable precursor for Zn that would be viable for SEA proved challenging. In order to adsorb to the negatively-charged TiO_2 surface, the precursor would need to provide a source of Zn^{2+}. Readily available water-soluble precursors such as $Zn(NO_3)_2$, $Zn(SO_4)_2$, $Zn(OAc)_2$, and $ZnCl_2$ were unsuitable. Upon dissolution of these compounds, solvated Zn^{2+} forms. Addition of NaOH to solvated Zn^{2+} results in formation of insoluble $Zn(OH)_2$, which immediately precipitates out of solution, and the sodium salt of the counterion. The precipitation of Zn out of solution renders all of these precursors unsuitable, since Zn must be in solution to adsorb onto the supporting material.

In order to overcome this issue, Zn must be solvated as a metal-ligand complex that resists reaction with hydroxide ions and is stable up to a pH of 13. The most viable complex would be $[Zn(NH_3)_4](OH)_2$, or ZnTA, the zinc analogue of PdTA, which could be readily synthesised. Supposedly, $Zn(OH)_2$ and concentrated excess NH_4OH react to form a solution of ZnTA. Through rigorous stirring, $Zn(OH)_2$ and NH_4OH would react, resulting in the observed dissolution of the hydroxide to form a clear and colourless solution of ZnTA.[245] Several attempts were made to replicate the synthesis of this procedure to produce ZnTA, however none were successful. A range of molar stoichiometries and reaction temperatures were investigated, but in each case no dissolution of $Zn(OH)_2$ was observed, suggesting no reaction between $Zn(OH)_2$ and NH_4OH was occurring. The reasons behind the failure of this procedure are currently unknown.

Experiments using H_2ZnCl_4 were also attempted. This compound could be readily synthesised using aqueous $ZnCl_2$ and HCl in a 1:2 molar ratio. In addition, the zinc in

this compound is in the form of a coordination complex, rather than solvated Zn^{2+}. At 1 mM the pH of this solution was measured as 2.73. Up to a pH of 11, no changes were observed. However, at higher pH, a white precipitate was formed. Since this precursor was not viable for the entire pH range of an uptake survey, especially since initial and final pH values would be 11 or greater for this uptake survey, this precursor could not be used. The same occurred when Na_2ZnCl_4 was used as the precursor.

No other readily available or cost-effective Zn-based precursors were available from Sigma Aldrich, Merck, or American Elements. This, along with the previously discussed unsuccessful attempts at using or synthesising a suitable Zn precursor, demonstrated that SEA is not a feasible method to introduce Zn as a MNP to a catalyst. Hence, other methods for Zn addition were considered. In particular, the use of CVI for incorporation of Zn was investigated.

Zn could be incorporated as a metal in a supported bimetallic composition using CVI. The procedure, as detailed in chapter 2, was a simple and effective way to accomplish this. As such, a mixed-method synthesis combining SEA and CVI was investigated to synthesise supported bimetallic PdZn nanoparticle catalysts.

3.4.2 PZC of Zinc-Containing Supporting Materials

Prior to PZC experiments, ZnO/TiO_2 was prepared using CVI, following the procedure detailed in chapter 2, which should yield ZnO/TiO_2 with approximately 15 wt.% ZnO. BET surface area analysis of this sample showed a surface area of 50 $m^2\ g^{-1}$. This was considered sufficient for PZC investigations, uptake surveys, and potential impregnation procedures.

In addition, the PZC of HSA-ZnO was investigated in order to determine if ZnO could double as a second metal and the supporting material. Following the procedure detailed in chapter 2, HSA-ZnO was prepared using $Zn(NO_3)_2{\cdot}6H_2O$ and $(NH_4)_2CO_3$. A small portion HSA-ZnO was exposed to a pH of 13 for 1 hour to emulate the conditions of an uptake survey. BET surface area analysis showed a surface area of 69 $m^2\ g^{-1}$ for both samples. Thus, exposure to high pH in an aqueous environment did not result in a loss of surface area.

For each PZC experiment, a surface loading of approximately 10,000 $m^2\ L^{-1}$ was used.

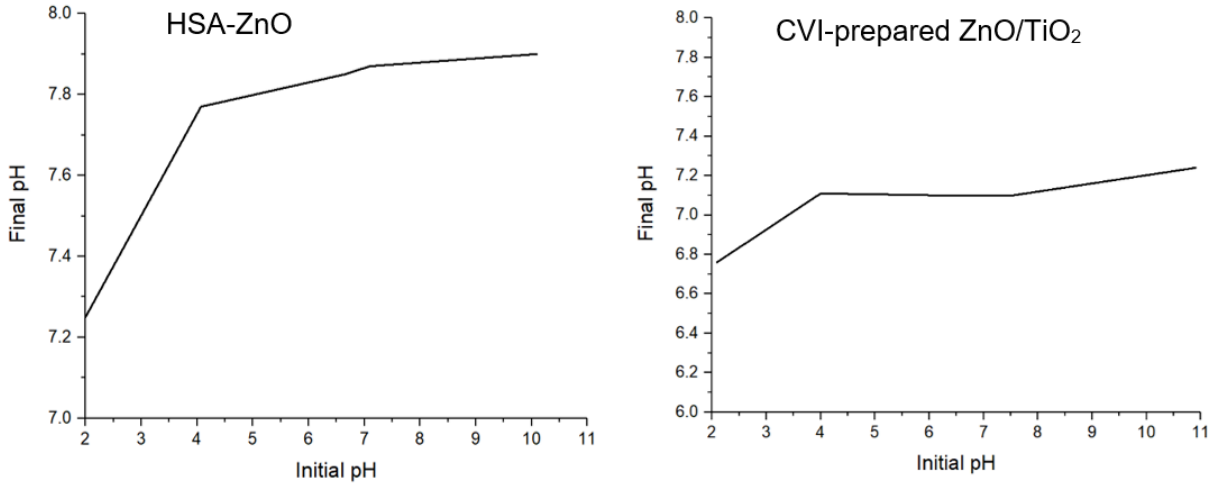

Fig. 3.16 – PZC graphs of a) HSA-ZnO, and b) CVI-prepared ZnO/TiO_2.

The PZC of HSA-ZnO (Fig. 3.16a) and CVI-prepared ZnO/TiO_2 (Fig. 3.16b) were taken to be 7.9 and 7.1 respectively. These were therefore both considered mid-range PZC supports, able to accommodate metal uptake at both high and low pH values. The slightly lower PZC of ZnO/TiO_2 was to be expected, given the influence of the far lower PZC of TiO_2.

3.4.3 Uptake Surveys of Pd on Zn-containing Materials

In order to add Pd to the Zn-containing materials via SEA, uptake surveys of Pd on these materials were investigated. Uptake surveys in the basic pH range (7.5-13) were carried out on HSA-ZnO and CVI-prepared ZnO/TiO_2 to assess either material's feasibility for the use of SEA to add Pd. Fig. 3.17 displays the results of these uptake surveys. For comparison, the uptake survey of Pd on TiO_2 (P25) is included. For these experiments, the surface loading of the Zn-containing materials was 500 m^2 L^{-1}.

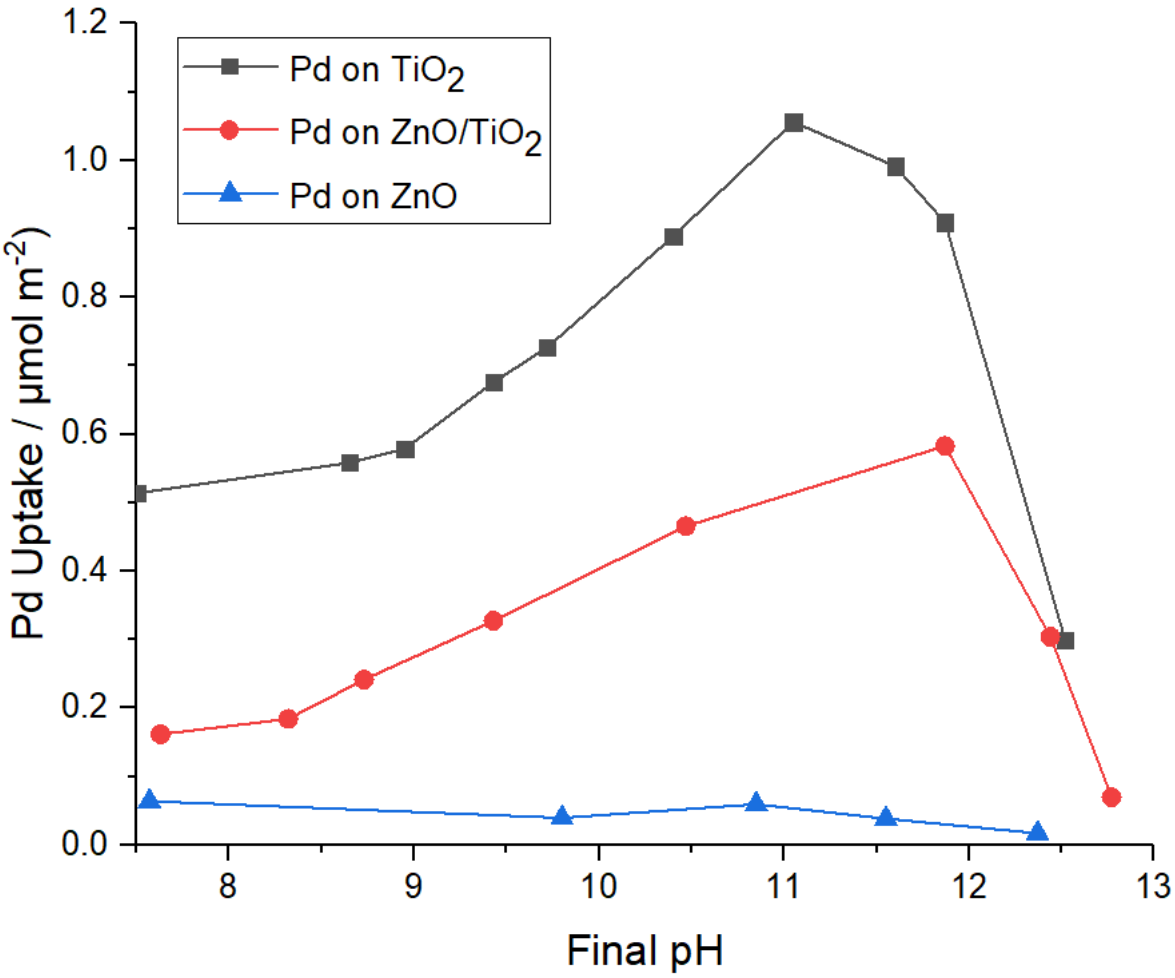

Fig. 3.17 – Uptake surveys of Pd on TiO_2 (P25) (grey), CVI-prepared ZnO/TiO_2 (red), and HSA-ZnO (blue).

As seen in Fig. 3.17, the uptake of Pd onto HSA-ZnO was minimal in the basic pH range. Given the PZC of 7.9, stronger surface charging is predicted to occur in the basic pH range. However, at pH values far more basic than the PZC, negative surface charging which would attract the cationic Pd complex should occur. Despite this, minimal uptake of Pd was observed. In addition, no trend was observed. The expected shape of an uptake survey, involving increasing uptake towards an optimum and then loss of uptake at higher pH values than the optimum, was not observed. Instead, there was no correlation between pH value and uptake.

With Pd on CVI-prepared ZnO/TiO_2, the maximum uptake was achieved with a final pH of 11.8. The measured Pd uptake at this pH was 0.583 µmol m^{-2}. This corresponded to a Pd loading of 0.31 wt.%. By comparison, the Pd uptake on TiO_2 was greater than 1 µmol m^{-2}, approximately 45% greater than the Pd uptake on ZnO/TiO_2.

There are two possible explanations for the reduced Pd uptake. The first is the fact the PZC of ZnO/TiO_2 was 7.1, while the PZC of TiO_2 was 3.6. The optimal final pH when using TiO_2 is further removed from the PZC than the optimal final pH with ZnO/TiO_2, resulting in a greater extent of surface charging for TiO_2 than ZnO/TiO_2, and thus a stronger interaction with the Pd complex.

The other possibility, supported by EDX data and elemental mapping (Fig. 3.18), is the structure of the ZnO/TiO_2 sample. Although the expected Zn distribution was a monolayer of ZnO over the TiO_2, the elemental mapping shows an uneven distribution of Zn. This suggests the formation of ZnO aggregates, rather than a homogeneous ZnO coating. This would leave areas of TiO_2 exposed, to which the Pd complex is preferentially adsorbing to. This is backed up by the uptake survey showing minimal to no uptake of Pd onto ZnO. Thus, the reduced uptake of Pd onto ZnO/TiO_2 can be attributed to ZnO blocking sites where Pd would adsorb onto TiO_2.

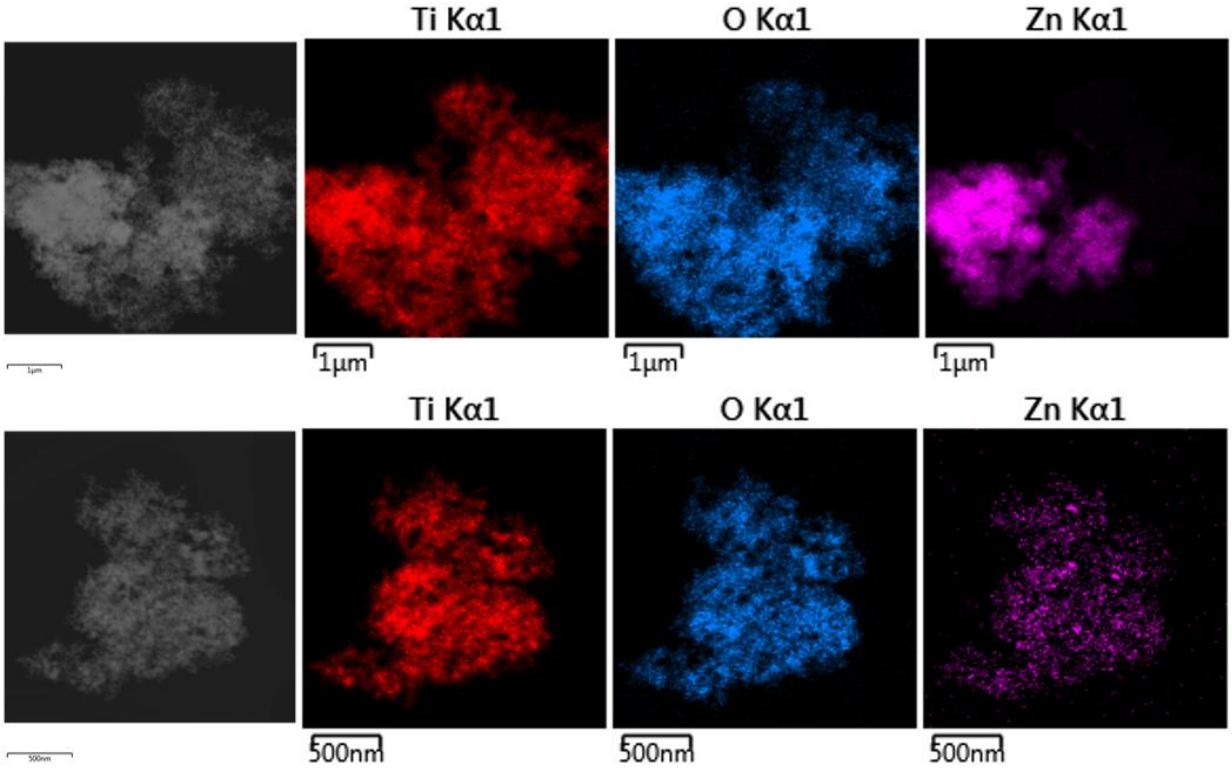

Fig. 3.18 – EDX elemental mapping of CVI-prepared ZnO/TiO_2, based on SEM images. Red=Ti, Blue=O, Magenta=Zn. The measured sites are a) approximately 25 square microns (top), b) and 4 square microns (bottom).

As seen in Fig. 3.18a, there exist entire regions where no Zn is present at all. These images suggest the Wolmer-Weber island formation mode of ZnO growth, rather than a continuous monolayer or Stranski-Krastanov growth.[246]

TPR was carried out to determine the reduction temperature of Pd on ZnO/TiO_2 (Fig. 3.19). In contrast to PdTA reduction on TiO_2, the reduction event occurred at a higher temperature. The peak reduction occurred at 460 °C. At temperatures greater than 500 °C, another reduction event occurred, resulting in a larger peak. This was assigned as reorganisation of ZnO and TiO_2, or temperature-induced changes to the gas stream. In order to reduce the PdTA without changes occurring in the supporting material, a reduction temperature of 500 °C (773 K) was selected for future preparations of $Pd/ZnO/TiO_2$.

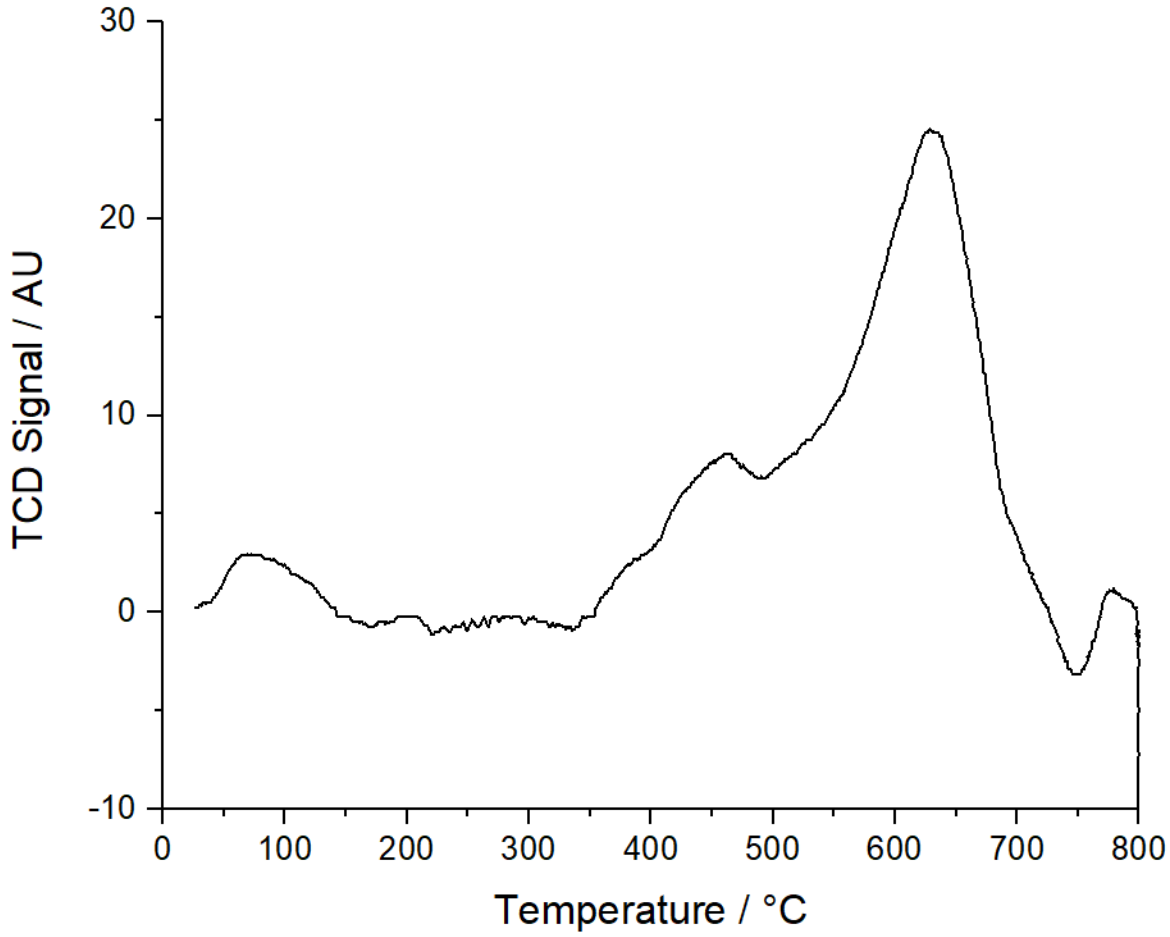

Fig. 3.19 – TPR data for the reduction of $PdTA/ZnO/TiO_2$ to $Pd/ZnO/TiO_2$ using H_2/Ar as the reducing gas.

3.4.4 Characterisation of $Pd/ZnO/TiO_2$

Following the information gained on the uptake of PdTA on ZnO/TiO_2, a scaled-up impregnation was carried out using a starting pH that yielded the optimal pH of uptake. Reduction was carried out at 773 K with 100 mL min^{-1} of flowing hydrogen (5% H_2 in

Ar). This yielded a larger sample size of Pd/ZnO/TiO_2 prepared via CVI followed by SEA that could be characterised.

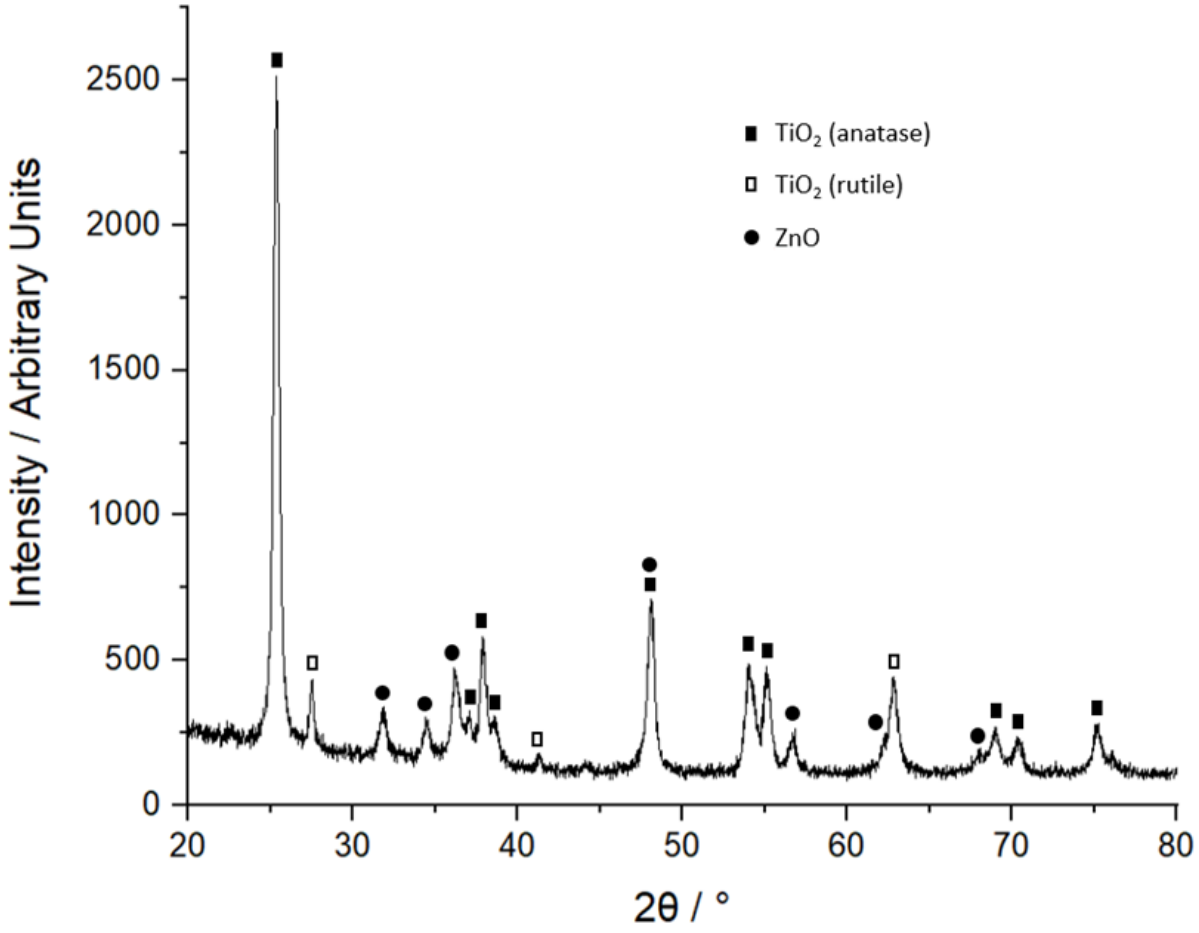

Fig. 3.20 – XRD pattern of Pd/ZnO/TiO_2 prepared via CVI followed by SEA.

XRD (Fig. 3.20) confirmed the presence of both ZnO and TiO_2 in this sample. The reflections at positions 32, 35, 37, 56, 62, and 67° match the literature pattern of ZnO.[247] The remainder of the reflections were assigned as TiO_2. Similar to the Pd/TiO_2 pattern, no reflection occurred at 40°, which would be the highest-intensity reflection for elemental Pd, Pd(111).

XPS was used to obtain further information. Specifically, the quantities of Pd and Zn at the surface, and to determine if alloying between Pd and Zn occurred. Fig. 3.21 shows the detailed Pd 3d scan obtained for Pd/ZnO/TiO_2.

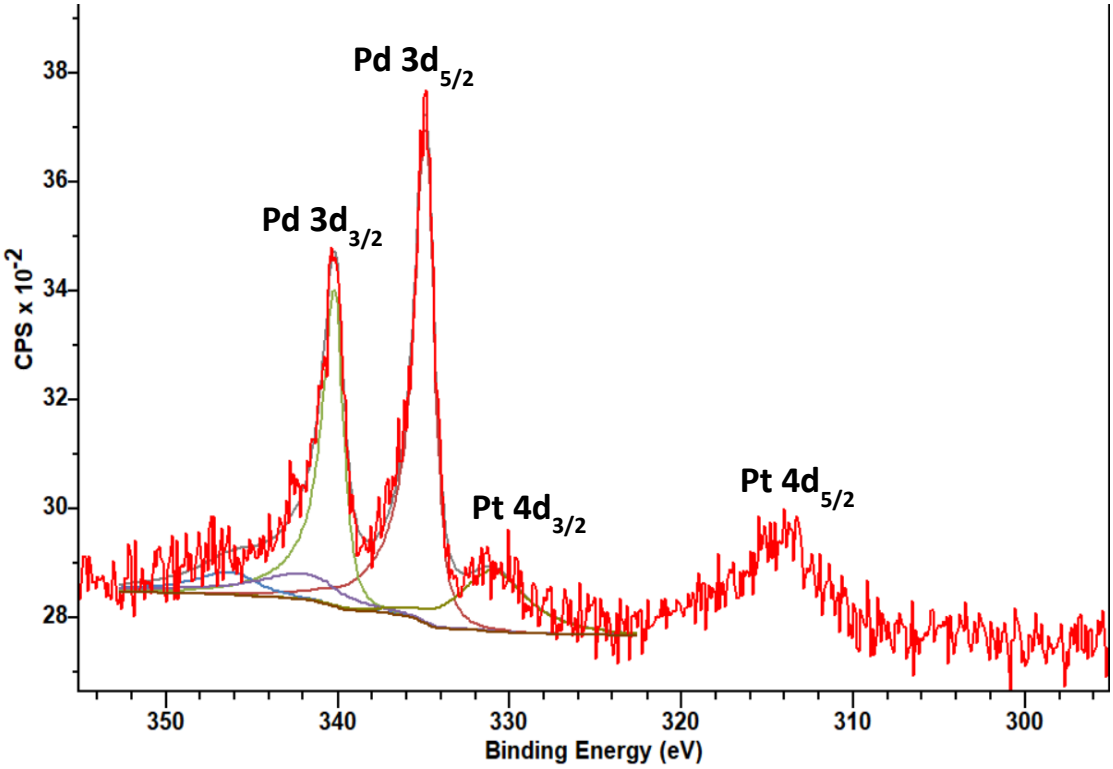

Fig. 3.21 – Detailed Pd 3d XPS spectrum of Pd/ZnO/TiO_2 prepared via CVI followed by SEA. This spectrum reveals Pt contamination.

In this sample, the Pd $3d_{5/2}$ peak occurred at a BE of 335 eV, diagnostic of Pd^0. However, in this region, two additional low-intensity peaks are present at 331 and 314 eV. These peaks match the BE for Pt $4d_{3/2}$ and Pt $4d_{5/2}$ respectively. This sample was not expected to contain Pt, suggesting Pt was present as a contaminant. The source of this contamination is unknown. A likely source was an improperly washed volumetric flask used to prepare the Pd precursor solution, since this flask was also used to prepare Pt stock solutions. However, crucially, due to the absence of two subpeaks expected within the $3d_{5/2}$ and $3d_{3/2}$ peaks,[251] this spectrum does not show evidence of Pd-Zn alloying. Table 7 displays the full quantitative dataset obtained for the XPS scan of Pd/ZnO/TiO_2.

This quantitative data confirms the presence of both Pd and Zn, showing the success of the mixed synthesis method in producing a sample with both metals present. The Pd wt.% (ignoring Carbon) is 0.65%. As expected, this is considerably lower than the Pd/TiO_2 run, where the Pd wt.% was measured to be 1.59 wt.% This was expected because previous uptake surveys have shown Pd uptake on ZnO to be far less than on TiO_2, and this lower Pd uptake onto ZnO/TiO_2 was reflected in the Pd on ZnO/TiO_2 uptake survey (Fig. 3.17).

Table 7 – Quantitative XPS data for Pd/ZnO/TiO_2 prepared via CVI followed by SEA.

Element (Orbital)	**Binding Energy / eV**	**Atomic %**	**Weight %**
C (1s)	285	4.99	**2.40**
O (1s)	530	66.97	**42.92**
Ti (2p)	459	27.11	**51.98**
Zn ($2p_{3/2}$)	1022	0.79	**2.07**
Pd (3d)	335, 341	0.15	**0.64**

As previously discussed, however, XPS quantification of metal loadings presents an overestimate. As such, EDX has been used to provide a more accurate quantification of Pd and Zn loadings. Average readings across three sites determined the Pd loading to be 0.31(3) wt.%, and the Zn loading to be 6.60 wt.%. This Pd loading was more in line with what was expected, given the lower Pd uptake on ZnO/TiO_2 than TiO_2, and the wt.% calculations from the measured Pd uptake. The Zn:Pd ratio was shown to be 20:1, which lined up with the ratios used in the synthetic procedure.

As already discussed in the previous section, elemental mapping (Fig. 3.19) showed the distribution of ZnO on the surface was not homogeneous, appearing in islands and aggregates (Wolmer-Weber mode of growth). This could explain discrepancies in the XPS and EDX quantification of Zn, since the XPS scan may have scanned a Zn-deficient region. However, it is worth noting that both XPS and EDX produce data only within a small sample size.

Both EDX and XPS show the quantity of Zn was lower than expected from the synthesis procedure, which was to yield 15 wt.% Zn. This shows that during the CVI procedure, much of the Zn did not adhere to the TiO_2. It is also possible that other sites may be particularly Zn-rich due to the uneven Zn distribution.

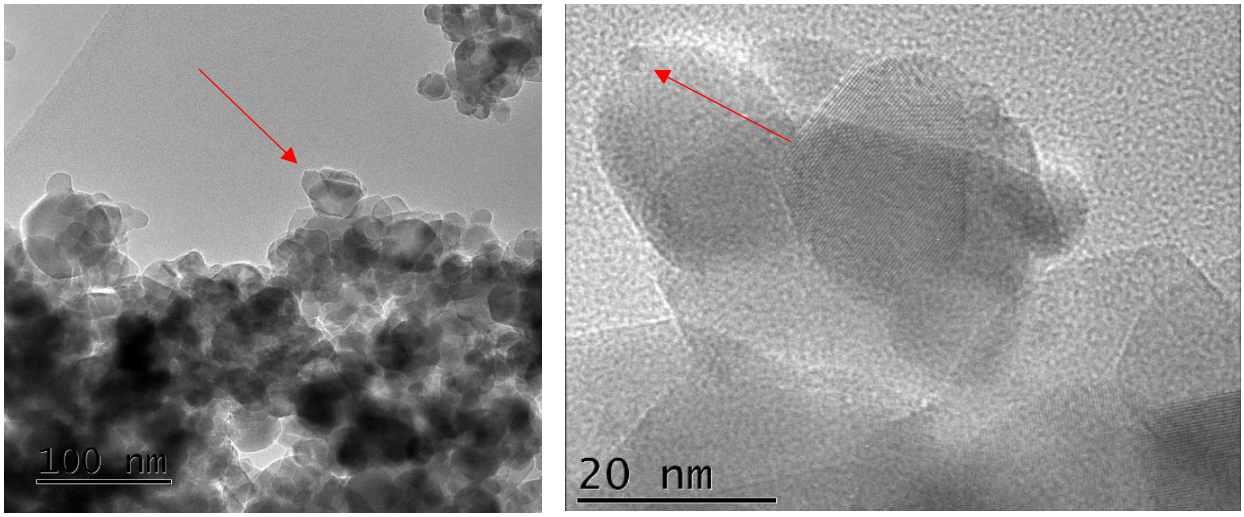

Fig. 3.22 – TEM images of Pd/ZnO/TiO_2. The image on the right (b) is the same site as the image on the left (a) but with a greater magnification. Highlighted with a red arrow is a nanoparticle.

TEM images were taken of Pd/ZnO/TiO_2 (Fig. 3.22). Owing to the lower loading of Pd/ZnO/TiO_2 as suggested by the uptake surveys (Fig. 3.17), far fewer nanoparticles are present in the Pd/ZnO/TiO_2 image than the Pd/TiO_2 image (Fig. 3.13). Fig. 3.22a shows clearly a Pd nanoparticle within the Pd/ZnO/TiO_2 sample, which can be deduced to be monometallic through the lack of alloying seen in the XPS data (Fig. 3.21).

Analysis of d-spacing between lattice planes visible in Fig. 3.22b was carried out. The d-spacing was determined to be 3.5 Å. This is consistent with the (101) plane of the anatase phase of TiO_2.[248] This confirmed TiO_2 to be the exposed surface for this site.

While this experiment proved that a two-step synthesis combining SEA and CVI could be used to develop a BMNP system, the lack of Pd-Zn alloying and very low Pd loading showed that this route was not ideal to synthesising a good catalyst candidate for the CO_2 hydrogenation reaction to methanol. An ideal candidate would have a far greater Pd loading and have the two metals alloyed. As such, an alternate synthesis route was devised.

3.4.5 Synthesis and Characterisation of ZnO/Pd/TiO_2

In order to synthesise a catalyst both containing Zn and containing a higher loading of Pd with potential to form a Pd-Zn alloy, the synthesis of ZnO/Pd/TiO_2 was investigated. Previously, Pd/ZnO/TiO_2 was prepared by first adding ZnO via CVI, and second adding Pd through SEA. For ZnO/Pd/TiO_2, the reverse sequence was applied, adding

Pd via SEA first, followed by ZnO via CVI. The maximal uptake of PdTA onto TiO_2 was 45% higher than ZnO/TiO_2, thus carrying out the SEA step first would potentially increase the Pd loading within the sample. In addition, greater Pd loading and the reverse order of steps could potentially lead to Pd-Zn alloying, specifically the formation of the β-PdZn alloy, which could in turn lead to a more active catalyst.[178]

Pd/TiO_2 was prepared using the standard SEA method, followed by a repeat of the CVI method used to prepare ZnO/TiO_2, however the supporting material was SEA-prepared Pd/TiO_2 as opposed to TiO_2. Following calcination at 773 K for 16 hours as the final stage of the CVI procedure, the colour of the sample changed from grey to peach, suggesting re-oxidisation of Pd^0 to Pd^{2+}. However, for catalytic testing this would not be an issue since catalysts entering the HTR are reduced *in-situ* beforehand at 673 K, thus re-reducing the Pd^{2+} back to Pd^0.

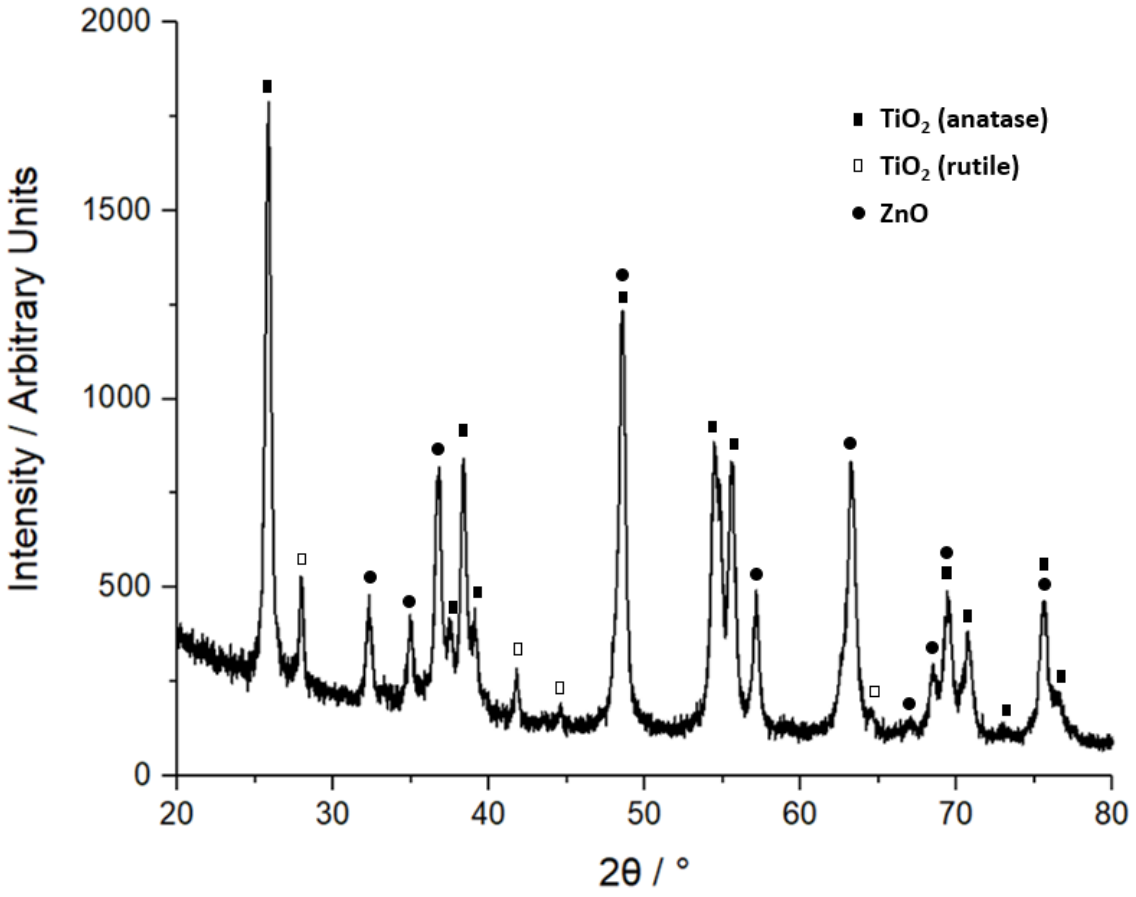

Fig. 3.23 – XRD pattern of $ZnO/Pd/TiO_2$ prepared via SEA followed by CVI.

An XRD pattern (Fig. 3.23) was taken for the $ZnO/Pd/TiO_2$ sample. This data confirmed the presence of both ZnO and TiO_2 in this sample. Similar to $Pd/ZnO/TiO_2$, the reflections at positions 32, 35, 37, 56, 62, and 67° match the literature pattern of

ZnO.[247] The remainder of the reflections were assigned as TiO_2. Similar to the Pd/TiO_2 and Pd/ZnO/TiO_2 patterns, no reflection occurred at 40°, which would be the highest-intensity reflection for elemental Pd, Pd(111). The diagnostic PdO reflection occurs at 33°, however in this pattern, any reflection at this position was obscured by the ZnO(100) reflection. The diagnostic reflection of β-PdZn(111) occurs at 40-41°, which is also not visible on this pattern.

XPS was used to obtain information on the properties of ZnO/Pd/TiO_2, and to gain insight into potential PdZn alloying. A complete scan was obtained. N (1s), Na (2s), and Cl (2p) were also scanned for during this run, none of which were detected. The lack of N and Cl suggests decomposition of PdTA, and the lack of Na suggested a lack of residual base (NaOH) present in the product. The detailed Pd 3d scan (Fig. 3.24) was analysed.

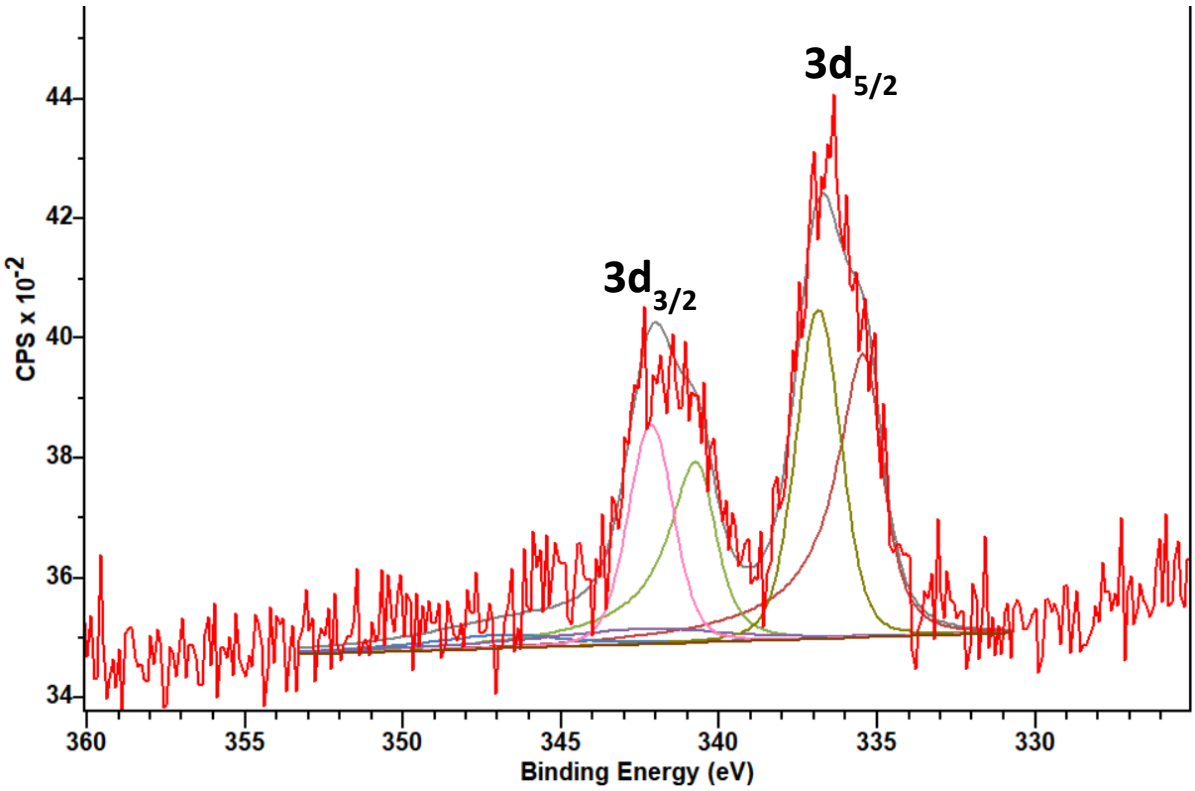

Fig. 3.24 – Detailed Pd 3d XPS spectrum of ZnO/Pd/TiO_2 prepared via SEA followed by CVI.

The position of the Pd ($3d_{5/2}$) peak, at a binding energy of 336 eV, lines up with the literature values of PdO.[249] This further suggests the Pd was oxidised by the

calcination step, lining up with the visual observation of the peach colour of the catalyst.

Table 8 displays the full quantitative dataset obtained for the XPS scan of ZnO/Pd/TiO_2.

Table 8 – Quantitative XPS data for ZnO/Pd/TiO_2 prepared via SEA followed by CVI.

Element (Orbital)	**Binding Energy / eV**	**Atomic %**	**Weight %**
C (1s)	285	18.49	**8.92**
O (1s)	530	55.56	**35.70**
Ti (2p)	459	18.75	**36.04**
Zn ($2p_{3/2}$)	1022	6.96	**18.27**
Pd (3d)	336, 342	0.25	**1.07**

Curiously, this data suggested a considerable quantity of the organic component remained. C (1s) accounted for 18.49% of the atoms in the region scanned, corresponding to 8.92 wt.%. This is more than three and a half times greater than the wt.% of C present with the Pd/ZnO/TiO_2 sample. In addition, 7.51% of atoms in the sample were assigned to organic -OH groups, with inorganic O (ZnO, TiO_2) accounting for the remaining O atoms present in the scan. This suggests incomplete decomposition of the organic component of the Zn precursor, or contamination from other organic sources.

Both Zn and Pd showed far greater loadings in this sample than XPS and EDX data implied for Pd/ZnO/TiO_2. Ignoring the significant organic contribution, both C (1s) and the organic -OH O (1s) component, the wt.% of Zn and Pd were 21.19 and 1.24 respectively. The Zn loading was more in line with what was expected for a sample prepared via CVI than Pd/ZnO/TiO_2. Moreover, a significantly greater Pd loading was

observed. The calculated wt.% of Pd for this sample was almost double that of the Pd/ZnO/TiO_2 sample. This was expected, since the Pd uptake on TiO_2 was almost double that of ZnO/TiO_2. However, it is worth noting that XPS systematically overestimates Pd loading, so the true loading is likely in the range of 0.5-0.6 wt.%, more in line with MMNP Pd/TiO_2 catalysts. The ratio of Zn:Pd wt.% was 17:1, approximately in line with the synthetic procedure.

Determining the presence of the β-PdZn alloy proved difficult from the XPS scan alone. This is because the sub-peaks present in the XPS spectrum could be the result of Pd-Zn alloying based on similarities with other reported publications,[250] but also because detailed quantitative scan data showed a mixture of Pd oxidation states Pd^0 and Pd^{2+}. The positions of the sub-peaks can also be matched with those of the two oxidation states of Pd.[251]

In addition, TEM imaging could have been useful in determining the particle sizes. Furthermore, EDX quantification could have served as a second quantitative dataset. However, time constraints and numerous experimental setbacks prevented such datasets from being obtained.

In terms of catalytic performance, the increase in both Pd and Zn in the ZnO/Pd/TiO_2 sample should result in superior catalytic performance when compared with Pd/ZnO/TiO_2.

3.5 Catalytic Testing for the CO_2 Hydrogenation Reaction

MMNP and BMNP catalysts synthesised through SEA and a mixture of SEA and CVI were tested for their catalytic activity for the CO_2 hydrogenation reaction to methanol using the 16-bed high-throughput reactor (HTR) at the Cardiff Catalysis Institute (CCI), located at the University of Cardiff.

Four samples were evaluated for catalytic activity: (i) Pd/TiO_2 prepared via SEA at optimal pH (o-Pd/TiO_2); (ii) Pd/TiO_2 prepared via SEA but without adjusting the pH of the solution (its native pH), which resulted in a final pH value far removed from the optimal pH (n-Pd/TiO_2); (iii) Pd/ZnO/TiO_2 prepared via CVI followed by SEA; (iv) ZnO/Pd/TiO_2 prepared via SEA followed by CVI. These samples were compared with a CZA control. The reaction conditions used were detailed in the Experimental chapter.

For each of these experiments, a range of by-products was formed. The main by-product was CO, a product of the RWGSR. However, another by-product that can commonly form is methane. This is the result of over-hydrogenation of CO_2, forming one molecule of CH_4 and two molecules of water. Other potential by-products are ethanol and dimethyl ether (DME). However, for all the catalysts tested, no ethanol or DME was detected. As such, all product formed that was not methanol or methane was CO. Table 9 displays the complete dataset obtained through catalytic testing.

Table 9 – Catalytic data for five catalysts: (i) CZA; (ii) o-Pd/TiO_2 prepared via SEA; (iii) n-Pd/TiO_2 prepared via SEA; (iv) Pd/ZnO/TiO_2 prepared via CVI followed by SEA; (v) ZnO/Pd/TiO_2 prepared via SEA followed by CVI. Included is the % CO_2 converted, the selectivity towards methanol, the selectivity towards an unwanted byproduct, methane, the ratio of methane to methanol produced, and the overall productivity of methanol. Each of these were measured for each catalyst at three temperatures: 230, 250, and 270 °C (503, 523, and 543 K). Unless otherwise stated in the "Sample" column, 500 mg of each catalyst was used in the reactor.

Temp / °C	**Sample**	**CO_2 conversion / %**	**MeOH selectivity / %**	**Methane selectivity / %**	**Methane: MeOH ratio**	**MeOH productivity/ mmol h^{-1} kg^{-1}**
230	CZA (50 mg)	7.2	57.9	0.00	N/A	13195
	o-Pd/TiO_2	10.6	10.5	2.8	0.267	437
	n-Pd/TiO_2	6.6	9.3	3.0	0.327	395
	Pd/ZnO/TiO_2	2.2	20.5	0.18	0.00870	179
	ZnO/Pd/TiO_2	3.5	24.9	0.16	0.00652	272
250	CZA (50 mg)	13.3	37.4	0.0071	<0.001	15669
	o-Pd/TiO_2	12.7	11.1	5.3	0.478	540
	n-Pd/TiO_2	7.3	8.7	5.1	0.588	414
	Pd/ZnO/TiO_2	4.3	20.8	0.22	0.0106	352
	ZnO/Pd/TiO_2	5.7	25.5	0.23	0.00884	447

270	CZA (50 mg)	18.3	17.9	0.025	0.00138	10321
	o-Pd/TiO_2	15.3	8.1	9.0	1.10	487
	n-Pd/TiO_2	8.0	5.8	7.3	1.25	304
	Pd/ZnO/TiO_2	8.7	20.1	0.33	0.0164	518
	ZnO/Pd/TiO_2	8.8	25.2	0.32	0.0128	683

At 230 °C, the catalyst with the highest CO_2 conversion was o-Pd/TiO_2, with a conversion of 10.6%. However, this catalyst exhibited poor selectivity towards methanol, at 10.5%. This selectivity was five times lower than the CZA catalyst. In addition, the o-Pd/TiO_2 catalyst produced a considerable quantity of methane, with a methane:MeOH ratio of 0.267. The CZA catalyst produced no detectable methane at this temperature, with all the non-MeOH product of this catalyst being CO. As such, the CZA catalyst exhibited a far superior MeOH productivity to o-Pd/TiO_2.

The o-Pd/TiO_2 catalyst was superior to the n-Pd/TiO_2. This was to be expected, given the greater Pd loading of the catalyst prepared at optimal pH during the SEA procedure. Both CO_2 conversion and MeOH selectivity were greater with the optimised sample compared with the native sample at all temperatures tested. In fact, the CO_2 conversion over the optimised pH catalysts was, in all cases, almost double that of the Pd/TiO_2 catalyst prepared at native pH.

At all temperatures, the selectivity towards methanol was greater over the optimised pH catalyst than the native pH catalyst. In addition, the methane:MeOH ratio was greater over the native pH sample than the optimised pH catalyst. This may be due to the lower loading of Pd in the native pH catalyst. Exposed TiO_2 is known to facilitate methane formation.[252] Since the native pH catalyst had greater quantities of exposed TiO_2 due to a lower loading, the methane:MeOH ratio was higher than that of the optimised pH catalyst.

As temperature increased, the formation of methane over both the o-Pd/TiO_2 and n-Pd/TiO_2 catalyst increased. At 230 °C, the methane:MeOH ratios were 0.267 and

0.327 for the optimised and native pH catalysts respectively. At 250 °C these values increased to 0.478 and 0.588. At 270 °C, these values further increased to 1.10 and 1.25 respectively, thus at this temperature the selectivity towards methane actually exceeded that of methanol. Accordingly, selectivity towards methanol trended downwards with these catalysts as temperature increased.

With o-Pd/TiO_2 and n-Pd/TiO_2, since CO_2 conversion trended upwards with temperature, albeit lower conversions with the n-Pd/TiO_2 catalysts, and MeOH selectivity trended downwards with temperature, the temperature of maximum MeOH productivity was 250 °C. For the optimised and native pH catalysts, these values were 540 and 414 $mmol_{MeOH}\ kg_{cat}^{-1}\ h^{-1}$ respectively.

At 230 °C, both BMNP catalysts performed worse overall than the MMNP catalysts in terms of MeOH productivity. This was due to far lower CO_2 conversions over these catalysts than the MMNP catalysts. With Pd/ZnO/TiO_2, the CO_2 conversion was merely 2.2%, little more than a fifth the conversion over o-Pd/TiO_2. However, the presence of Zn proved extremely successful in suppressing the formation of methane. At all temperatures, only trace quantities of methane were produced over the BMNP catalysts. The reason given for this was the high loadings of Zn blocking the TiO_2 from facilitating methane formation. Another possibility is there was significant ZnO coverage of TiO_2, suggesting a mode of ZnO growth greater resembling Stranski-Krastanov than Wolmer-Weber.

In addition to the far lower selectivity towards methane, MeOH selectivities also increased significantly. While the MMNP catalysts exhibited MeOH selectivity in the range of 5-12%, the BMNP catalysts exhibited MeOH selectivities in the range of 20-25%. This shows that in addition to methane suppression, these catalysts were better able to compete with the RWGSR, likely due to the synergistic effects of the two metals.

Although the BMNP catalysts exhibited low CO_2 conversion at 230 °C, CO_2 conversion trended upwards with temperature. Conversion values at 230 °C for Pd/ZnO/TiO_2 and ZnO/Pd/TiO_2 were 2.2 and 3.5% respectively. At 250 °C, these values were 4.3 and 5.7% respectively. At 270 °C, these values were 8.7 and 8.8% respectively. However, although these conversions failed to match those of the o-Pd/TiO_2 catalyst at 15.3%, the higher selectivity towards MeOH made for a greater MeOH productivity than the

MMNP catalyst. Owing to the increase in CO_2 conversion without much change in the selectivities of the BMNP catalysts with temperature, the highest MeOH productivities in both BMNP catalysts was reached at 270 °C. This was in contrast to the MMNP catalysts, which reached maximum MeOH productivity at 250 °C.

Overall, amongst the MMNP and BMNP catalysts tested, ZnO/Pd/TiO_2 at 270 °C exhibited the greatest MeOH productivity, at 683 $mmol_{MeOH}$ kg_{cat}^{-1} h^{-1}. The superiority of ZnO/Pd/TiO_2 over Pd/ZnO/TiO_2 has been attributed to the greater Pd loading of this catalyst increasing CO_2 conversion, as well as the greater MeOH selectivities seen in this catalyst.

Despite the success in proving the superiority of BMNP over MMNP catalysts, all catalysts prepared via SEA or CVI-SEA combinations failed to even come close to the MeOH productivity of CZA. SEA-prepared MMNP and BMNP catalysts exhibited 30 to 100 times lower MeOH productivity than CZA. CZA at 230 °C exhibited exquisite MeOH selectivity, albeit lower CO_2 conversion. MeOH selectivity decreased with temperature over CZA, however, CO_2 conversion increased. As such, the maximal MeOH productivity, with a value of greater than 15,000 $mmol_{MeOH}$ kg_{cat}^{-1} h^{-1}, was achieved at 250 °C.

The low activities of the MMNP and BMNP catalysts in comparison to CZA could be attributed to the low Pd loadings present. In o-Pd/TiO_2, Pd loadings were proven both theoretically and experimentally to be in the range of 0.5-0.6wt.%. The loading in n-Pd/TiO_2 was even lower. Pd-based catalysts for the CO_2 hydrogenation reaction in literature typically consist of much greater loadings ca. 2-5wt.%.[252–257] As such, a greater Pd loading would likely prove beneficial for catalytic performance. Although performance was improved with Zn incorporation due to improving MeOH selectivity and suppressing methane formation, low Pd loadings still proved to result in low overall MeOH productivity rates in comparison to CZA.

3.6 Methodical Evaluation

The main scope of the experimental work for this project was to investigate the viability of the SEA method in synthesis of multimetallic nanoparticles for CO_2 hydrogenation to methanol. This section will provide an evaluation on this method and its viability for this application.

3.6.1 Precursor Sourcing

Experimentally, the main challenge to overcome is precursor speciation at high and low pH. Specifically, reactions of precursors with acids and bases used to adjust the pH of solutions to a range of values between 1 and 13 to form precipitates. Since the metal precursors must exist as a stable complex, many metals do not have readily commercially available precursors. For low-PZC supports, the tetraammine (TA) complex is typically used, but only a small range of TA salts are available commercially, including PdTA, PtTA, and RuTA. For metals such as Zn, Cu, Au, Ga, ammine complexes are not readily available. As previously discussed, synthesis of ZnTA through reported methods could not be reproduced despite several attempts with varying conditions, and as such SEA could not be used for Zn incorporation at all.

For elements such as Au, there is no readily available cationic complex for a low PZC support. Where Au has been incorporated into an SEA synthesis on a low-PZC support, $[Au(en)_2]Cl_3$ could be used.[258] However, this complex is not readily available and must be synthesised, adding an additional step. This is not an issue with a high-PZC support, since $HAuCl_4$ is readily available as an anionic Au precursor.

3.6.2 Quantity of Resources Used

In a seq-SEA procedure, with each metal that is added, repeats of PZC experiments are required in order to gain information on the new supporting material surface. For instance, Pd/TiO_2 was proven to have a vastly different PZC to TiO_2. For any PZC or uptake survey, new BET and TPR data is required as well. In addition to the additional time required for these additional experiments, a large quantity of material must be synthesised in order to obtain PZC, BET, uptake survey, and TPR information for each step. Even when minimising volumes to the point where the pH probe is only just submerged, more than six grams of Pd/TiO_2 would required to be synthesised to fulfil PZC and uptake surveys alone.

If this were to be expanded to a trimetallic system, six grams of bimetallic supported nanoparticles would need to be synthesised to run these tests. Additional material would need to be synthesised for any scaled-up impregnations. Given limitations of facilities, in particular tube furnaces for reduction stages, producing the required large quantities of material quickly becomes impractical. For these reasons, synthesis of a core@shell BMNP or TMNP through the use of seq-SEA would prove difficult. In

addition, as reported by Regalbuto, several repeats of the SEA procedure are usually required to obtain full formation of the shell.

The drawbacks of the large quantity of materials required is the high volume of waste that is produced. For PZC and uptake surveys, solutions must be made for every pH value tested, producing a large quantity of both solid and liquid waste. In addition to waste, the high quantity of resources also increases the costs of the procedure.

Time is also an important factor to consider. Obtaining the required information takes a lot of laboratory time, resulting in fewer formulations being tested in a given time period. As such, fewer catalysts can be tested in a given time period.

3.6.3 pH Measurement Accuracy and pH Shifts

Further challenges arose with pH measurements. For the purpose of both PZC and uptake surveys, pH values between 1 and 13 were required. Given the reliance of SEA data on pH values, accuracy of these values was of great importance. However, pH values in the mildly acidic range (pH 5-7) were often inaccurate. For instance, a 10-fold dilution of a pH 4 solution should result in a pH of 5. However, consistently throughout all experiments, a pH value of approximately 6.5 was displayed, with slow but constant drifting downwards. This was the case with all pH probes in the laboratory, and occurred even immediately after probe recalibration. This made PZC testing and uptake surveys within the weakly acidic range greatly challenging and time consuming to obtain an accurate reading. However, in most cases with PZC testing, a sufficiently high loading meant the pH range of the final pH plateau was wide enough such that initial pH values lower than 4 still resulted in a pH shift to the PZC.

In addition, pH values above 12 were inaccurate due to alkaline error, in which Na^+ concentrations were sufficiently high and H^+ concentrations low that the electrode within the probe was responding to Na^+ and giving a false, slightly lower reading than expected.[259] Solutions that were prepared as pH 13, such as 0.1 M NaOH, often read as 12.6-12.7. However, since optimal pH values for low-PZC supports were around 11, this did not significantly impact the accuracy of the initial and final pH values taken as the optimal value in uptake surveys.

The main source of inaccuracy and inconsistency with pH measurements was the pH shift, defined as the change in pH once the supporting material was added. Although this could be approximately anticipated by running a simple experiment, pH shifting

was often inconsistent and highly unpredictable. For instance, in one experiment, a solution with initial pH of 11.80, following addition of a 500 m^2 L^{-1} loading of TiO_2, shifted to a final pH of 11.05. In a repeat experiment with these same conditions, the pH shifted to a final value of 11.30. In a third repeat of the experiment, pH shifted to a final value of 11.45.

The inconsistent pH shifting proved a major challenge experimentally. In uptake surveys, uptake is measured against the final pH value. Since fine final pH values were required to gain crucial information on the optimal pH value, the inaccuracies and inconsistencies associated with anticipating the pH shift severely limited this ability. Since final pH value could not be measured until after the experiment, in which large quantities of resources had been used, large gaps between final pH values often occurred. This often resulted in repeat uptake surveys having to be carried out, requiring more resources and time.

Inconsistent pH shifts also presented as an issue in scaled-up impregnations, in which initial pH values did not always result in the desired final pH that was at or close to the determined optimal value. This was a significant issue. As previously proven, pH values removed from the optimum in an impregnation resulted in a lower metal loading, thus reducing catalytic performance in the CO_2 hydrogenation reaction. In a multimetallic system, this would make obtaining a highly accurate and controlled metal stoichiometry impossible.

Overall, the inconsistent pH shifting from initial to final pH that occurred significantly hampered control over the product; control, which, as previously discussed, is paramount in catalyst design. As such, although the idea of SEA is a rational synthesis, the actual feasibility of this as a rational method has been called into question.

3.6.4 Metal Loading

Catalytic data showed how SEA-prepared catalysts showed low activity compared to CZA, even when combined with CVI. As previously discussed, the SEA method produced catalysts with low metal loadings. For Pd/TiO_2, this was in the 0.5-0.6 wt.% range. As previously discussed, this limit appeared inherent to the supporting material, as governed by the retention of two hydration sheaths. Literature reports of using multimetallic MNPs for CO_2 hydrogenation, particularly Pd-based catalysts, exhibit metal loadings of 5 wt.% as previously discussed.

High metal loadings of around 5 wt.% are required for high catalytic activity for the CO_2 hydrogenation reaction, and this SEA procedure produced low loading catalysts far below 1 wt.%, insufficient for this application. CZA has a Cu loading of 60 wt.%, 100 times the Pd loading achieved via SEA, contributing to its industrial success.

Regalbuto's paper on PdPt BMNP synthesis[214] suggested that loadings in the range 1-4 wt.% Pd and 3-11 wt.% Pt could be obtained on supports such as SiO_2, Al_2O_3, and C, but this remains to be tested.

3.6.5 Final Verdict

Overall, given the difficulty in sourcing or synthesising pH-stable precursors for many metals other than a select few, the high quantity of resources, costs, and high volume of waste, difficulties with anticipating pH shift to predict crucial final pH values, the low loadings of metal and the ultimate low activity of the catalysts produced, the SEA method was deemed not viable for the synthesis of multimetallic nanoparticles for the hydrogenation of CO_2 to methanol.

3.7 Future Prospects

Future experimental prospects would first evaluate Pd loadings when SEA would be carried out on other supporting materials such as Al_2O_3 or SiO_2 gel, which exhibit a greater surface area than TiO_2. If these supports exhibited greater Pd loading up to the 4 wt.% suggested in Regalbuto's publication, adsorption methods could be reconsidered for CO_2 hydrogenation to methanol. However, even if SEA could be used to produce sufficiently high metal loadings, the other challenges with the method still apply. This would particularly present challenges if expansion to TMNPs were considered.

More information could be gained on the $PdZn/TiO_2$ catalysts. Specifically, more conclusive information on β-PdZn alloying could be investigated using elemental mapping. The role of Zn in the suppression of methane formation could be assessed with regards to the reaction mechanism of CO_2 hydrogenation. Specifically, if the ZnO islands suppressed methane formation, or if Pd-Zn nanoparticles played a role.

The natural progression from here would have been expansion from BMNP to TMNPs, staying with Pd and Zn as the first two metals. Addition of a range of third metals could

be tested, such as Au, Ga, Co, Ru and Cu, which have all proven significant in CO_2 hydrogenation reactions.[28,260–263]

Given the difficulties in sourcing viable precursors and the volume of resources and time required to test an array of catalysts, in addition to the unpredictability of pH shifting, the SEA method would likely become disregarded for this application. Alternative methods that were discussed in the introduction chapter, such as galvanic replacement, sequential CVI, or colloidal methods could have been investigated instead. This would therefore allow for not only testing a wide array of third metals, but also a wide array of ratios between the three metals.

Future experiments could have provided not only more catalytic data, but more characterisation, such as DRIFTS to determine metal dispersion on the supporting material, high-resolution EDX mapping to determine nanoparticle structure, and analysis on particle size changes before and after a reaction to check for sintering. Reusability studies should also be carried out, determining the number of reaction cycles the catalyst retains activity for.

Overall, future experiments would shift the scope of the experiment away from SEA and more towards synthesis and testing of TMNP catalysts using different methods better suited to TMNP synthesis and CO_2 hydrogenation to methanol, and evaluating the viability of these methods against the main criteria for catalyst design: producing a highly active catalyst using as little material and resources as possible.

4 Conclusion

The SEA method was successfully used to synthesise samples of Pd/TiO_2, a supported MMNP catalyst with a low loading of 0.6 wt.%, and small particle sizes of below 5 nm. Proof-of-concept experiments also confirmed simultaneous uptake of Pd and PtTA onto TiO_2 was possible, allowing SEA to be used to synthesise BMNP catalysts, too. However, attempts to apply SEA to include Zn in the formulation proved unsuccessful due to the instability of readily available Zn precursors at high pH values and lack of reproducibility in synthesising a pH-stable Zn precursor.

Upon combination of SEA with another method, CVI, Zn was successfully incorporated as a second metal. CVI was carried out to form ZnO/TiO_2, followed by SEA to form a $Pd/ZnO/TiO_2$ BMNP catalyst. However, due to the low uptake of Pd onto ZnO/TiO_2, Pd loadings were found to be very low, at around 0.3 wt.%. Particle sizes were below 5 nm, and the metals were not alloyed.

In order to increase the Pd loading, $ZnO/Pd/TiO_2$ was prepared, where the CVI and SEA steps were reversed. This catalyst was proven to have greater Pd loading. However, the presence or absence of a β-PdZn alloy formation was inconclusive.

When these catalysts were applied to the CO_2 hydrogenation reaction to methanol, the benefits of a second metal were highly apparent. MMNP catalysts showed lower activity and far lower selectivity towards methanol than the BMNP catalysts for all temperatures other than 230 °C. Importantly, MMNP catalysts produced a high quantity of methane, and inferior CO_2 conversion. BMNP catalysts suppressed the formation of methane due to the presence of Zn and the ZnO layer, with almost no methane detectable and superior CO_2 conversions.

Of the BMNP catalysts, $ZnO/Pd/TiO_2$ proved superior in both methanol productivity and methanol selectivity, owing to the greater Pd loading and potential alloying of Pd and Zn. Overall, the most active catalyst was $ZnO/Pd/TiO_2$ at 270 °C.

However, the activity of the most active catalyst was still far lower than the activity of the industrial catalyst for this reaction, CZA. This was potentially due to the low Pd loading of 0.6wt.% afforded by the SEA procedure. This loading was not sufficient to produce an effective catalyst but was proven to be the highest practically achievable loading of Pd on TiO_2 due to the retention of two hydration sheaths. Additional

challenges with the SEA procedure involved lack of predictability with pH shift after the supporting material was added, and the high volume of resources and time required in order to gain the information necessary to carry out the procedure.

In conclusion, while SEA may be useful and applicable for other industrially important reactions such as the ORR, other synthetic procedures would be better suited for BMNP catalysts for the CO_2 hydrogenation reaction, especially if TiO_2 is to be used as the supporting material, or TMNP catalysts are to be considered. These could include galvanic replacement or CVI. These procedures use far fewer resources, produce higher metal loadings on TiO_2, and can be more readily expanded to the synthesis of supported multimetallic nanoparticles as catalysts.

5 References

1 X. Wang, S.-I. Choi, L. T. Roling, M. Luo, C. Ma, L. Zhang, M. Chi, J. Liu, Z. Xie, J. A. Herron, M. Mavrikakis and Y. Xia, *Nat Commun*, 2015, **6**, 7594.

2 S. I. Sinar Mashuri, Ts. Dr. U. Rashid, Y. H. Taufiq-Yap, M. L. Ibrahim, A. Islam, M. F. Kasim, M. S. Mastuli and N. Mijan, *Catalysts*, 2020, **10**, 1260.

3 M. Monai, M. Melchionna and P. Fornasiero, in *Advances in Catalysis*, ed. C. Song, Academic Press, 2018, vol. 63, pp. 1–73.

4 M. Kamalzare, in *Heterogeneous Micro and Nanoscale Composites for the Catalysis of Organic Reactions*, ed. A. Maleki, Elsevier, 2022, pp. 149–165.

5 *Describe the steps in the catalytic hydrogenation of ethylene*, 2003, https://homework.study.com/explanation/describe-the-steps-in-the-catalytic-hydrogenation-of-ethylene.html, (accessed 25 July 2023).

6 S. Kozuch and J. M. L. Martin, *ACS Catal*, 2012, **2**, 2787–2794.

7 J. W. M. Crawley, I. E. Gow, N. Lawes, I. Kowalec, L. Kabalan, C. R. A. Catlow, A. J. Logsdail, S. H. Taylor, N. F. Dummer and G. J. Hutchings, *Chem Rev*, 2022, **122**, 6795–6849.

8 S. Szunerits and R. Boukherroub, in *Encyclopedia of Interfacial Chemistry*, ed. K. Wandelt, Elsevier, Oxford, 2018, pp. 500–510.

9 S. Mohan Bhagyaraj and O. S. Oluwafemi, in *Synthesis of Inorganic Nanomaterials*, eds. S. Mohan Bhagyaraj, O. S. Oluwafemi, N. Kalarikkal and S. Thomas, Woodhead Publishing, 2018, pp. 1–18.

10 V. v Mody, R. C. Siwale, A. V. Singh and H. R. Mody, *J Pharm Bioallied Sci*, 2010, **2**, 282–289.

11 W. H. Qi, M. P. Wang and Q. H. Liu, *J Mater Sci*, 2005, **40**, 2737–2739.

12 K. H. R. Rouwenhorst, O. Elishav, B. Mosevitzky Lis, G. S. Grader, C. Mounaïm-Rousselle, A. Roldan and A. Valera-Medina, in *Techno-Economic Challenges of Green Ammonia as an Energy Vector*, eds. A. Valera-Medina and R. Banares-Alcantara, Academic Press, 2021, pp. 303–319.

13 W. Weiss and W. Ranke, *Prog Surf Sci*, 2002, **70**, 1–151.

14 G. A. Somorjai and J. Y. Park, *Top Catal*, 2008, **49**, 126–135.

15 H. Miyamura and S. Kobayashi, *Angewandte Chemie International Edition*, 2022, **61**, e202201203.

16 N. J. S. Costa and L. M. Rossi, *Nanoscale*, 2012, **4**, 5826–5834.

17 J. D. Scholten, B. C. Leal and J. Dupont, *ACS Catal*, 2012, **2**, 184–200.

18 A. Gual, C. Godard, S. Castillón and C. Claver, *Dalton Transactions*, 2010, **39**, 11499–11512.

19 Y. Zhu and F. Zaera, *Catal Sci Technol*, 2014, **4**, 955–962.

20 B. Roldan Cuenya, *Acc Chem Res*, 2013, **46**, 1682–1691.

21 M. M. Telkar, C. V Rode, R. V Chaudhari, S. S. Joshi and A. M. Nalawade, *Appl Catal A Gen*, 2004, **273**, 11–19.

22 N. Yan, C. Xiao and Y. Kou, *Coord Chem Rev*, 2010, **254**, 1179–1218.

23 G. S. Fonseca, A. P. Umpierre, P. F. P. Fichtner, S. R. Teixeira and J. Dupont, *Chemistry – A European Journal*, 2003, **9**, 3263–3269.

24 C. Wang, R. Ciganda, L. Salmon, D. Gregurec, J. Irigoyen, S. Moya, J. Ruiz and D. Astruc, *Angewandte Chemie International Edition*, 2016, **55**, 3091–3095.

25 M. J. Ndolomingo, N. Bingwa and R. Meijboom, *J Mater Sci*, 2020, **55**, 6195–6241.

26 A. S. Nagpure, P. Gogoi, N. Lucas and S. V Chilukuri, *Sustain Energy Fuels*, 2020, **4**, 3654–3667.

27 H. Zou, J. Dai, J. Suo, R. Ettelaie, Y. Li, N. Xue, R. Wang and H. Yang, *Nat Commun*, 2021, **12**, 4968.

28 V. Iablokov, S. K. Beaumont, S. Alayoglu, V. V Pushkarev, C. Specht, J. Gao, A. P. Alivisatos, N. Kruse and G. A. Somorjai, *Nano Lett*, 2012, **12**, 3091–3096.

29 T. Mitsudome and K. Kaneda, *Green Chemistry*, 2013, **15**, 2636–2654.

30 J. Pang, M. Zheng, C. Wang, X. Yang, H. Liu, X. Liu, J. Sun, Y. Wang and T. Zhang, *ACS Catal*, 2020, **10**, 13624–13629.

31 Y. Huang, B. Wang, H. Yuan, Y. Sun, D. Yang, X. Cui and F. Shi, *Catal Sci Technol*, 2021, **11**, 1652–1664.

32 S.-J. Li, Y.-T. Zhou, X. Kang, D.-X. Liu, L. Gu, Q.-H. Zhang, J.-M. Yan and Q. Jiang, *Advanced Materials*, 2019, **31**, 1806781.

33 J. Wu, S. Mallikarjun Sharada, C. Ho, A. W. Hauser, M. Head-Gordon and A. T. Bell, *Appl Catal A Gen*, 2015, **506**, 25–32.

34 H. N. Pham, J. J. H. B. Sattler, B. M. Weckhuysen and A. K. Datye, *ACS Catal*, 2016, **6**, 2257–2264.

35 J. Liu, Y. Yue, H. Liu, Z. Da, C. Liu, A. Ma, J. Rong, D. Su, X. Bao and H. Zheng, *ACS Catal*, 2017, **7**, 3349–3355.

36 Z. Wu, E. C. Wegener, H.-T. Tseng, J. R. Gallagher, J. W. Harris, R. E. Diaz, Y. Ren, F. H. Ribeiro and J. T. Miller, *Catal Sci Technol*, 2016, **6**, 6965–6976.

37 C. Deraedt, R. Ye, W. T. Ralston, F. D. Toste and G. A. Somorjai, *J Am Chem Soc*, 2017, **139**, 18084–18092.

38 Y. Shan, H. Hu, X. Fan and Z. Zhao, *Chem Phys*, 2023, **25**, 18609–18622.

39 P. Ingale, K. Knemeyer, P. Preikschas, M. Ye, M. Geske, R. Naumann d'Alnoncourt, A. Thomas and F. Rosowski, *Catal Sci Technol*, 2021, **11**, 484–493.

40 X. Zhou, Z. Chen, D. Yan and H. Lu, *J Mater Chem*, 2012, **22**, 13506–13516.

41 E.-H. Yuan, Y. Niu, X. Huang, M. Li, J. Bao, Y.-H. Song, B. Zhang, Z.-T. Liu, M.-G. Willinger and Z.-W. Liu, *Journal of Energy Chemistry*, 2023, **80**, 479–491.

42 Z.-P. Hu, Z. Wang and Z.-Y. Yuan, *Molecular Catalysis*, 2020, **493**, 111052.

43 J. Lu, J. W. Elam and P. C. Stair, *Acc Chem Res*, 2013, **46**, 1806–1815.

44 K. Kon, W. Onodera, T. Toyao and K. Shimizu, *Catal Sci Technol*, 2016, **6**, 5864–5870.

45 W. Shen, F. E. Huggins, N. Shah, G. Jacobs, Y. Wang, X. Shi and G. P. Huffman, *Appl Catal A Gen*, 2008, **351**, 102–110.

46 D. Fan, X. Lv, J. Feng, S. Zhang, J. Bai, R. Lu and J. Liu, *Int J Hydrogen Energy*, 2017, **42**, 11312–11320.

47 M. R. Scheide, M. M. Peterle, S. Saba, J. S. S. Neto, G. F. Lenz, R. D. Cezar, J. F. Felix, G. V Botteselle, R. Schneider, J. Rafique and A. L. Braga, *Sci Rep*, 2020, **10**, 15233.

48 W. Wang, D. Wang, H. Song, D. Hao, B. Xu, J. Ren, M. Wang, C. Dai, Y. Wang and W. Liu, *Chem Eng Journal*, 2023, **455**, 140909.

49 K. Mallick, M. Witcomb and M. Scurrell, *Mater Chem Phys*, 2006, **97**, 283–287.

50 R. K. Sharma, P. Sharma and A. Maitra, *J Colloid Interface Sci*, 2003, **265**, 134–140.

51 E. Lorençon, A. S. Ferlauto, S. de Oliveira, D. R. Miquita, R. R. Resende, R. G. Lacerda and L. O. Ladeira, *ACS Appl Mater Interfaces*, 2009, **1**, 2104–2106.

52 K. Zhang, W. Guo, Z. Liang and R. Zou, *Sci China Chem*, 2019, **62**, 417–429.

53 N. C. Bigall, M. Reitzig, W. Naumann, P. Simon, K.-H. van Pée and A. Eychmüller, *Ang Chemie Int Ed*, 2008, **47**, 7876–7879.

54 A. Garcia-Leis, D. Jancura, M. Antalik, J. V Garcia-Ramos, S. Sanchez-Cortes and Z. Jurasekova, *Chem Phys*, 2016, **18**, 26562–26571.

55 Z. Zhang, U. Gernert, R. F. Gerhardt, E.-M. Höhn, D. Belder and J. Kneipp, *ACS Catal*, 2018, **8**, 2443–2449.

56 D. Lyu, Y. Du, S. Huang, B. Y. Mollamahale, X. Zhang, S. W. Hasan, F. Yu, S. Wang, Z. Q. Tian and P. K. Shen, *ACS Appl Mater Interfaces*, 2019, **11**, 39809–39819.

57 Q. Li and S. Sun, *Nano Energy*, 2016, **29**, 178–197.

58 Z.-P. Wu, D. T. Caracciolo, Y. Maswadeh, J. Wen, Z. Kong, S. Shan, J. A. Vargas, S. Yan, E. Hopkins, K. Park, A. Sharma, Y. Ren, V. Petkov, L. Wang and C.-J. Zhong, *Nat Commun*, 2021, **12**, 859.

59 Y. S. Jeong, J.-B. Park, H.-G. Jung, J. Kim, X. Luo, J. Lu, L. Curtiss, K. Amine, Y.-K. Sun, B. Scrosati and Y. J. Lee, *Nano Lett*, 2015, **15**, 4261–4268.

60 Z.-F. Li, Y. Wang and G. G. Botte, *Electrochim Acta*, 2017, **228**, 351–360.

61 O. Movil, M. Garlock and J. A. Staser, *Int J Hydrogen Energy*, 2015, **40**, 4519–4530.

62 J. Kim, H.-E. Kim and H. Lee, *ChemSusChem*, 2018, **11**, 104–113.

63 S. Back, M. S. Yeom and Y. Jung, *ACS Catal*, 2015, **5**, 5089–5096.

64 H.-S. Oh, H. N. Nong, T. Reier, A. Bergmann, M. Gliech, J. Ferreira de Araújo, E. Willinger, R. Schlögl, D. Teschner and P. Strasser, *J Am Chem Soc*, 2016, **138**, 12552–12563.

65 C. Wang and D. Astruc, *Prog Mater Sci*, 2018, **94**, 306–383.

66 M. Liu, F. Hof, M. Moro, G. Valenti, F. Paolucci and A. Pénicaud, *Nanoscale*, 2020, **12**, 20165–20170.

67 Y. Holade, N. Şahin, K. Servat, T. Napporn and K. Kokoh, *Catalysts*, 2015, **2015**, 310–348.

68 S. Kidambi, J. Dai, J. Li and M. L. Bruening, *J Am Chem Soc*, 2004, **126**, 2658–2659.

69 D. Capco and Y. Chen, *Nanomaterial: Impacts on Cell Biology and Medicine*, 2014.

70 R. J. Isaifan, S. Ntais and E. A. Baranova, *Appl Catal A Gen*, 2013, **464–465**, 87–94.

71 S. Mostafa, F. Behafarid, J. R. Croy, L. K. Ono, L. Li, J. C. Yang, A. I. Frenkel and B. R. Cuenya, *J Am Chem Soc*, 2010, **132**, 15714–15719.

72 S. Cao, F. (Feng) Tao, Y. Tang, Y. Li and J. Yu, *Chem Soc Rev*, 2016, **45**, 4747–4765.

73 K. M. Bratlie, H. Lee, K. Komvopoulos, P. Yang and G. A. Somorjai, *Nano Lett*, 2007, **7**, 3097–3101.

74 C. T. Campbell, *Acc Chem Res*, 2013, **46**, 1712–1719.

75 B. Vanrenterghem, B. Geboes, S. Bals, J. Ustarroz, A. Hubin and T. Breugelmans, *Appl Catal B*, 2016, **181**, 542–549.

76 M. Shekhar, J. Wang, W.-S. Lee, W. D. Williams, S. M. Kim, E. A. Stach, J. T. Miller, W. N. Delgass and F. H. Ribeiro, *J Am Chem Soc*, 2012, **134**, 4700–4708.

77 P. Serp, *ChemCatChem*, 2023, **15**. doi.org/10.1002/cctc.202300545

78 A. Primo, P. Concepción and A. Corma, *Chem Comm*, 2011, **47**, 3613–3615.

79 J. Croy, S. Mostafa, J. Liu, Y. Sohn, H. Heinrich and B. Roldan Cuenya, *Catal Letters*, 2007, **119**, 209–216.

80 C.-J. Zhong, J. Luo, P. N. Njoki, D. Mott, B. Wanjala, R. Loukrakpam, S. Lim, L. Wang, B. Fang and Z. Xu, *Energy Environ Sci*, 2008, **1**, 454–466.

81 S. D. Lacey, Q. Dong, Z. Huang, J. Luo, H. Xie, Z. Lin, D. J. Kirsch, V. Vattipalli, C. Povinelli, W. Fan, R. Shahbazian-Yassar, D. Wang and L. Hu, *Nano Lett*, 2019, **19**, 5149–5158.

82 X. Sun, D. Li, Y. Ding, W. Zhu, S. Guo, Z. L. Wang and S. Sun, *J Am Chem Soc*, 2014, **136**, 5745–5749.

83 B. N. Wanjala, J. Luo, B. Fang, D. Mott and C.-J. Zhong, *J Mater Chem*, 2011, **21**, 4012–4020.

84 N. A. Beckers, S. Huynh, X. Zhang, E. J. Luber and J. M. Buriak, *ACS Catal*, 2012, **2**, 1524–1534.

85 L. Huang, H. Lin, C. Y. Zheng, E. J. Kluender, R. Golnabi, B. Shen and C. A. Mirkin, *J Am Chem Soc*, 2020, **142**, 4570–4575.

86 J. H. Park and H. S. Ahn, *Appl Surf Sci*, 2020, **504**, 144517.

87 R. Jiang, D. R. Baker, D. T. Tran, J. Li, A. C. Leff and S. S. Zhang, *ACS Appl Nano Mater*, 2020, **3**, 7119–7129.

88 F. Epron, C. Especel, G. Lafaye and P. Marécot, in *Nanoparticles and Catalysis*, 2007, pp. 279–302.

89 P. Qiao, S. Zou, S. Xu, J. Liu, Y. Li, G. Ma, L. Xiao, H. Lou and J. Fan, *J Mater Chem A Mater*, 2014, **2**, 17321–17328.

90 Z. Chen, G. Zhang, H. Chen, J. Prakash, Y. Zheng and S. Sun, *Ren and Sust Energy Rev*, 2022, **155**, 111922.

91 M. S. İzgi, O. Baytar, Ö. Şahin and H. Ç. Kazıcı, *Int J Hydrogen Energy*, 2020, **45**, 34857–34866.

92 P.-C. Chen, X. Liu, J. L. Hedrick, Z. Xie, S. Wang, Q.-Y. Lin, M. C. Hersam, V. P. Dravid and C. A. Mirkin, *Science (1979)*, 2016, **352**, 1565–1569.

93 F. Fan, J. Zhang, J. Li, N. Zhang, R. Hong, X. Deng, P. Tang and D. Li, *Sens Actuators B Chem*, 2017, **241**, 895–903.

94 D. J. Loevlie, B. Ferreira and G. Mpourmpakis, *Acc Chem Res*, 2023, **56**, 248–257.

95 C. Wang, D. van der Vliet, K. L. More, N. J. Zaluzec, S. Peng, S. Sun, H. Daimon, G. Wang, J. Greeley, J. Pearson, A. P. Paulikas, G. Karapetrov, D. Strmcnik, N. M. Markovic and V. R. Stamenkovic, *Nano Lett*, 2011, **11**, 919–926.

96 C. Kim and J. W. Ager, *Nature Synthesis*, DOI:10.1038/s44160-023-00392-6.

97 P. Wu, F. Gong, X. Feng, Y. Xia, L. Xia, T. Kai and P. Ding, *J Nanobiotechnology*, 2023, **21**, 185.

98 D. Mott, J. Luo, P. N. Njoki, Y. Lin, L. Wang and C.-J. Zhong, *Catal Today*, 2007, **122**, 378–385.

99 H. Kim, T. Y. Yoo, M. S. Bootharaju, J. H. Kim, D. Y. Chung and T. Hyeon, *Advanced Science*, 2022, **9**, 2104054.

100 M. Takahashi, H. Koizumi, W.-J. Chun, M. Kori, T. Imaoka and K. Yamamoto, *Sci Adv*, 2023, **3**, 1700101.

101 T. Dang-Bao, D. Pla, I. Favier and M. Gomez, *Catalysts*, DOI:10.3390/catal7070207.

102 N. A. Merrill, T. T. Nitka, E. M. McKee, K. C. Merino, L. F. Drummy, S. Lee, B. Reinhart, Y. Ren, C. J. Munro, S. Pylypenko, A. I. Frenkel, N. M. Bedford and M. R. Knecht, *ACS Appl Mater Interfaces*, 2017, **9**, 8030–8040.

103 J. K. Edwards, J. Pritchard, L. Lu, M. Piccinini, G. Shaw, A. F. Carley, D. J. Morgan, C. J. Kiely and G. J. Hutchings, *Ang Chemie Int Ed*, 2014, **53**, 2381–2384.

104 W. Zhang, in *Nanomaterial: Impacts on Cell Biology and Medicine*, eds. D. G. Capco and Y. Chen, Springer Netherlands, Dordrecht, 2014, pp. 19–43.

105 T. W. Hansen, A. T. DeLaRiva, S. R. Challa and A. K. Datye, *Acc Chem Res*, 2013, **46**, 1720–1730.

106 I. F. Cruz, C. Freire, J. P. Araújo, C. Pereira and A. M. Pereira, in *Magnetic Nanostructured Materials*, eds. A. A. El-Gendy, J. M. Barandiarán and R. L. Hadimani, Elsevier, 2018, pp. 59–116.

107 G. Vaidyanathan and S. Sendhilnathan, *Physica B Condens Matter*, 2008, **403**, 2157–2167.

108 G. Vaidyanathan, S. Sendhilnathan and R. Arulmurugan, *J Magn Magn Mater*, 2007, **313**, 293–299.

109 K. Maaz, S. Karim, A. Mumtaz, S. K. Hasanain, J. Liu and J. L. Duan, *J Magn Magn Mater*, 2009, **321**, 1838–1842.

110 G. Allaedini, S. Tasirin and P. Aminayi, *Chemical Papers*, DOI:10.1515/chempap-2015-0190.

111 S. Tazikeh, A. Akbari, A. Talebi and E. Talebi, *Materials Science-Poland*, 2014, **32**, 98–101.

112 K. Petcharoen and A. Sirivat, *Materials Science and Engineering: B*, 2012, **177**, 421–427.

113 B. Wang, Q. Wei and S. Qu, *Int J Electrochem Sci*, 2013, **8**, 3786–3793.

114 Q. Yang, Q. Xu and H.-L. Jiang, *Chem Soc Rev*, 2017, **46**, 4774–4808.

115 L. Delannoy, N. el Hassan, A. Musi, N. N. le To, J.-M. Krafft and C. Louis, *J Phys Chem B*, 2006, **110**, 22471–22478.

116 C. A. Boasiako, Z. Zhou, X. Huo and T. Ye, *J Hazard Mater*, 2023, **446**, 130661.

117 Y. Zhang, L. Zhong, H. Wang, P. Gao, X. Li, S. Xiao, G. Ding, W. Wei and Y. Sun, *Journal of CO_2 Utilization*, 2016, **15**, 72–82.

118 S. J. Freakley, Q. He, C. J. Kiely and G. J. Hutchings, *Catal Letters*, 2015, **145**, 71–79.

119 N. Santhanam, T. A. Conforti, W. Spieker and J. R. Regalbuto, *Catal Today*, 1994, **21**, 141–156.

120 J. A. Mendoza-Nieto, O. Vera-Vallejo, L. Escobar-Alarcón, D. Solís-Casados and T. Klimova, *Fuel*, 2013, **110**, 268–277.

121 M. Yurderi, A. Bulut, M. Zahmakiran and M. Kaya, *Appl Catal B*, 2014, **160–161**, 514–524.

122 Y. Nakaya, M. Miyazaki, S. Yamazoe, K. Shimizu and S. Furukawa, *ACS Catal*, 2020, **10**, 5163–5172.

123 Q. He, P. J. Miedziak, L. Kesavan, N. Dimitratos, M. Sankar, J. A. Lopez-Sanchez, M. M. Forde, J. K. Edwards, D. W. Knight, S. H. Taylor, C. J. Kiely and G. J. Hutchings, *Faraday Discuss*, 2013, **162**, 365–378.

124 J. A. Lopez-Sanchez, N. Dimitratos, P. Miedziak, E. Ntainjua, J. K. Edwards, D. Morgan, A. F. Carley, R. Tiruvalam, C. J. Kiely and G. J. Hutchings, *Chem Phys*, 2008, **10**, 1921–1930.

125 H. Bahruji, M. Bowker, G. Hutchings, N. Dimitratos, P. Wells, E. Gibson, W. Jones, C. Brookes, D. Morgan and G. Lalev, *J Catal*, 2016, **343**, 133–146.

126 R. Nain and R. P. Chauhan, *Asian Journal of Chem*, 2009, **21**, S113-116.

127 J. Cookson, *Platin Met Rev*, 2012, **56**, 83–98.

128 A. Kyrychenko, D. A. Pasko and O. N. Kalugin, *Chem Phys*, 2017, **19**, 8742–8756.

129 T. Tsuji, J. Kim, H. Sakakita, Y. Shimizu, G. Chen, K. Hata, D. N. Futaba and S. Sakurai, *ACS Omega*, 2021, **6**, 18763–18769.

130 K. B. Male, J. Li, C. C. Bun, S.-C. Ng and J. H. T. Luong, *Journal of Phys Chem C*, 2008, **112**, 443–451.

131 S. AU - Mozaffari, W. AU - Li, C. AU - Thompson, S. AU - Ivanov, S. AU - Seifert, B. AU - Lee, L. AU - Kovarik and A. M. AU - Karim, *JoVE*, 2018, e57667.

132 S. A. Kondrat, P. J. Miedziak, M. Douthwaite, G. L. Brett, T. E. Davies, D. J. Morgan, J. K. Edwards, D. W. Knight, C. J. Kiely, S. H. Taylor and G. J. Hutchings, *ChemSusChem*, 2014, **7**, 1326–1334.

133 J. Zhao, H. Li, Z. Liu, W. Hu, C. Zhao and D. Shi, *Carbon N Y*, 2015, **87**, 116–127.

134 K. Aranishi, H.-L. Jiang, T. Akita, M. Haruta and Q. Xu, *Nano Res*, 2011, **4**, 1233–1241.

135 S. W. Kang, Y. W. Lee, Y. Park, B.-S. Choi, J. W. Hong, K.-H. Park and S. W. Han, *ACS Nano*, 2013, **7**, 7945–7955.

136 P. Wu, P. Ding, X. Ye, L. Li, X. He and K. Wang, *RSC Adv*, 2019, **9**, 14982–14989.

137 X. Ye, X. He, Y. Lei, J. Tang, Y. Yu, H. Shi and K. Wang, *Chem Comm*, 2019, **55**, 2321–2324.

138 Y. Shi, H. Xu, J. Wang, S. Li, Z. Xiong, B. Yan, C. Wang and Y. Du, *Sens Actuators B Chem*, 2018, **272**, 135–138.

139 P. C. Pandey and G. Pandey, *Catal Sci Technol*, 2016, **6**, 3911–3917.

140 Md. A. Matin, J.-H. Jang and Y.-U. Kwon, *Int J Hydrogen Energy*, 2014, **39**, 3710–3718.

141 F. Fiévet, S. Ammar-Merah, R. Brayner, F. Chau, M. Giraud, F. Mammeri, J. Peron, J.-Y. Piquemal, L. Sicard and G. Viau, *Chem Soc Rev*, 2018, **47**, 5187–5233.

142 B. Sen, B. Demirkan, A. Şavk, S. Karahan Gülbay and F. Sen, *Int J Hydrogen Energy*, 2018, **43**, 17984–17992.

143 H. Bahruji, M. Bowker, W. Jones, J. Hayward, J. Ruiz Esquius, D. J. Morgan and G. J. Hutchings, *Faraday Discuss*, 2017, **197**, 309–324.

144 M. M. Forde, R. D. Armstrong, R. McVicker, P. P. Wells, N. Dimitratos, Q. He, L. Lu, R. L. Jenkins, C. Hammond, J. A. Lopez-Sanchez, C. J. Kiely and G. J. Hutchings, *Chem Sci*, 2014, **5**, 3603–3616.

145 P. Sivakumar, R. Ishak and V. Tricoli, *Electrochim Acta*, 2005, **50**, 3312–3319.

146 K. Oura, V. G. Lifshits, A. A. Saranin, A. V. Zotov and M. Katayama, *Surface Science: An Introduction*, Springer Science & Business Media, 2013.

147 T. K. Gupta, M. S. Goyat, A. Dhyani and R. K. Brajpuriya, in *Ferrite Nanostructured Magnetic Materials*, eds. J. Pal Singh, K. H. Chae, R. C. Srivastava and O. F. Caltun, Woodhead Publishing, 2023, pp. 293–308.

148 A. Yamaguchi, A. Hirohata and B. J. H. Stadler, Eds., in *Nanomagnetic Materials*, Elsevier, 2021, pp. 1–55.

149 K. Oura, M. Katayama, A. V Zotov, V. G. Lifshits and A. A. Saranin, in *Surface Science: An Introduction*, eds. K. Oura, M. Katayama, A. V Zotov, V. G. Lifshits and A. A. Saranin, Springer Berlin Heidelberg, Berlin, Heidelberg, 2003, pp. 357–387.

150 M. Miyazaki, S. Furukawa, T. Takayama, S. Yamazoe and T. Komatsu, *ACS Appl Nano Mater*, 2019, **2**, 3307–3314.

151 X. Wang, S. Chen, G. Reggiano, S. Thota, Y. Wang, P. Kerns, S. L. Suib and J. Zhao, *Chem Comm*, 2019, **55**, 1249–1252.

152 S. Papadimitriou, S. Armyanov, E. Valova, A. Hubin, O. Steenhaut, E. Pavlidou, G. Kokkinidis and S. Sotiropoulos, *The Journal of Physical Chemistry C*, 2010, **114**, 5217–5223.

153 Q. Li, P. Xu, B. Zhang, G. Wu, H. Zhao, E. Fu and H.-L. Wang, *Nanoscale*, 2013, **5**, 7397–7402.

154 A. G. M. da Silva, T. S. Rodrigues, S. J. Haigh and P. H. C. Camargo, *Chem Comm*, 2017, **53**, 7135–7148.

155 J. M. Lowe and R. H. Coridan, *Nanoscale Adv*, 2019, **1**, 1343–1350.

156 F. Xhelo, J. Patarroyo, L. Russo, J. Piella, A. Genç, J. Arbiol, N. Bastús and V. Puntes, *Mater Today Adv*, , DOI:10.1016/j.mtadv.2019.100037.

157 A. Papaderakis, I. Mintsouli, J. Georgieva and S. Sotiropoulos, *Catalysts*, 2017, **7**, 80.

158 D.-Y. Wang, H.-L. Chou, Y.-C. Lin, F.-J. Lai, C.-H. Chen, J.-F. Lee, B.-J. Hwang and C.-C. Chen, *J Am Chem Soc*, 2012, **134**, 10011–10020.

159 J. I. Patarroyo Rengifo, Exploring Synthetic Strategies for the Production of Complex Inorganic Nanoparticles. Doctoral Thesis, Universitat Autonoma de Barcelona, 2018.

160 H.-J. Yin, Z.-P. Zhang, Y. Guo, K. Yuan and Y.-W. Zhang, *Mater Chem Front*, 2020.

161 L. S. R. Kumara, O. Sakata, S. Kohara, A. Yang, C. Song, K. Kusada, H. Kobayashi and H. Kitagawa, *Chem Phys*, 2016, **18**, 30622–30629.

162 C. Zhu, S. Guo and S. Dong, *J. Mater. Chem.*, 2012, **22**, 14851–14855.

163 F. Muench, *ChemElectroChem*, 2021, **8**, 2993–3012.

164 R. Sen, T. M. Gordon, S. L. Millheim, J. H. Smith, X. Y. Gan and J. E. Millstone, *Nanoscale*, 2023, **15**, 6655–6663.

165 A. A. Ashkarran, *Current Applied Physics – Curr Appl Phys*, 2010, **10**, 1442–1447.

166 P.-C. Chen, G. Liu, Y. Zhou, K. A. Brown, N. Chernyak, J. L. Hedrick, S. He, Z. Xie, Q.-Y. Lin, V. P. Dravid, S. A. O'Neill-Slawecki and C. A. Mirkin, *J Am Chem Soc*, 2015, **137**, 9167–9173.

167 M. Nguyen and T. Yonezawa, *Sci Technol Adv Mater*, 2018, **19**, 883–898.

168 EASAC, *Decarbonisation of Transport: options and challenges*, 2019, ISBN: 978-3-8047-3977-2. (Accessed September 14, 2023).

169 J. Sa, *Fuel Production with Heterogeneous Catalysis*, CRC Press, 1st edn., 2018.

170 B. R. Cuenya, *Thin Solid Films*, 2010, **518**, 3127–3150.

171 A. Karelovic, G. Galdames, J. C. Medina, C. Yévenes, Y. Barra and R. Jiménez, *J Catal*, 2019, **369**, 415–426.

172 A. Karelovic and P. Ruiz, *Catal Sci Technol*, 2015, **5**, 869–881.

173 M. Pori, I. Arčon, V. D. B. C. Dasireddy, B. Likozar, Z. C. Orel and M. Marinšek, *Catal Letters*, 2021, **151**, 3114–3134.

174 J. Díez-Ramírez, J. A. Díaz, P. Sánchez and F. Dorado, *Journal of CO2 Utilization*, 2017, **22**, 71–80.

175 M. S. Duyar, A. Gallo, J. L. Snider and T. F. Jaramillo, *Journal of CO_2 Utilization*, 2020, **39**, 101151.

176 S. Zhao, Z. Zhao, K. Yao and H. Liu, *Comput Theor Chem*, 2020, **1178**, 112783.

177 T. E. L. Smitshuysen, M. R. Nielsen, T. Pruessmann, A. Zimina, T. L. Sheppard, J.-D. Grunwaldt, I. Chorkendorff and C. D. Damsgaard, *ChemCatChem*, 2020, **12**, 3265–3273.

178 M. Bowker, N. Lawes, I. Gow, J. Hayward, J. R. Esquius, N. Richards, L. R. Smith, T. J. A. Slater, T. E. Davies, N. F. Dummer, L. Kabalan, A. Logsdail, R. C. Catlow, S. Taylor and G. J. Hutchings, *ACS Catal*, 2022, **12**, 5371–5379.

179 J. Su and J.-S. Chen, *Micro Meso Mat*, 2017, **237**, 246–259.

180 Z. Yan, L. Lin and S. Liu, *Energy & Fuels*, 2009, **23**, 3853–3858.

181 T. Maegawa, A. Akashi, K. Yaguchi, Y. Iwasaki, M. Shigetsura, Y. Monguchi and H. Sajiki, *Chemistry – A European Journal*, 2009, **15**, 6953–6963.

182 P. Gallezot, P. J. Cerino, B. Blanc, G. Flèche and P. Fuertes, *J Catal*, 1994, **146**, 93–102.

183 H. Lindlar and R. Dubuis, Org. Synth. 1966, **46**, 89. DOI: 10.15227/orgsyn.046.0089

184 V. R. Surisetty, A. K. Dalai and J. Kozinski, *Ind Eng Chem Res*, 2010, **49**, 6956–6963.

185 H. Schulz, *Appl Catal A Gen*, 1999, **186**, 3–12.

186 M. A. Vannice, *J Catal*, 1975, **37**, 449–461.

187 S. Badoga, G. Kamath and A. Dalai, *Appl Catal A Gen*, 2020, **607**, 117861.

188 P. Breeze, in *Power System Energy Storage Technologies*, ed. P. Breeze, Academic Press, 2018, pp. 69–77.

189 M. Younas, M. Rezakazemi, M. S. Arbab, J. Shah and W. U. Rehman, *Int J Hydrogen Energy*, 2022, **47**, 11694–11724.

190 D. Harrison, E. Welchman and T. Thonhauser, *Int J Hydrogen Energy*, 2017, **42**, 2223–2228.

191 T. Hügle, M. F. Kühnel and D. Lentz, *J Am Chem Soc*, 2009, **131**, 7444–7446.

192 S. Akbayrak and S. Özkar, *Int J Hydrogen Energy*, 2018, **43**, 18592–18606.

193 Y. Wu, D. Wang, X. Chen, G. Zhou, R. Yu and Y. Li, *J Am Chem Soc*, 2013, **135**, 12220–12223.

194 C. H. Campos, K. Shanmugaraj, T. M. Bustamante, E. Leal-Villarroel, V. Vinoth, R. Aepuru, R. V. Mangalaraja and C. C. Torres, *Catal Today*, 2022, **394–396**, 510–523.

195 S. Dahl, A. Logadottir, R. C. Egeberg, J. H. Larsen, I. Chorkendorff, E. Törnqvist and J. K. Nørskov, *Phys Rev Lett*, 1999, **83**, 1814–1817.

196 J. Yang and J. Y. Ying, *Ang Chemie Int Ed*, 2011, **50**, 4637–4643.

197 Z. Khan, *Int J Hydrogen Energy*, 2019, **44**, 11503–11513.

198 B. Peng and J. Chen, *Energy Environ Sci*, 2008, **1**, 479–483.

199 L.-L. Fu, D.-F. Zhang, Z. Yang, T.-W. Chen and J. Zhai, *ACS Sustain Chem Eng*, 2020, **8**, 3734–3742.

200 N. Cao, J. Su, W. Luo and G. Cheng, *Catal Commun*, 2014, **43**, 47–51.

201 V. P. Zhdanov, *J Chem Phys*, 2015, **143**, 166102.

202 G. J. Hutchings, *Catal Today*, 2014, **238**, 69–73.

203 P. Haider, B. Kimmerle, F. Krumeich, W. Kleist, J.-D. Grunwaldt and A. Baiker, *Catal Letters*, 2008, **125**, 169–176.

204 A. Abad, P. Concepción, A. Corma and H. García, *Ang Chemie Int Ed*, 2005, **44**, 4066–4069.

205 M. Sankar, N. Dimitratos, D. W. Knight, A. F. Carley, R. Tiruvalam, C. J. Kiely, D. Thomas and G. J. Hutchings, *ChemSusChem*, 2009, **2**, 1145–1151.

206 H. Zhang, M. Okumura and N. Toshima, *Journal of Phys Chem C*, 2011, **115**, 14883–14891.

207 H. Zhang, L. Lu, Y. Cao, S. Du, Z. Cheng and S. Zhang, *Mater Res Bull*, 2014, **49**, 393–398.

208 L. Wang, L. Yang, Y. Zhang, W. Ding, S. Chen, W. Fang and Y. Yang, *Fuel Processing Technology*, 2010, **91**, 723–728.

209 D. Andreeva, V. Idakiev, T. Tabakova, L. Ilieva, P. Falaras, A. Bourlinos and A. Travlos, *Catal Today*, 2002, **72**, 51–57.

210 J. T. Kummer, *J Phys Chem*, 1986, **90**, 4747–4752.

211 M. Haruta, T. Kobayashi, H. Sano and N. Yamada, *Chem Lett*, 1987, **16**, 405–408.

212 L. Yang, S. Shan, R. Loukrakpam, V. Petkov, Y. Ren, B. N. Wanjala, M. H. Engelhard, J. Luo, J. Yin, Y. Chen and C.-J. Zhong, *J Am Chem Soc*, 2012, **134**, 15048–15060.

213 A. Tripathi, C. Hareesh, S. Sinthika, G. Andersson and R. Thapa, *Appl Surf Sci*, 2020, **528**, 146964.

214 H.-R. Cho and J. R. Regalbuto, *Catal Today*, 2015, **246**, 143–153.

215 H. P. Boehm, *Discuss Faraday Soc*, 1971, **52**, 264–275.

216 J. Chorover, in *Encyclopedia of Soils in the Environment (Second Edition)*, eds. M. J. Goss and M. Oliver, Academic Press, Oxford, 2023, pp. 368–375.

217 J. Regalbuto, in *Catalyst Preparation: Science and Engineering*, ed. J. Regalbuto, CRC Press, 1st edn., 2007, pp. 297–318.

218 Y.-P. Qiu, Q. Shi, W.-Z. Wang, S.-H. Xia, H. Dai, H. Yin, Z.-Q. Yang and P. Wang, *Small*, 2022, **18**, 2106143.

219 J. Yang, Y. Fan, Z.-L. Li, Z. Peng, J.-H. Yang, B. Liu and Z. Liu, *Molecular Catalysis*, 2020, **492**, 110992.

220 J. M. Keels, X. Chen, S. Karakalos, C. Liang, J. R. Monnier and J. R. Regalbuto, *ACS Catal*, 2018, **8**, 6486–6494.

221 L. D'Souza and J. R. Regalbuto, in *Studies in Surface Science and Catalysis*, eds. E. M. Gaigneaux, M. Devillers, S. Hermans, P. A. Jacobs, J. A. Martens and P. Ruiz, Elsevier, 2010, vol. 175, pp. 715–718.

222 Y. Ma, A. N. Kuhn, W. Gao, T. Al-Zoubi, H. Du, X. Pan and H. Yang, *Nano Energy*, 2021, **79**, 105465.

223 L. De Castro, D. Sahsah, A. Heyden, J. Regalbuto and C. Williams, *Journal of Phys Chem C*, 2022, **126**, 11111–11128.

224 M. Schreier and J. R. Regalbuto, *J Catal*, 2004, **225**, 190–202.

225 W. A. Spieker, J. Liu, X. Hao, J. T. Miller, A. J. Kropf and J. R. Regalbuto, *Appl Catal A Gen*, 2003, **243**, 53–66.

226 H. K. Farag, *Zeitschrift für Physikalische Chemie*, 2011, **225**, 45–55.

227 C. E. Housecroft and A. G. Sharpe, *Inorganic Chemistry: Fourth Edition*, Pearson, 4th edn., 2012.

228 S. M. Londoño-Restrepo, R. Jeronimo-Cruz, B. M. Millán-Malo, E. M. Rivera-Muñoz and M. E. Rodriguez-García, *Sci Rep*, 2019, **9**, 5915.

229 A. Connelly, BET surface area, https://andyjconnelly.wordpress.com/2017/03/13/bet-surface-area/#:~:text=C%20is%20normally%20between%20100,sample%20may%20contain%20significant%20porosity, (accessed 16 September 2023).

230 V. Kumar, G. Srinivas, B. Wood, K. Ramisetty, A. Stewart, C. Howard, D. J. L. Brett and F. Rodriguez-Reinoso, *J Mater Chem A Mater*, DOI:10.1039/C9TA00287A.

231 M. C. Geisenblosen, P. Oyhantçabal and M. Pistón, *MethodsX*, 2022, **9**, 101793.

232 W. W. Wendlandt and L. A. Funes, *Journal of Inorganic and Nuclear Chemistry*, 1964, **26**, 1879–1884.

233 M. A. Richard and R. J. Pancirov, *Journal of thermal analysis*, 1987, **32**, 825–834.

234 D. Brandon and W. D. Kaplan, *Microstructural Characterization of Materials, 2nd Edition*, Wiley, 2nd edn., 2008.

235 Augsten, *J Basic Microbiol*, 1987, **27**, 166.

236 R. S. Frankel and D. W. Aitken, *Appl Spectrosc*, 1970, **24**, 557–566.

237 ChemTalk: Raman Spectroscopy, https://chemistrytalk.org/raman-spectroscopy/, (accessed 16 September 2023).

238 R. Osibanjo, R. Curtis and Z. Lai, *Infrared Spectroscopy*. https://chem.libretexts.org/Bookshelves/Physical_and_Theoretical_Chemistry_Textbook_Maps/Supplemental_Modules_(Physical_and_Theoretical_Chemistry)/Spectroscopy/Vibrational_Spectroscopy/Infrared_Spectroscopy/Infrared_Spectroscopy (accessed 7 September 2023).

239 K. Zhou, W. Ma, Z. Zeng, X. Ma, X. Xu, Y. Guo, H. Li and L. Li, *Chemical Engineering Journal*, 2019, **372**, 1122–1133.

240 L. Xu, X.-C. Wu and J.-J. Zhu, *Nanotechnology*, 2008, **19**, 305603.

241 A. Mohtasebi, T. Chowdhury, L. H. H. Hsu, M. C. Biesinger and P. Kruse, *The Journal of Physical Chemistry C*, 2016, **120**, 29248–29263.

242 F. García-Picazo, S. Sicairos, G. Fimbres Weihs, S. W. Lin, M. Salazar-Gastélum and B. Trujillo-Navarrete, *Polymers (Basel)*, DOI:10.3390/polym13101637.

243 G. Greczynski and L. Hultman, *J Appl Phys*, 2022, **132**, 011101.

244 A. Stenner, R. J. Lewis, J. Brehm, T. Qin, Á. López-Martín, D. J. Morgan, T. E. Davies, L. Chen, X. Liu and G. J. Hutchings, *ChemCatChem*, 2023, **15**, e202300162.

245 J. P. Birk, Characteristic Reactions of Zinc Ions (Zn^{2+}), https://chem.libretexts.org/Bookshelves/Analytical_Chemistry/Supplemental_Modules_(Analytical_Chemistry)/Qualitative_Analysis/Characteristic_Reactions_of_Select_Metal_Ions/Characteristic_Reactions_of_Zinc_Ions_(Zn) (accessed 7 September 2023).

246 C. Fornari, G. Fornari, P. Rappl, E. Abramof and J. Travelho, 2018. DOI: 10.5772/intechopen.70220

247 S. M. A. Naqvi, *Structural and optical properties of chromium doped zinc oxide nanoparticles synthesized by sol-gel method*, 2014.

248 B. Houng, Y. Shih, S. Lu and W. Chien, *J Electroceram*, DOI:10.1007/s10832-015-0011-0.

249 A. Miller, L. Yu, J. Blickensderfer and R. Akolkar, *J Electrochem Soc*, 2015, **162**, D630–D634.

250 C. A. Milligan, R. R. Seemakurthi, J. Gao, J. P. Greeley, J. T. Miller, F. H. Ribeiro and D. Y. Zemlyanov, *The Journal of Physical Chemistry C*, 2022, **126**, 13660–13674.

251 J. P. Mathew and M. Srinivasan, *Eur Polym J*, 1995, **31**, 835–839.

252 N. Lawes, I. E. Gow, L. R. Smith, K. J. Aggett, J. S. Hayward, L. Kabalan, A. J. Logsdail, T. J. A. Slater, M. Dearg, D. J. Morgan, N. F. Dummer, S. H. Taylor, M. Bowker, C. R. A. Catlow and G. J. Hutchings, *Faraday Discuss*, 2023, **242**, 193–211.

253 Y. Sun, J. Wu, Y. Wang, J. Li, N. Wang, J. Harding, S. Mo, L. Chen, P. Chen, M. Fu, D. Ye, J. Huang and X. Tu, *JACS Au*, 2022, **2**, 1800–1810.

254 J. Ruiz Esquius, H. Bahruji, S. H. Taylor, M. Bowker and G. J. Hutchings, *ChemCatChem*, 2020, **12**, 6024–6032.

255 N. Lawes, K. J. Aggett, L. R. Smith, T. J. A. Slater, M. Dearg, D. J. Morgan, N. F. Dummer, S. H. Taylor, G. J. Hutchings and M. Bowker, *Catal Letters*, DOI:10.1007/s10562-023-04437-5.

256 R. Pothu, H. Mitta, P. Banerjee, R. Boddula, R. K. Srivastava, P. K. Kalambate, R. Naik, A. Bahgat Radwan and N. Al-Qahtani, *Mater Sci Energy Technol*, 2023, **6**, 484–492.

257 O. A. Ojelade and S. F. Zaman, *Catalysis Surveys from Asia*, 2020, **24**, 11–37.

258 S. R. Noble, S. E. Barnes, R. Banerjee, J. Miller and J. R. Regalbuto, *J Catal*, 2021, **393**, 344–356.

259 K. Cheng and Z. Da-Ming, *Sensors*, 2005, DOI: 10.3390/s5040209.

260 X. Yang, S. Kattel, S. D. Senanayake, J. A. Boscoboinik, X. Nie, J. Graciani, J. A. Rodriguez, P. Liu, D. J. Stacchiola and J. G. Chen, *J Am Chem Soc*, 2015, **137**, 10104–10107.

261 A. García-Trenco, E. R. White, A. Regoutz, D. J. Payne, M. S. P. Shaffer and C. K. Williams, *ACS Catal*, 2017, **7**, 1186–1196.

262 B. Deng, H. Song, Q. Wang, J. Hong, S. Song, Y. Zhang, K. Peng, H. Zhang, T. Kako and J. Ye, *Appl Catal B*, 2023, **327**, 122471.

263 X. Zhang, J.-X. Liu, B. Zijlstra, I. A. W. Filot, Z. Zhou, S. Sun and E. J. M. Hensen, *Nano Energy*, 2018, **43**, 200–209.